4. EXPERIMENTAL REPORTS

4.1. CONDENSED MATTER PHYSICS

Diffraction

Effect of Oxygen Isotope Substitution on Magnetic Structure of $(La_{0.25}Pr_{0.75})_{0.7}Ca_{0.3}MnO_3$
A.M.Balagurov, V.Yu.Pomjakushin, D.V.Sheptyakov, V.L.Aksenov, N.A.Babushkina, L.M.Belova, A.H.Taldenkov, A.V.Inyushkin, P.Fischer, M.Gutmann, L.Keller, O.Yu.Gorbenko, A.R.Kaul

SMB_6 Structure under the Effect of Applied Pressure
D.Yu.Chernyshev, D.V.Sheptyakov, M.B.Smirnov

A Neutron Diffraction Investigation of a γ Manganese Hydride
V.K.Fedotov, V.E.Antonov, A.I.Kolesnikov, A.I.Beskrovnyi, G.Grosse, F.E.Wagner

Neutron Diffraction Strain Studies of Geomaterials on the Diffractometer EPSILON
Ch.Scheffzuek, A.Frischbutter, K.Walther

Residual Stress Studies in Cu-W Gradient Materials
J.Schreiber, M.Stalder, G.Bokuchava, N.Shamsutdinov

Cu-W Composites Study at High Temperatures and under Applied Load
J.Schreiber, M.Stalder, G.Bokuchava, N.Shamsutdinov

Small-Angle Scattering

Bilayer Thickness and Acyl Chain Length in Extruded Unilamellar Phosphatidylcholine Liposomes
P.Balgavy, M.Dubnickova, M.A.Kiselev, S.P.Yaradaikin

Structure of Mixed POPC/$C_{12}E_n$ Aggregates, SANS Study
T.Gutberlet, M.Koselev, H.Heerklotz, G.Klose

SANS Study of Onion-Type Micelles Formed by an ABC Block Copolymer with a pH-Sensitive Middle Block
J.Plestil, H.Pospisil, B.Masar, M.A.Kiselev

Inelastic Scattering

Neutron Diffraction Study of Thermal Expansion and Compressibility of Pyridinium Nitrate and Tetrafluoroborate
L.Bobrowicz-Sarga, P.Czarnecki, S.Lewicki, I.Natkaniec, J.Wisicki

Neutron Scattering Study of the Liquid Helium Excitation Spectrum
I.V.Bogoyavlenskii, A.V.Puchkov, A.N.Skomorokhov

Low Frequency Internal Vibrations of Norbornane and its Derivatives Study by the IINS Spectroscopy and Quantum Chemistry Calculations
K.Holderna-Natkaniec, I.Natkaniec, V.D.Khavryutchenko

Neutron Study of Dynamic Atomic Correlations in Amorphous Isotopic Ni-B Alloys
S.N.Ishmaev, Y.V.Lisichkin, A.V.Puchkov, V.A.Semenov, E.Svab, G.F.Syrykh

On Hydrogen Localization in the β' Phase of $VO_{0.2}$
S.I.Morozov

Ammonium Dynamics Study in the $Rb_{1-x}(NH_4)_xI$ Mixed Crystals
I.Natkaniec, M.L.Martinez Sarrion, L.Mestres, L.S.Smirnov

Neutron Spectrometry and Numerical Simulations of Low-Frequency Internal Vibrations in Solid Xylenes
I.Natkaniec, K.Holderna-Natkaniec, J.Kalus, V.D.Khavryutchenko

Comparative Analysis of Ionic and Hydrophobic Hydration by Inelastic Neutron Scattering
A.G.Novikov, M.N.Rodnikova, O.V.Sobolev

Some Structural and Dynamical Properties of Liquid $PoCl_3$
A.G.Novikov, D.I.Seluverstov, O.V.Sobolev

The IINS Spectroscopy of Amino Acids: L-Isoleucine
A.Pawlukojc, I.Natkaniec, J.Leciejewicz

Incoherent Inelastic Neutron Scattering Studies of 1,8-bis(dimethylamino)naphthalene and its Protonated Forms
A.Pawlukojc, I.Natkaniec, E.Grech, J.Baran, Z.Malarski, L.Sobczyk

Neutron Optics

Neutron Standing Waves at Total Reflection of Polarized Neutrons Observed through Spin-Flip and Beam-Splitting
V.L.Aksenov, Yu.V.Nikitenko, S.V.Kozhevnikov, F.Radu, R.Kruijs, Th.Rekveldt

Observation of Resonance Enhanced Neutron Standing Waves Using Charged Particle Emission after Neutron Capture
V.L.Aksenov, Yu.V.Nikitenko, F.Radu, Yu.M.Gledenov, P.V.Sedyshev, A.V.Petrenko, S.V.Kozhevnikov

Reflectometry Studies of the Coherent Properties of Neutrons
D.A.Korneev, V.I.Bodnarchuk, S.P.Yaradaikin, V.F.Peresedov, V.K.Ignatovich, A.Menelle, R.Gaehler

Profile Analysis

Study of Oxidation of Thin Cobalt Layers by Elastic Scattering of Helium Ions
A.P.Kobzev, O.A.Nikonov, L.P.Chernenko, N.K.Pleshanov, S.V.Metelev, A.F.Schebetov, V.A.Ul'yanov

EFFECT OF OXYGEN ISOTOPE SUBSTITUTION ON MAGNETIC STRUCTURE OF $(La_{0.25}Pr_{0.75})_{0.7}Ca_{0.3}MnO_3$

A.M.Balagurov, V.Yu.Pomjakushin, D.V.Sheptyakov, V.L.Aksenov
FLNP JINR, Dubna, Russia
N.A.Babushkina, L.M.Belova, A.H.Taldenkov, A.V.Inyushkin
RRC Kurchatov Institute, Moscow, Russia
P.Fischer, M.Gutmann, L.Keller
PSI, Villigen, Switzerland
O.Yu.Gorbenko, A.R.Kaul
Chemistry Department, Moscow State University, Moscow, Russia

Recent studies revealed a close interplay between transport (electrical) and magnetic properties of perovskite manganites $A_{1-x}A'_xMn^{3+}_{1-x}Mn^{4+}_xO_3$, where A=La, or a rare earth, A'= Ca, Sr etc. These compounds were widely known since the discovery of the colossal magnetoresistance (CMR) effect [1]. At room temperature these compounds are usually paramagnetic insulators (PI), and their low temperature state is ferromagnetic metal (FMM), or antiferromagnetic insulator (AFI) with a tendency to ordering of manganese charges (CO) (see, for example, Refs. [2–4].) The low temperature state is determined by a subtle balance of several interactions and can be modified by changing the composition or by external forces (pressure or magnetic field). The particular state depends on doping level, i.e. on the proportion of Mn^{3+}/Mn^{4+}, and on the relation between the Mn-O and A-O bond lengths which in turn depends on average A-cation radius ($<r_A>$).

For example, according to the literature data, the insulator-metal (I-M) phase transition is observed in $(La_{1-y}Pr_y)_{0.7}Ca_{0.3}MnO_3$, with natural oxygen isotope content, for $y \leq 0.75$, while for $y = 1$ the compound is insulator in the whole temperature range. It was shown in Ref. [5], that the composition with y=0.75 is close to the phase boundary between metal and insulating states, that is conditioned by the critical value of tolerance factor of perovskite structure for this compound (t≈0.91). As a result, the low-temperature state can be easily modified even by relatively weak effect of the oxygen isotope substitution. It was shown [6], that the composition with natural content of oxygen isotopes (99.7% ^{16}O) becomes metallic at T≈100 K, while the ^{16}O – ^{18}O exchange resulted in the insulating state down to 4 K.

In the present investigation we continue the study of the $(La_{1-y}Pr_y)_{0.7}Ca_{0.3}MnO_3$ system and report new experimental data obtained for the compound with y=0.75 by the neutron diffraction technique. Two oxygen isotope samples of this compound have been studied: the first one (O-16 sample hereafter) contained the natural mixture of isotopes (99.7% ^{16}O, metallic at T≤100 K) and in the other one (O-18 sample hereafter) 75% of oxygen was substituted by ^{18}O (insulating in the whole temperature range). The main goal of the study was to find out the changes in crystal and magnetic structure accompanying the colossal isotope-effect in this compound.

The powder samples for neuron diffraction experiments were prepared by means of the so-called «paper synthesis», with the following annealing of quite a complicated character in the nature oxygen atmosphere and in the atmosphere enriched with ^{18}O.

Neutron diffraction experiments on the magnetic structure determination were carried out on DMC diffractometer at the SINQ spallation neutron source at PSI (at λ=2.5616 Å in the range of scattering angles $10<2\theta<90°$, which gave the corresponding to d_{hkl} region from 1.8 to 14.7 Å), and the study of crystal structure peculiarities was done on TOF High Resolution Fourier diffractometer (HRFD) of the IBR-2 pulsed reactor in Dubna in the d_{hkl} region from 0.8 to 2.8 Å.

Rietveld refinement of the diffraction patterns taken on DMC at room temperature showed, that the O-16 and O-18 samples are indeed identical, in particular with respect to oxygen content with the accuracy ±0.03. The comparison of the unit cell parameters for both samples gives even better matching for the oxygen content. They were measured at HRFD at room temperature and coincided within accuracy 0.002 – 0.004%.

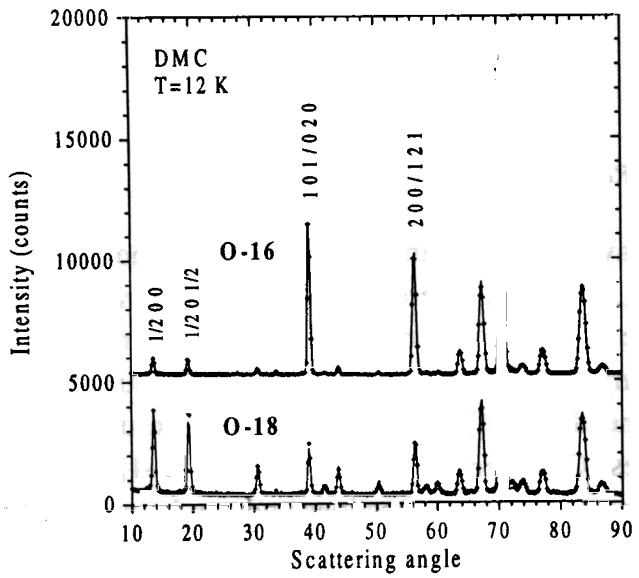

Fig.1. Diffraction patterns of the O-16 (top) and O-18 (bottom) samples measured with DMC at T=12 K. For the O-16 pattern the y-scale is shifted by 5000 counts. The Miller indices highlight the most intensive AFM and FM peaks. At 12 K the AFM intensity, (1/2 0 0) and (1/2 0 1/2) peaks, is much higher for O-18 sample, whereas for O-16 sample the intensity of FM peaks, (101) / (020) and (200) / (121), is high.

Superlattice reflections such as (1/2 0 0) at 2θ=13.6° and (1/2 0 1/2) at 19.2° associated with antiferromagnetic (AFM) ordering appeared with the decreasing temperature (Fig. 1) for both samples. The intensities of these peaks are significantly higher for the O-18 sample at T=12 K. In the neutron diffraction pattern of O-16 sample at T=12 K an increased contribution to the nuclear Bragg peaks (101)/(020) and (200)/(121) at 2θ=39° and 56° due to the ferromagnetic (FM) ordering is clearly observed. The intensity of the AFM peaks monotonically increases with decreasing temperature for the O-18. For O-16 sample this dependence is non-monotonic with a maximum at T ≈110 K, which correlates with appearance of FM component in respective Bragg peaks.

The refinement of the O-16 sample magnetic structure was performed in the model of two antiferromagnetic phases (AFM1 and AFM2) and ferromagnetic phase (FM) with magnetic moments on Mn-atoms. The AFM1-phase peaks can be indexed using the **k**=(1/2 0 0) or **k**=(0 0 1/2) propagation vectors (doubling of the a or c unit cell directions), AFM2-phase peaks can be described using the **k**=(1/2 0 1/2) propagation vector (both a and c parameters are doubled). The refinement of the O-18 sample magnetic structure was done in the same way, but without FM-component. The temperature dependencies of the μ_{AFM1}, μ_{AFM2}, μ_{FM} magnetic moments are presented in Fig. 2. The magnetic structure in O-16 sample may be described as noncollinear canted structure. The complete suppression of the ferromagnetic component in the O-18 sample means that the isotope substitution results in the completely new magnetic state. This type of ordering has not been observed before in Pr manganites with 30% doping level and natural oxygen isotopes content.

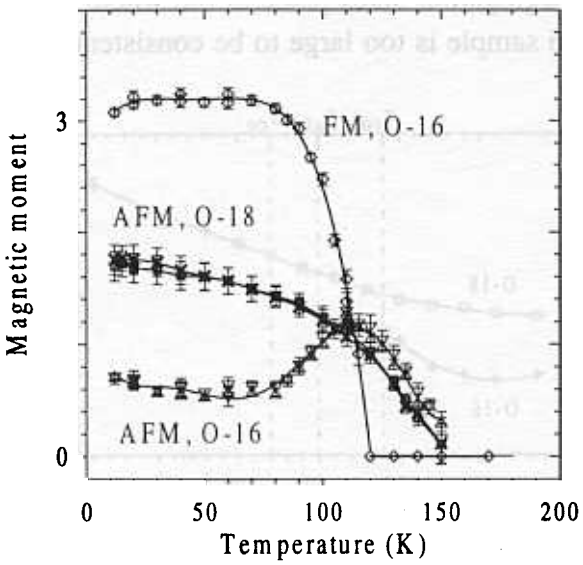

Fig.2. Temperature dependencies of the Mn magnetic moments (in Bohr magnetons) for the FM- and AFM-components of the O-16 sample and for the AFM-components of the O-18 sample. For O-16 sample some of the points were measured twice. The values of the AFM-moments for the O-18 sample for both propagation vectors coincide within the error bars. The lines are guides to the eye.

The temperature dependencies of the unit cell parameters for both samples were measured at HRFD instrument in Dubna, which high resolution ($\Delta d/d \approx 0.0015 - 0.0018$ in the working range of wavelengths) allowed to obtain high precision data. The example of a diffraction pattern obtained at HRFD, is given in the Fig. 3.

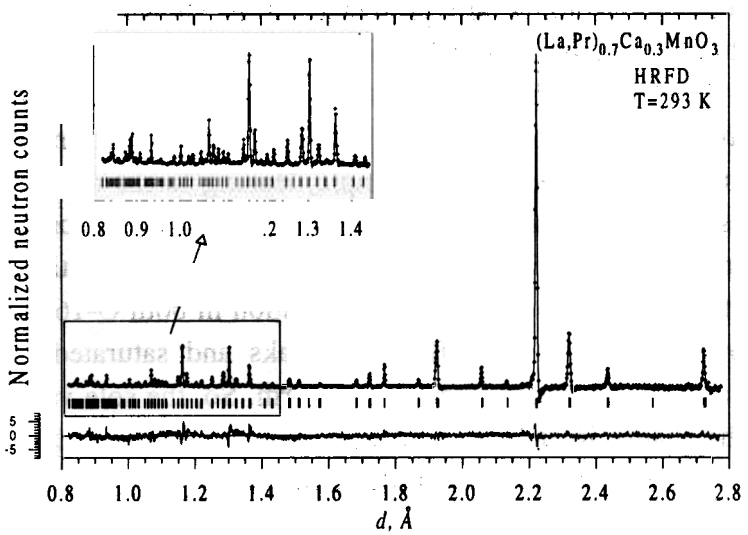

Fig. 3. Diffraction patterns of the O-18 sample measured with HRFD at room temperature and processed with the Rietveld method.

Several distinctive features are easily seen in the dependencies presented in Fig. 4, which correlate with behavior of the magnetic structure and the electrical properties. In both samples the temperature dependencies of the unit cell parameters are identical between the room temperature and the transition temperature of O-16 sample to metallic state. Moreover, their absolute values are practically the same. Any anomalies of the behavior of unit cell volume are absent, although *a* and *b* parameters have non-linear dependencies close to T_{CO} charge ordering temperature. Antiferromagnetic ordering at $T_{AFM} \approx 150$ K is not revealed in the temperature dependencies of lattice parameters. At the temperature of FM ordering, $T_{FM} \approx 110$ K, *b* parameter, and to some extent, *c* parameter of O-16 sample have well observed sharp jump which is also well visible in $V_c(T)$ dependence. This behavior corresponds to the transition from a high-volume to a low-volume state at phase transition from insulating to metallic state.

Unlike to the data of several published works, we did not observe significant effects of diffraction peak broadening, in spite of high resolution of the HRFD instrument. This fact allows us

to conclude that in both samples no long-range phase segregation takes place in the whole studied temperature interval. Also, the FM moment of the O-16 sample is too large to be consistent with a simple two-phase model.

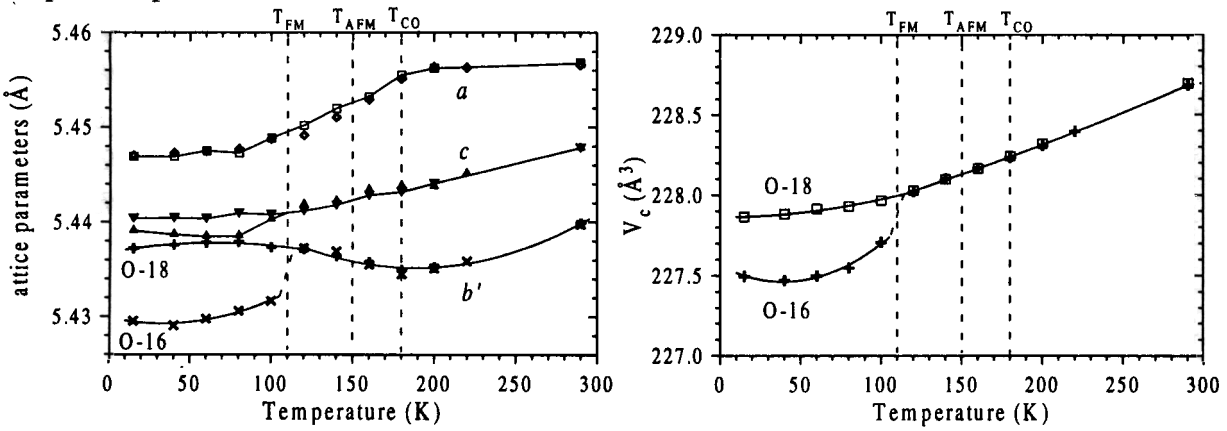

Fig.4. Temperature dependencies of lattice parameters (left) and unit cell volume (right) for the O-16 and O-18 samples ($b'=b/\sqrt{2}$). Between T_{FM} and room temperature, there is practically no difference between the parameters. The identity of the a unit cell parameter is preserved in the whole temperature range. The solid lines are guides to the eye.

In conclusion, the results of neutron diffraction study of two $(La_{0.25}Pr_{0.75})_{0.7}Ca_{0.3}MnO_3$ samples enriched by oxygen ^{16}O and ^{18}O isotopes are presented. It is shown, that at room temperature the samples are structurally identical. Antiferromagnetic ordering of manganese magnetic moments is observed below $T = T_{AFM} \approx 150$ K with propagation vectors (1/2 0 0) or (0 0 1/2) and (1/2 0 1/2). AFM-ordering process is developed identically in both samples down to 110 K. Below $T_{FM} \approx 110$ K the magnetic structure changes in O-16 sample, leading to the appearance of FM component of ordered manganese magnetic moments, decreasing of AFM-components, and partial destroying of the charge ordered state. We emphasize that oxygen isotope substitution did not affect T_{AFM}. We did not find any traces of long-range phase segregation in both O-16 and O-18 samples at low temperature. Moreover, the width of diffraction peaks and saturated value of magnetic moments indicate that the samples are macroscopically uniform. So, the sole variation of oxygen mass is responsible for both the change in electronic state (metal-insulator) and alteration of correlated magnetic state (noncollinear ferromagnetic - pure antiferromagnetic).

References

S.Jin, M.McCormac, T.H.Tiefel, and R.Ramesh, J. Appl. Phys. **76**, 6929 (1994).

2. C.N.R.Rao, A.K.Cheetham, and R.Mahesh, Chem. Mater. **8**, 2421 (1996).
3. A.P.Ramirez, J. Phys.: Condens. Matter **9**, 8171 (1997).
4. D.Cox, P.G.Radaelli, M.Marezio, and S.-W. Cheong, Phys. Rev. **B57**, 3305 (1998).
5. N.A. Babushkina, L.M.Belova, V.I.Ozhogin, O.Yu.Gorbenko, A.R.Kaul, A.A.Bosak, D.I.Khomskii, and K.I.Kugel, J. Appl. Phys. **83**, 7369 (1998).
6. N.A.Babushkina, L.M.Belova, O.Yu.Gorbenko, A.R.Kaul, A.A.Bosak, V.I.Ozhogin, and K.I.Kugel, Nature (London) **391**, 159 (1998).

SmB_6 STRUCTURE UNDER THE EFFECT OF APPLIED PRESSURE

Chernyshev D.Yu.
St. Petersburg Nuclear Physics Institute, Gatchina
Sheptyakov D.V.
Frank Laboratory of Neutron Physics, JINR, Dubna
Smirnov M.B.
Institute of Silicate Chemistry, St. Petersburg

The crystal structure of SmB_6 belongs to the framework type. The boron atoms in the structure are coupled by rather strong valence bonds, whereas the samarium atoms are located in vast holes of the boron framework. This causes the specific features of the SmB_6 lattice dynamics. The phonon spectra observed by neutron scattering include rather soft zone boundary modes. They are the so-called Rigid Unit Modes (RUM) predominantly involving the boron octahedra rotations. The RUM usually indicate the predisposition of the crystal structure to pressure induced phase transitions.
Despite of a great number of papers devoted to the SmB_6 lattice dynamics, the problem of a self-consistent dynamical model of phonon spectra and elastic properties has not been solved so far. This is partly because of lack of experimental information about the behavior of the crystal under pressure.
Thus, the purpose of the experiment was to obtain very important data on the crystal structure and thermal atomic parameters variation under hydrostatic compression. These data were supposed to help us to estimate reliably the dynamical model parameters. Another purpose was to try to detect the structural phase transition.
The experiments were carried out on the DN-12 diffractometer in June, 98. The diffraction patterns were collected at room temperature at pressures 0, 1, 2.6, 4.3, 6.0 and 7.0 GPa in a sapphire-anvil high-pressure cell. An example of the Rietveld refinement of the crystal structure under external pressure is given in Fig. 1.

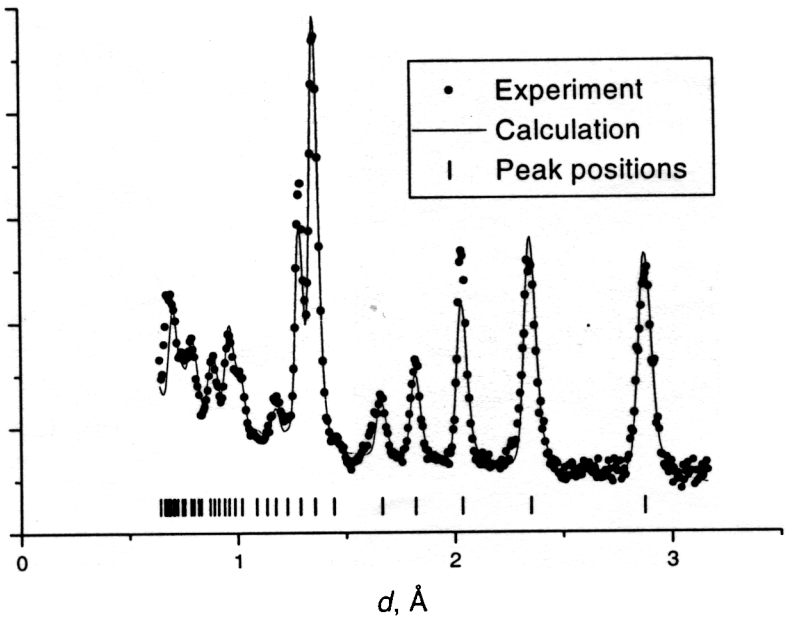

Fig.1. Rietveld refinement of the neutron powder diffraction data on SmB_6 at P=4.3 GPa. Measurement time ~12 hours on DN-12.

The final results of a detailed analysis of the dependencies of the thermal parameters on the pressure are not obtained yet. However, we can conclude that in the limits of our resolution we do not see the

structural phase transition in SmB_6 at pressures up to 7.0 GPa as it was predicted. Valuable information comes from an analysis of the dependence of the lattice parameters on the pressure. The pressure dependence of the *a* lattice parameter (sp.gr. 221) is given in Fig. 2.

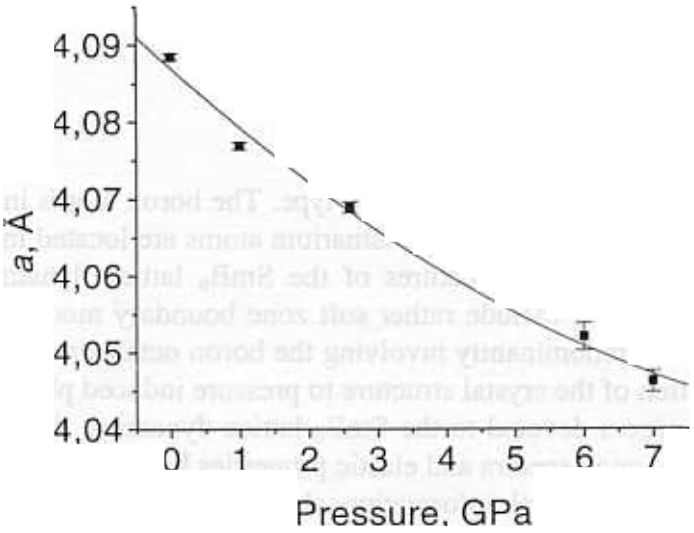

Fig. 2. Dependence of lattice parameter a of SmB_6 on the pressure. The solid line is a guide to the eye.

It turns out, that the crystal structure of SmB_6 is very hard compressible – the compressibility of the lattice parameter *a* is only κ_a = 1.38 (2) * 10^{-3} ГПа$^{-1}$. This value is several times lower than the compressibility of the typical inorganic compounds with unit cells of close dimensions.

A NEUTRON DIFFRACTION INVESTIGATION OF A γ MANGANESE HYDRIDE

V.K. Fedotov,V.E. Antonov, A.I. Kolesnikov
Institute of Solid State Physics, Russian Academy of Sciences, Chernogolovka, Russia
A.I. Beskrovnyi
Frank Laboratory of Neutron Physics, JINR, Dubna
G.Grosse, F.E.Wagner
Physik-Department E 15, Technische Universitat Munchen, D-85747 Garching, Germany

It is known that under high hydrogen pressures manganeses to form non-stoichiometric ε hydrides with a hcp metal lattice /1,2/ and non-stoichiometric γ hydrides with either fcc or fct metal lattices /3,4/. The crystal line and magnetic structures of antiferromagnetic ε hydrides were studied by neutron diffraction /5/ and was investigated Mossbauer spectroscopy /6,7/, and their lattice dynamics by inelastic neutron scattering /8/. γ manganese hydrides with the H/Mn atomic ratios x=0.04-0.36 were also found to be antiferromagnets and the dependence of their Neel temperature,T_N ,on the hydrogen concentration was studied in magnetization measurements and by neutron diffraction /3/.

The present article reports on the results of a neutron diffraction (ND) investigation of the crystal line and magnetic structure of γ–MnH_x with x~0.41. To prepare the hydride, powdered manganese metal of 99.99 wt.% purity and a grain size from 0.05 to 0.1~mm was loaded with hydrogen by means of a 20 min exposure to a hydrogen pressure of 2 GPa at 550K. The hydrogen content of the γ-MnH_x sample was determined to be x=0.411(5) by hot extraction at temperatures up to 800K. Under ambient conditions, no release of hydrogen from the sample was observed in the course of two weeks. The ND spectrum of a 300 mg sample of this hydride was measured at 300K for 20h with the high luminosity time-of-flight diffractometer DN-2 at the pulsed reactor IBR-2. The data were analysed with a computer program based on the Rietveld profile refinement technique.

The ND spectrum of γ-$MnH_{0.41}$ and the results of its profile analysis are presented in Fig.1. The smooth background is subtracted from the shown spectrum to allow a better visual comparison with the calculated profiles. An X-ray examination of the γ-$MnH_{0.41}$ sample at 300K (DRON-2.0 diffractometer, FeK_α radiation) showed that it has a fcc manganese lattice. As is seen from Fig.1, the ND spectrum of this sample contains intensive superstructure lines corresponding to the primitive cubic cell, space group Pm3m. The superstructure lines can be due to both hydrogen ordering and magnetic ordering. On the unpolarized neutron beam used in the experiment magnetic scattering and nuclear scattering are incoherent and the corresponding intensities are additive. Since the lines (001) and (003) are not observed in the ND spectrum, this means that only atomic and magnetic superstructures which give zero intensity for these reflections need to be considered in the analysis. Assuming a collinear spin structure, only four types of antiferromagnetic superstructures are compatible with the fcc lattice of magnetic atoms /9/. Of these, only one (type I) can be described with a cubic unit cell of the same size as the crystallographic fcc cell, $a=a_0$, while all others have unit cells twice as large in at least one dimension. Since all observed superstructure lines have integral indices of the cubic structure with $a=a_0$, the magnetic structure must be of the type I. The type I structure consists of ferromagnetic (001) planes coupled antiferromagnetically. From the observation that the (001) reflection is missing in the ND spectrum one can conclude that the magnetic moments of Mn atoms are oriented perpendicular to these planes, since the neutron scattering intensity from magnetic planes is proportional to the square projection of magnetic moments onto the planes. The resulting magnetic structure is shown in Fig.2. Its symmetry is tetragonal, Shubnikov space group P_I4/mmm. The magnetic Bravais cell with $a=a_0/\sqrt{2}$ and $c=a_0$ is shown by dashed lines. The diffraction lines of collinear antiferromagnetic superstructures in the fcc

lattice do not overlap with any of the fcc nuclear lines. Their profiles can therefore be analysed independently. As shown in Fig.1, curve b, the modelling of the proposed type I superstructure provides a good description of all superstructure lines in the ND spectrum of γ-$MnH_{0.41}$. In transition metal hydrides with close packed metal lattices hydrogen occupies either octahedral or tetrahedral interstices, the occupation of the tetrahedral ones occurring only in the dihydrides of titanium and vanadium group metals /10/. A model assuming hydrogen randomly occupying octahedral positions in the fcc metal lattice gives a good profile fit of the fcc lines in the ND spectrum (curve c in Fig.1). It also yields a value of x=0.41(3) hydrogen atoms per Mn atom which agrees well with x=0.411(5) measured by hot extraction. Together with the magnetic contribution (curve b), the calculated nuclear component (curve c) provides a rather good description of the whole ND pattern as one can see from the difference curve d. The intensity ratio of the magnetic and nuclear contributions yields σ = 1.88(15) μ_B/Mn atom for the magnetic moment of Mn atoms at 300 K. Neither tetrahedral hydrogen coordination nor the formation of an octahedral hydrogen superstructure in γ-$MnH_{0.41}$ are consistent with experiment. The former is illustrated by the difference curve e in Fig.1. Only two of them give rise to reflections with only integral indices and in both cases these reflections include the (001) one. The absence of the (001) reflection and of any reflections with fractional indices in the ND spectrum of γ–$MnH_{0.41}$ therefore shows that hydrogen is distributed randomly over octahedral sites.

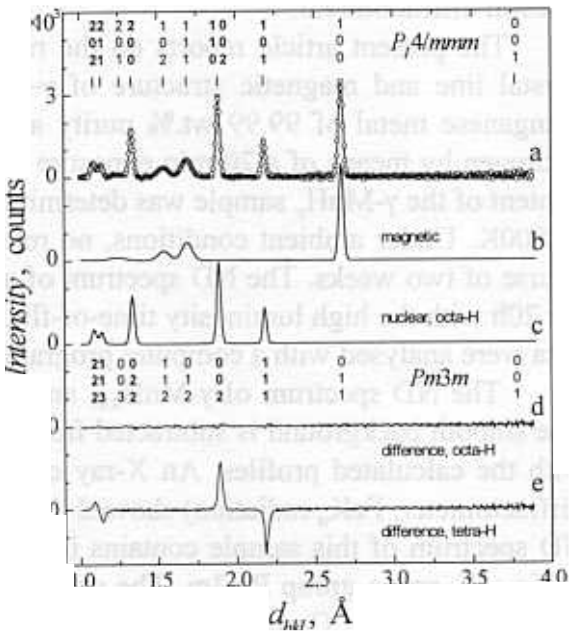

Fig1. Powder neutron diffraction spectrum of the γ-$MnH_{0.41}$ sample measured at 300K (circles) and results of its Rietveld analysis (solid lines). Curve a is the calculated profile and represents the sum of magnetic (b) and nuclear (c) contributions. Curve d is the difference between the experimental (dots) and calculated (curve a) spectra, (e) the difference between the experimental spectrum and that calculated for x=0.41 hydrogen atoms randomly occupying tetrahedral interstices in the fcc metal lattice of γ-$MnH_{0.41}$. Bold indices are for the lines of the fcc lattice.

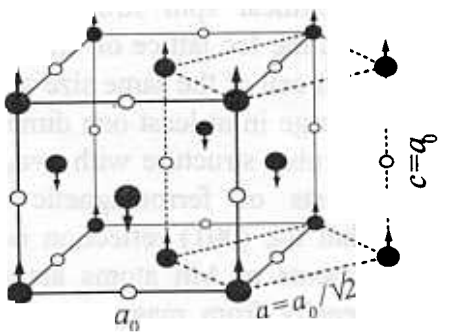

Fig. 2. Crystal (solid lines) and magnetic (dashed lines) Bravais cells of γ-$MnH_{0.41}$. Solid circles represent manganese atoms, open circles show the positions partly occupied by hydrogen, arrows indicate the positions and directions of magnetic moments.

References

1. M.Krukowski and B. Baranowski, Roczniki Chem., 49,(1975),1183.

2. E.G.Ponyatovskii, T.Belash, Dokl. Akad. Nauk SSSR, 224,(1975),607 (in Russian).

3. Y.Fukai, H.Ishikawa, T.Goto, J.Susaki, T.Yagi, J.L. Soubeyroux, D. Fruchart, Z. Phys. Chem. N.F.,163, (1989), 479.

4. S.M.Filipek, S.Majchrzak, A.B.Sawaoka, M.Cernansky, High Pressure Research, 7,1991, 271.

5. A.V.Irodova, V.P.Glazkov, V.A.Somenkov, S.Sh.Shil'shtein, V.E.Antonov, E.G.Ponyatovskii, Sov. Phys. Solid State, 29,1987,1562.

6. G.Schneider, M.Baier, F.E.Wagner, V.E.Antonov, T.E.Antonova, Yu.Kopilovskii, E.Makarov, Hyperfine Interactions, 69,1991,467.

7. G.Grosse, M.Baier,G.F. Schneider, F.E.Wagner, V.E.Antonov,T.E.Antonova, in Conf. Proc. Vol. 50, Int. Conf. on the Applications of the Mossbauer Effect 1995 ed. I. Ortalli, p.~215, SIF, Bologna (1996).

8. V.E.Antonov, I.T.Belash, A.I.Kolesnikov, J.Mayer, I.Natkaniec, E.G.Ponyatovskii, V.K.Fedotov, Sov. Phys. Solid State,33,1991,87.

9. Yu.A.Izyumov, V.E.Naish, R.P.Ozerov, Neutron Diffraction of Magnetic Materials, p.273, Consultants Bureau, New York (1991).

10. V.A.Somenkov and S.Sh.Shil'stein, Z. Phys. Chem. N.F.,117,1979,125.

NEUTRON DIFFRACTION STRAIN STUDIES OF GEOMATERIALS ON THE DIFFRACTOMETER EPSILON

CH. SCHEFFZUEK [1,2] , A. FRISCHBUTTER [1] & K. WALTHER [1]
[1] *GeoForschungsZentrum Potsdam, Telegrafenberg, 14473 Potsdam, Germany*
[2] *Frank Laboratory of Neutron Physics, JINR, 141980 Dubna, Russia*

The strain/stress characterization of rocks is important for the understanding of the deformation behaviour and will allow the estimation of the complete strain/stress tensor. Furthermore, the spontaneous reduction of large internal stresses in the Earth's crust is the cause of earthquakes. Such internal stress fields are permanently present. Up to now, their characterization has been done mainly on a macroscopic scale. A new method is to characterize the strain/stress state of rocks by microscopic lattice properties, for instance along a definite geological structure by means of strain/stress measurements of its constituents using diffraction methods. For such intracrystalline strain measurements of rocks there have been used only X-ray diffraction so far [1,3]. For geological materials, however, neutron diffraction is a much more suitable tool because of a high penetration depth of neutrons which allows the investigation of the stress state of sample volumes of some cm^3.

The main aim of our experiments was to prove that first of all, neutron diffraction, especially the time-of-flight method, is a very suitable tool for intracrystalline strain/stress determination of geological materials. The investigated specimen originates from a drilling depth of about 250 m and was prepared immediately after core extraction as a cylinder with a diameter of 38 mm and a length of 100 mm pushed at half its length into a steel tube (Fig. 1).

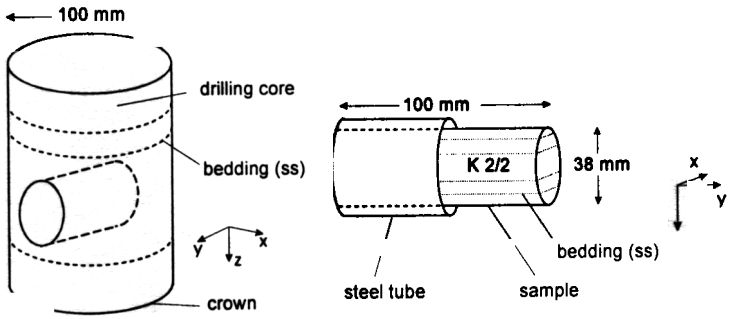

Fig. 1: *The sketch illustrates the sample orientation regarding the drilling core and the preparation mode. The sample was measured in the directions [x], [y] and [z] of the free and encapsulated part, respectively.*

In order to determine the d_0-values required for the calculation of the strain ε, an equivalent of the measured sample was grinded up to a grain size <62 μm, the powder was annealed for 24h at a temperature ≤ 500°C and its diffraction pattern recorded on the diffractometer EPSILON [4]. The beam geometry of the diffractometer allows the simultaneous measurement in two, perpendicular to each other directions characterized by the scattering vectors Q_1 and Q_2. The scattered neutrons are recorded by a multi-channel time analyser with a channel width of 32μs. The time-of-flight diffraction pattern of the encapsulated part of the sample is demonstrated in Fig. 2. The resolution of the diffractometer allows complete separation of quartz (11-21) and (01-12)/(10-12) BRAGG reflections (Fig. 3).

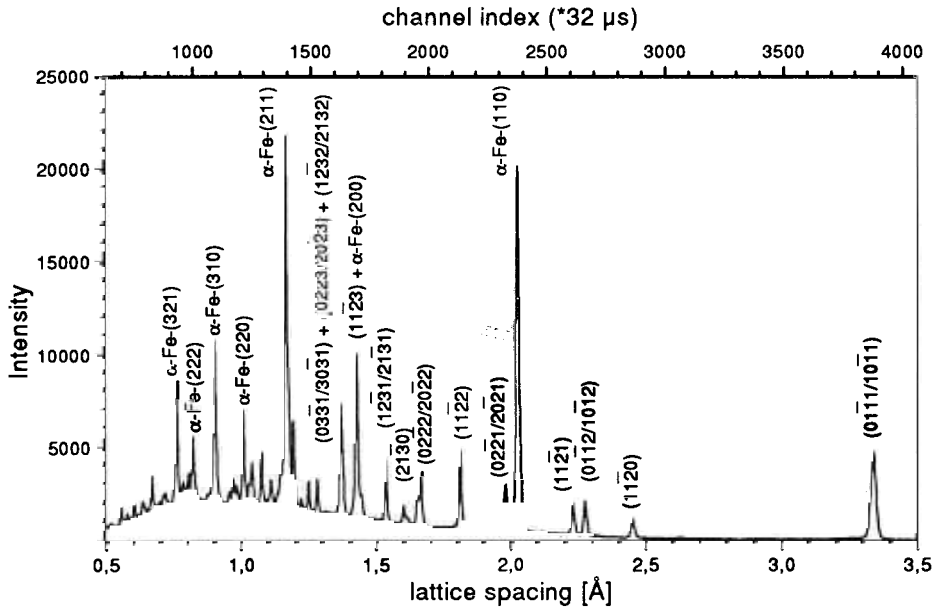

Fig. 2: Neutron time-of-flight diffraction pattern of the enclosed part of the quartz sample K2/2. Only the (110) BRAGG reflection of α-Fe overlaps the quartz (02-21)/(20-21) BRAGG reflection.

The asymmetrical shape of the peaks is caused by the asymmetry of the incident neutron pulse and is not an indicator of internal stresses. The right flank corresponds to slower neutrons and is broader than the left flank which corresponds to faster neutrons. This asymmetry was taken into account by fitting the peaks with the asymmetrical double sigmoidal function [3], Fig. 3.

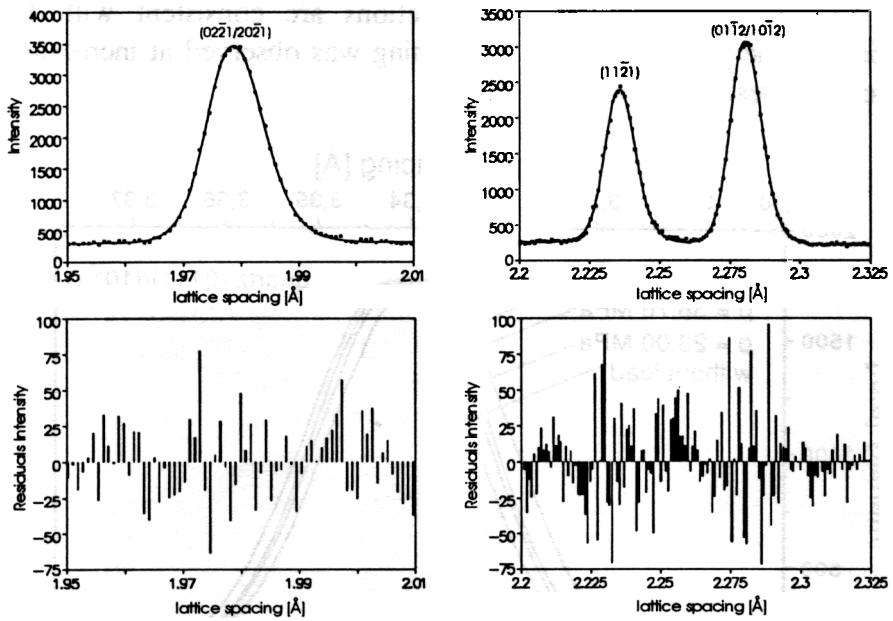

Fig. 3: Illustration of the neutron-TOF-BRAGG reflection (02-21)/(20-21) - left - and the peaks (11-21) with (01-12)/(10-12) - right - measured within the free part of the samples [x]-direction. The peaks were fitted using the asymmetrical double sigmoidal function. The diagrams in the lower rank represent the corresponding residual intensities.

In the [x]-direction of the free part of the specimen there was observed a positive strain (*e.g.* stretching) of about $2 \cdot 10^{-4}$, the enclosed part shows negative strains (*e.g.* compression) of about $-3.5 \cdot 10^{-4}$.

The errors are less than nearly one order of magnitude of the values obtained for the strain, so the results are considered to be significant. The ε-values of about $-2.5 \cdot 10^{-4}$ (compression) are determined for the enclosed part of the sample in the [z]-direction. The strain values vanish for the free part of the sample in the [z]-direction. The data clearly indicate a slight compression of about $-1 \cdot 10^{-4}$ within the enclosed, but -unexpectedly- a distinct compression of about $-4 \cdot 10^{-4}$ within the free part of the quartz sample [2].

Within any geological ensemble there exists a balance of forces (*e.g.* stresses). Each sampling from this ensemble will destroy this balance and most of the load stresses will quickly relax and/or redistributed; only residual stress will remain. Studies of drill cores from the KTB deep well in Bavaria [5] indicated measurable stress recovery by microcracking in up to 100 h after core extraction, obviously distinctly depending on the intensity of the anisotropic features of the specimens (*e.g.* texture).

A pressure device for uniaxial load up to 100 kN (140 MPa at sample dimensions of 30 mm diameter and 60 mm length) has been installed for diffraction experiments under load. The experiments will allow a better understanding of the strain/stress- and relaxation behaviour of first and second order internal stresses. First experiments, carried out on the sandstones mentioned above, demonstrate a linear peak shift indicating the dependence of macrostresses on the applied stress.

The strain values $\varepsilon = \Delta d/d_0$ are of the order of 10^{-3} at a load of about 67 MPa (Fig. 4). The applied stress and the observed lattice contractions are consistent with HOOKE's law. Furthermore, besides the peak shift, peak broadening was observed at increasing stress as an indicator of microstresses.

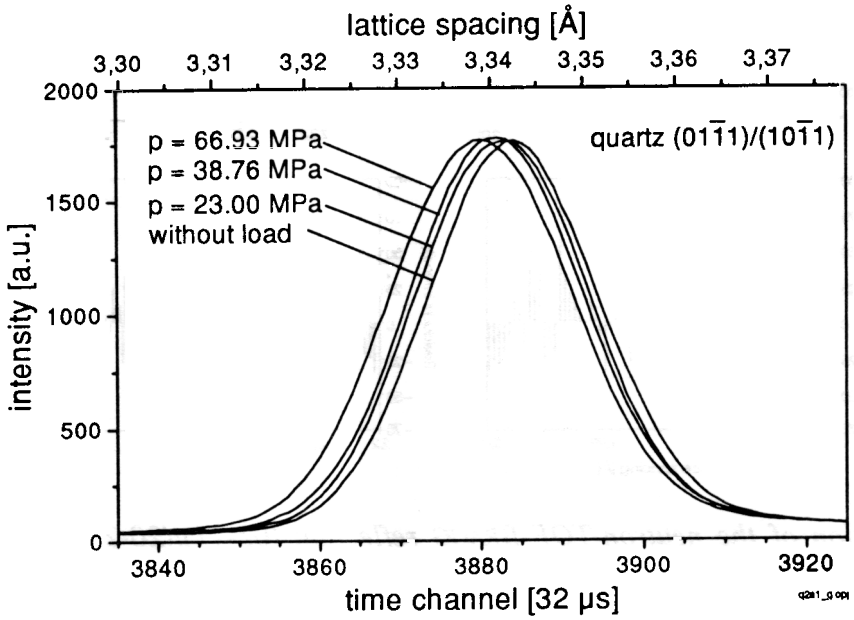

***Fig. 4:** Peak shift as a function of applied stresses up to about 67 MPa demonstrated with the (01-11)/(10-11) BRAGG reflection of quartz.*

References

[1] FRIEDMAN, M. (1972): Residual elastic strain in rocks. *Tectonophysics* **15,** 297-330.

[2] FRISCHBUTTER, A., SCHEFFZUEK, CH. & WALTHER, K. (1998): Strain Measurements on Geological Samples at the EPSILON-Neutron Diffractometer. Proceedings of the German-Russian User Meeting, Condensed Matter Physics with Neutrons at IBR-2, JINR Dubna, 80-86.

[3] REIK, G. (1976): Residuelle Spannungen in quarzreichen Gesteinen. Roentgendiffraktometrische Messung und Erklaerungsmoeglichkeiten ihrer Entstehung. *Geol. Rdsch.* **65**, 66-83.

[3] SCHEFFZUEK, CH., FRISCHBUTTER, A. & WALTHER, K. (1998): Intracrystalline Strain Measurements with Time-of-Flight Neutron Diffraction: Application to a Cretaceous Sandstone from the Elbezone (Germany). *Schriftenr. f. Geowiss.* **6**, 39-48.

[4] WALTHER, K., FRISCHBUTTER, A. & SCHEFFZUEK, CH. (1998): The Diffractometer EPSILON for the Measurement of Strains: An Estimation of the Full Stress Tensor. *Schriftenr. f. Geowiss.* **6**, 19-28.

[5] ZANG, A., WOLTER, K. & BERCKHEMER, H. (1989): Strain recovery, microcracks and elastic anisotropy of drill cores from KTB deep well. *Scientific Drilling* **1**, 115-126.

Residual stress studies in Cu-W gradient materials

J.Schreiber[1], M.Stalder[1], G.Bokuchava[2], N.Shamsutdinov[2]
[1]) EADQ IzfP, Dresden.
[2]) FLNP JINR, Dubna.

The aim of corresponding proposal was to determine the stress field in gradient materials W/Cu and to compare it to FEM calculations. The samples were produced in Darmstadt by an electrochemical gradation of porous tungsten preforms and subsequent infiltration of that with fluid copper at high temperatures [1]. The samples for the residual stress measurements (numbered 17 and 18) were almost cubic (fig.1, right).

In order to optimise statistics the gauge volume was chosen to comprise an entire slice through the sample with the phase fraction nearly constant within each slice (fig. 1). However, the thickness of the gauge volume attenuated the incident beam and considerably shifted the centre of gravity of the scattered beam, an effect that had to be corrected for later. The gradient direction (denoted as axial direction in the sample's coordinate system) was always perpendicular to the incident beam. Each sample was measured twice, with the gradient direction in the scattering plane and normal to it (see fig.1). Thus three orientations of the scattering vector: 90°, 76° and 45° relative to sample's axis were obtained. Assuming cylindrical symmetry this allows to derive the stress components in both the axial and the perpendicular direction. The evaluation of the strain from the measured diffraction pattern was achieved by means of a Rietveld refinement [2] instead of analysing single peaks. Strains were converted into stresses using the following averaged bulk elastic constants: E_{Cu} = 145 GPa, E_W = 411 GPa, μ_{Cu} = 0,35 and μ_W = 0,28. The stress free lattice parameters were obtained by reference samples of the single phase material, yielding $a_{o,Cu}$ = 3,6149±0,0001 and $a_{o,W}$ = 3,1651±0,0001. The macrostresses were calculated as the weighted average (in terms of volume) of the stresses of the Cu- and W-phase, whereas the microstresses are the difference between macrostresses and the stress value of the individual phases.

As it could be seen from fig. 2 the infiltration process and may be due to temperature gradients the Cu phase turned out to be significantly textured. This texture is obviously responsible for deviations of Rietveld-yielded phase ratios and those provided by sample producers (fig.3).

The Cu phase turned out to be highly textured which is probably caused by the infiltration process and large temperature gradients during solidification. The texture might also be responsible for disagreements between the phase fractions determined by the Rietveld refinement and those reported by the manufacturers of the samples (fig.2).

The measured macrostresses in sample 17 (fig.4) are qualitatively close to FEM calculations [2]. Even the change in the absolute value of residual stresses crossing from the left border and towards to the interface with the Cu-block fits well with the 600 MPa difference between them. But for the sample 18 we clearly see the compression in Cu in the tungsten rich side, what is not described by the model of thermal expansion coefficients mismatch. In the same time the Cu-side shows thermally induced stresses well match the FEM calculations.

For the sample 17 the scan at x=1mm with step 3mm across the gradient direction was performed with 3mm slits on the scattered beam. Since theory predicts no dependence on radial position for tangential and radial components of stress tensor, using this one orientation we can estimate the axial stress dependence. Interesting results (see fig.5) had been found. For the centre of the sample stresses behave as thermally induced (i.e Cu is in tension) and in agreement with FEM calculations. When we go closer to edge, we see the Cu is getting to compression.

We explain the disagreement with theory as a result of deformation stresses arising during inhomogeneous cooling. This is confirmed by the neutron diffraction measurements at D1A (ILL) of gradient samples, produced in the same manner but having a cylindrical shape. Unfortunately, because of texture in Cu-phase only tungsten strain could be measured. The measurements were

carried out twice: with sample as it had been produced and after the controlled slow annealing process and have shown a considerable decrease in stresses in tungsten.

Conclusions

1. Volume macro- and microstresses were determined for different Cu-W gradient materials by neutron diffraction. Qualitatively it was confirmed that thermal induced stresses are reduced for finer gradients. However, the experimental results do not agree quantitatively with theoretical simulations available so far. The reason for that is the presence of strong deformation stresses in the Cu-phase, which was not taken into account in the simulations.

2. Microstresses in the Cu-phase were found sometimes to be compressive resulting from too fast cooling process or uncontrolled temperature gradients. The deformation stresses can be avoided by corresponding heat treatment which can change the microstresses drastically.

It is a task for further study to investigate the origin of the obtained strong deformation stresses and to analyze the influence of the manufacturing process on the residual stress distribution in gradient materials systematically in order to optimize their mechanical properties.

References

1) R.Jedamzik, A. Neubrand, J. Rödel: „Electrochemical processing and characterisation of graded tungsten/copper composites", Proceedings of 14th Intern. Plansee Seminar, Eds.: G. Kneringer, P. Rödhammer, P. Wilhartitz, Plansee AG, Reutte, Vol. 1, p. 1 (1997)

2) Zlokazov V.B., Chernyshov V.V., „MRIA - a Program for Full Profile Analysis of Powder Neutron-Diffraction Time-of-Flight (Direct and Fourier) Spectra". JINR, P10-90-315, Dubna, 1990.

3) W. Schaller: „Berechnung thermischer Spannungen in einem gradierten Wolfram-Kupfer Verbundwerkstoff", Bericht innerhalb des DFG-SPP *Gradientenwerk-stoffe* (Karlsruhe, 1997)

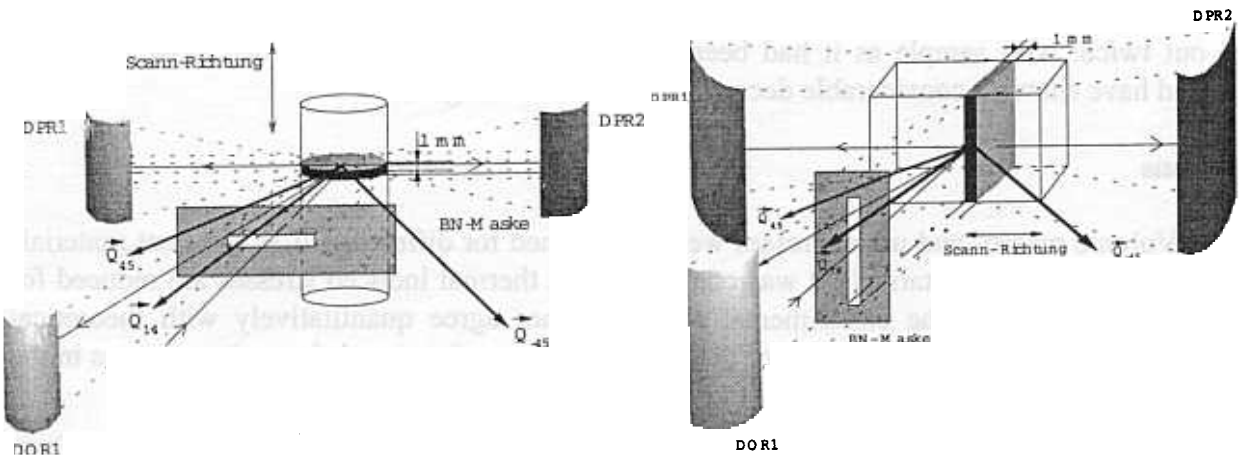

Fig.1. Scattering geometry for layered gradient materials diffraction measurements.

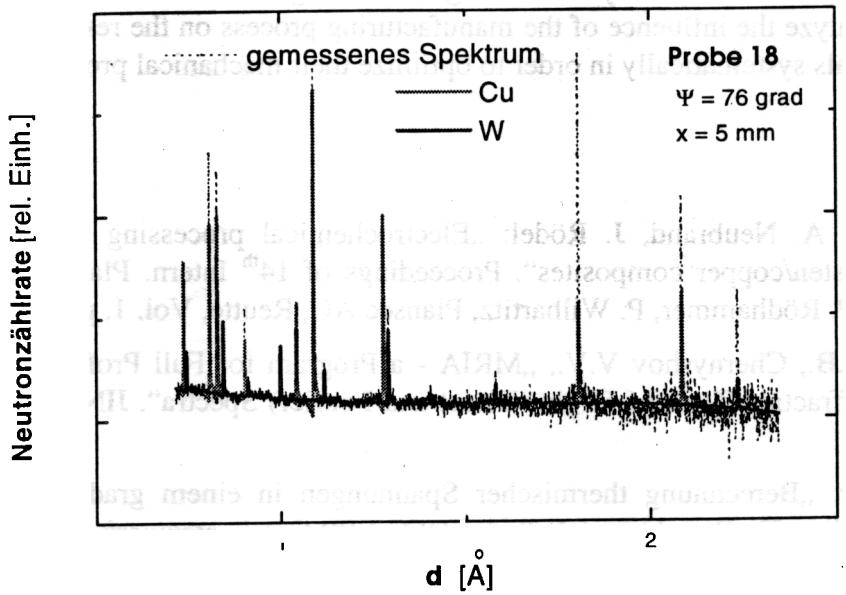

Fig2. The measured spectrum and its Rietveld refinement. Note the texture in Cu phase.

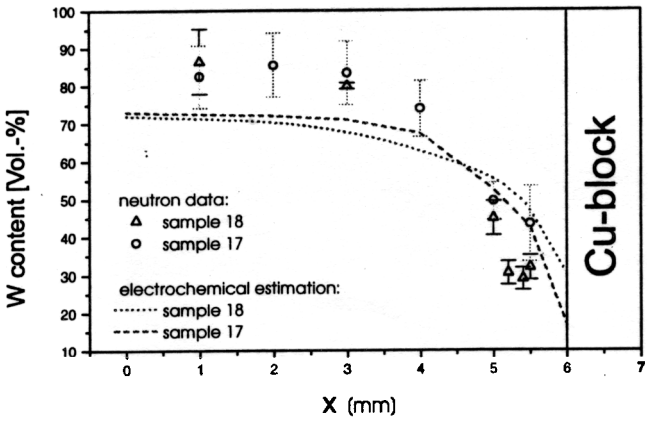

*Fig.3. The tungsten volume content, obtained from neutron diffraction and estimated by electrochemical estimations [1]. **x** is the position along the gradient.*

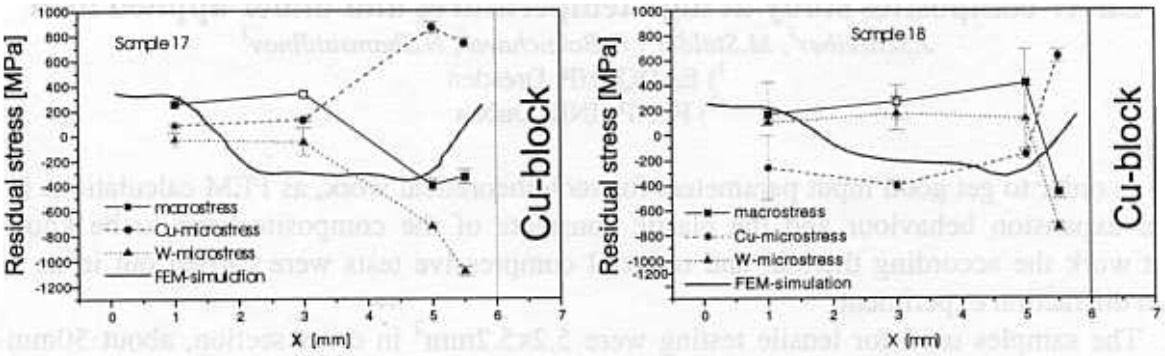

Fig.4. Residual stresses perpendicular to the gradient direction as determined by neutron diffraction and FEM-calculations [4].

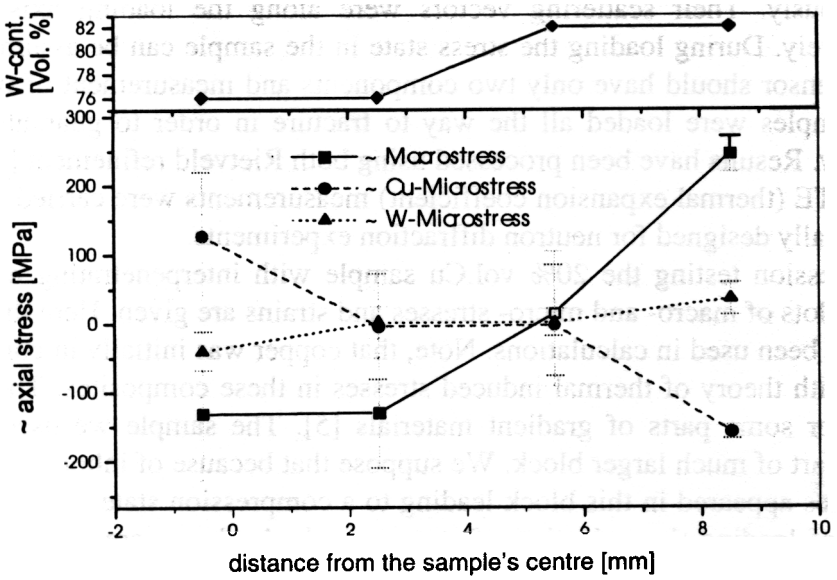

Fig.5. Estimated axial stresses in sample 17.

Cu-W composites study at high temperatures and under applied load

J.Schreiber[1], M.Stalder[1], G.Bokuchava[2], N.Shamsutdinov[2]
[1]) EADQ IzfP, Dresden
[2]) FLNP JINR, Dubna

In order to get good input parameters for such theoretical work, as FEM calculations [1], the thermal expansion behaviour and the elastic constants of the composite have to be known. In present work the according thermal and uniaxial compressive tests were carried out in an in situ neutron diffraction experiment.

The samples used for tensile testing were 5.2x5.2mm^2 in cross section, about 50mm long and consisted of an interpenetrating network of 20% Cu and 80% W that had been produced by infiltration of liquid copper into a porous tungsten preform [2]. Unfortunately, another batch of samples, manufactured by powder sintering [3], could not measured because of their high fragility. The way the loading frame was installed at HRFD, two detectors could measure the diffraction pattern simultaneously. Their scattering vectors were along the loading axis and 59° to that direction, respectively. During loading the stress state in the sample can be assumed to be uniaxial, so that the strain tensor should have only two components and measurement of two orientations is sufficient. The samples were loaded all the way to fracture in order to guarantee to get into the regime of plasticity. Results have been processed using both Rietveld refinement [4] and single peak processing. The CTE (thermal expansion coefficient) measurements were carried out using a mirror lamp furnace specially designed for neutron diffraction experiments.

For compression testing the 20% vol.Cu sample with interpenetrating networks had been used. In fig.1 the plots of macro- and micro- stresses and strains are given. Here the elastic constants from literature had been used in calculations. Note, that copper was initially in compression, what is in disagreement with theory of thermal induced stresses in these composites. The same result also had been found for some parts of gradient materials [5]. The sample we used for compression testing is just the part of much larger block. We suppose that because of inhomogeneous cooling the deformation stresses appeared in this block leading to a compression state in copper in our sample. In the beginning of loading the reduction of stresses in both phases are observed. And W-phase begins the non-elastic behaviour from almost the very beginning. Later, at the load of about 300 MPa, copper gets into a state of hydrostatic pressure. It corresponds to a sharp increase of peak width for copper (fig.2). And the Cu-phase seems to take all the load.

Unfortunately we had taken too big steps so rushing into plastic behaviour. That gave us no statistics to calculate precisely the elastic constants. However, using first two points the constants had been calculated: E_{Cu} = 148.8 GPa, E_W = 370.7 GPa, ν_{Cu} = 0.36, ν_W = 0.28, and are in good agreement with those from literature. For further study the elastic region must be studied more carefully to get more reliable result.

The first attempt to perform a compression test at high temperatures had been made. The present furnace together with loading machine allows us to use only back scattering geometry, that is why the strain tensor cannot be directly measured. But in future we believe the mirror furnace can be improved so that the temperature environment can be added without changes in described above compression experiment geometry.

For several composite samples of both powder-sintering manufacturing and interpenetrating networks the thermal expansion coefficients (CTE) were determined from measured lattice parameters: CTE(T) = (a(T) - a(20° C))/((T[°C]-20° C) a(20°C)). On fig.3, 4 the CTE behaviour is shown. The CTE corresponds to the stress state near the ambient region. That is especially pronounced for the 50/50 powder-sintered sample.

Conclusions

1. The coefficients of thermal expansion were determined for composites of various Cu-W content using special heating facility at the neutron beam. It was found that the obtained coefficients for each phase are modified by the microstress state significantly.

2. Interesting results are obtained by compressive testing for Cu-W composites with interpenetrating networks with 20 vol.% of Cu. Following the diffraction line broadening of Cu-phase an increase of the yield strength up to 300 MPa was found. On the other hand strong non-elastic behaviour was obtained for the W-network starting at 100 MPa load, which can be explained by local cracking of the W-network.

Altogether these measurements show that we can gather good experimental data at HRFD for modelling of gradient materials. Further research is needed to answer newly posed questions. The experiment with compression should be repeated after controlled annealing and with finer steps in elastic region ($\sigma < 100$ MPa). This annealing can be monitored by neutron diffraction to show the stress redistribution during the cooling.

References

[1] W. Schaller: „Berechnung thermischer Spannungen in einem gradierten Wolfram-Kupfer Verbundwerkstoff", Bericht innerhalb des DFG-SPP *Gradientenwerk-stoffe* (Karlsruhe, 1997)

[2] R.Jedamzik, A. Neubrand, J. Rödel: „Electrochemical processing and characterisation of graded tungsten/copper composites", Proceedings of 14th Intern. Plansee Seminar, Eds.: G. Kneringer, P. Rödhammer, P. Wilhartitz, Plansee AG, Reutte, Vol. 1, p. 1 (1997)

[3] A. Neubrand, J. Rödel: „Gradient Materials: An Overview of a Novel Concept", Z. Metallkunde 88 (1997) p. 5

[4] Zlokazov V.B., Chernyshov V.V., „MRIA - a Program for Full Profile Analysis of Powder Neutron-Diffraction Time-of-Flight (Direct and Fourier) Spectra". JINR, P10-90-315, Dubna, 1990.

[5] J.Schreiber, M.Stalder, G.Bokuchava, N.Shamsutdinov. The experimental report on gradient materials study at HRFD, FLNP JINR, 1998.

[6] Metals Reference Book, Editor: Colin J.Smithells, Butterworth, Boston&London, 5th Edition.

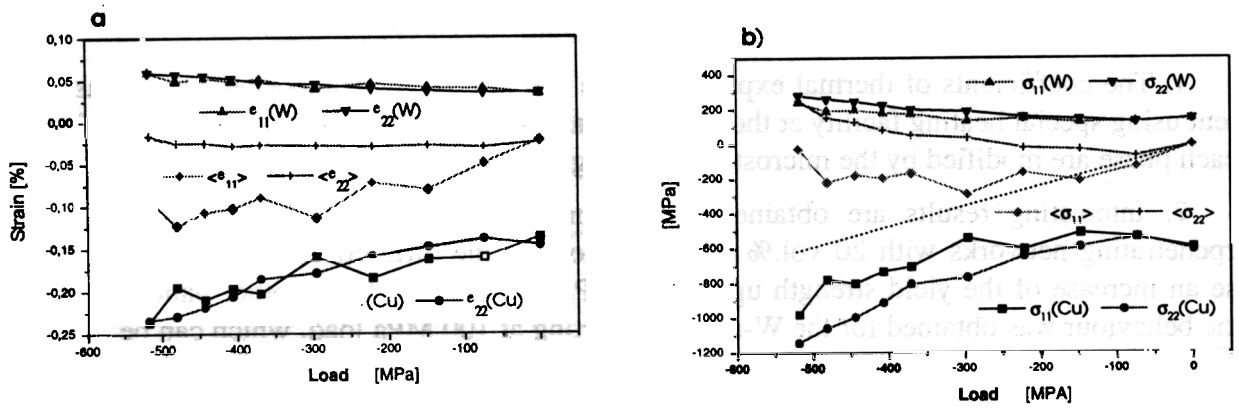

Fig.1. Micro- and macro stresses and strains in W/Cu composite (80% vol. W) under load. <..> means average of two phases, dot line denotes the applied load.

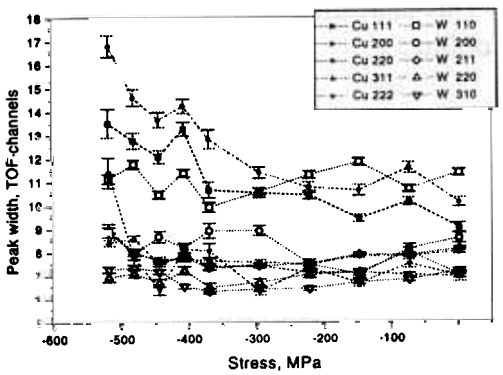

Fig.2. The peak width behaviour versus applied load.

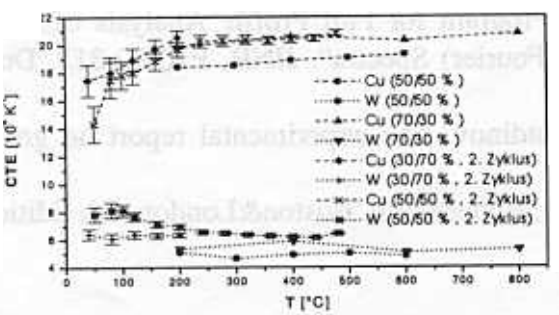

Fig.3. Results of the CTE-measurements for powder-sintered samples.

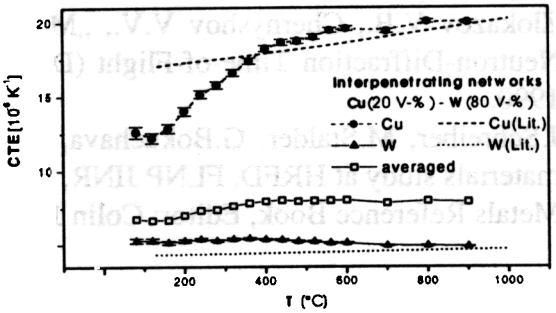

Fig.4. Results of CTE-measurements for interpenetrating networks sample with 20 vol.% Cu together with the literature values [5].

Bilayer thickness and acyl chain length in extruded unilamellar phosphatidylcholine liposomes.

P. Balgavy[1], M. Dubnickova[1], M. A. Kiselev[2], S. P. Yaradaikin[2]

[1]*Faculty of Pharmacy, J. A. Comenius University, 83232 Bratislava (Slovakia)*
[2]*Frank Laboratory of Neutron Physics, Joint Institute for Nuclear Research, 141980 Dubna (Russia*

Introduction

Phospholipid liposomes are widely used as the simplest models of the phospholipid part of biological membranes. Unilamellar liposomes are hollow spheres consisting of a phospholipid bilayer shell with the aqueous phase inside and outside the shell. One of the basic physical parameters of unilamellar liposomes is the thickness of the lipid bilayer, d_L. The thickness d_L profoundly affects the properties of transbilayer proteins. For example, the transbilayer protein (Ca-Mg)ATPase reconstituted in unilamellar 1,2-diacylphosphatidylcholine liposomes displays maximum activity at m=18, where m is the number of carbon atoms in the acyl chain containing one double bond [1]. In the present work, we determine the bilayer thickness in large unilamellar liposomes prepared from 1,2-diacylphosphatidylcholines with saturated acyl chains as a function of the number of acyl chain carbons n using SANS.

Material and Methods

The lipids 1,2-dilauroylphosphatidylcholine (DLPC), 1,2-dimyristoylphosphatidylcholine (DMPC), 1,2-dipalmitoylphosphatidylcholine (DPPC) and 1,2-distearoylphosphatidylcholine (DSPC) were purchased from Avanti Polar Lipids (Alabaster, USA) in a dry lyophilized form and were used without further purification. Heavy water (99.98 % ^2H_2O) was received from Izotop (Moscow, Russia). Lipid and heavy water were mixed in a glass tube. The tube was purged with pure gaseous nitrogen and sealed. The lipid concentration was 1 wt. % in each sample. The lipid was dispersed by hand shaking and sonication in a bath sonicator at temperature above the gel-fluid phase transition temperature (see below). From this dispersion, extruded unilamellar liposomes were prepared following the procedure of MacDonald et al. [26]. Using a LiposoFast Basic extruder (Avestin, Ottawa, Canada), liposomes were extruded through two polycarbonate filters (Nucleopore, Plesanton, USA) with pores 50 nm in diameter mounted on the extruder fitted by two gas-tight Hamilton syringes (Hamilton, Reno, USA). The sample was subjected to many passes through filters at temperature above the gel-fluid phase transition temperature (see below). An odd number of passes were performed to avoid contamination of the sample with large and multilamellar vesicles which might not have passed through the filter. This method yields liposomes with a wide distribution of diameters.

The SANS measurements were performed with the small-angle time-of-flight axially symmetric neutron scattering spectrometer YuMO at the IBR-2 fast pulsed reactor. The samples were poured into quartz cells (Hellma, Munich, Germany) to provide a 1 mm sample thickness. The sample temperature was set and controlled electronically at 20±0.1°C, 36±0.1°C, 44±0.1°C and 60±0.1°C for DLPC, DMPC, DPPC and DSPC samples, respectively, well above the gel-fluid phase transition temperatures of these phospholipids in heavy water [3]. The sample was equilibrated for 1 hour at a given temperature before the measurement. The acquisition time was two hours for each sample. The scattering patterns were corrected for background effects. The coherent scattering cross section was obtained by using a vanadium standard scatterer.

Results and Discussion

Figure 1 shows typical plots of the measured SANS scattering functions, $I(Q)$, as a function scattering vector Q defined as

$$Q=4\pi\sin\theta/\lambda \tag{1}$$

where 2θ is the scattering angle and λ is the wavelength of neutrons.

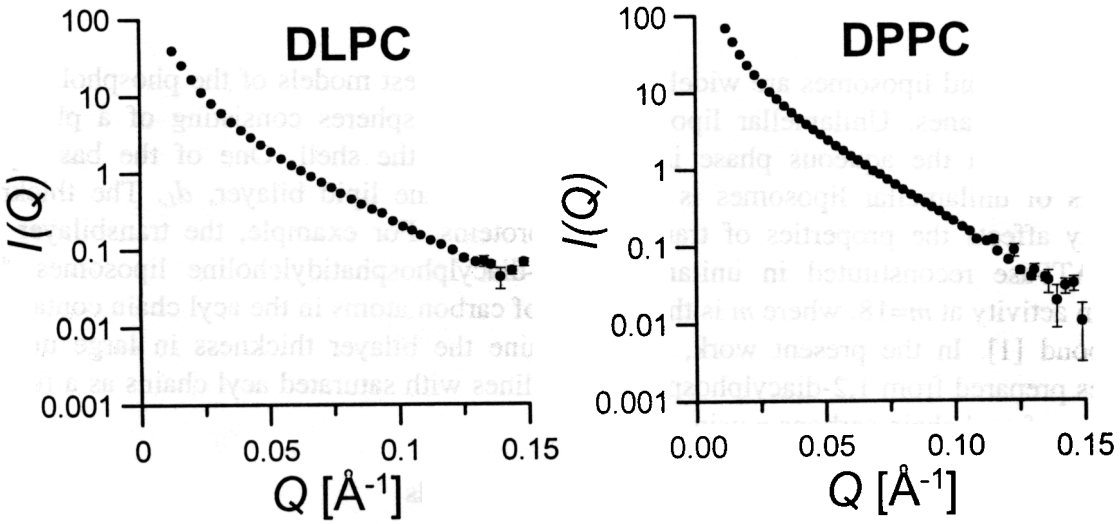

Fig.1. The dependence of the SANS intensity $I(Q)$ on the scattering vector Q

The experimentally determined mean coherent neutron scattering length density for DMPC liposomes is $\rho=0.27\cdot10^{14}$ m^{-2} [4] and for the solvent used, $\rho_S=6.4\cdot10^{14}$ m^{-2}. Gordeliy et al. [5] show that in the situation when the variation of the coherent neutron scattering length density over the phosphatidylcholine molecule ($\pm1\cdot10^{14}$ m^{-2}) is significantly smaller than the contrast $\Delta\rho=\rho_S-\rho$, scattering on the bilayer in a single unilamellar liposome may be approximated by scattering on the concentric shell with homogenous neutron scattering length density. The neutron scattering intensity per unit neutron flux on the sample and per unit volume for a monodisperse system can be written as

$$I(Q)=NP(Q)S(Q) \tag{2}$$

where N is the number of particles, $P(Q)$ is the particle structure factor and $S(Q)$ is the size and orientation dependent interparticle structure factor [39, 40]. $S(Q)$ is approximately equal to 1 for dilute and weakly interacting spherical particles. It has been found experimentally that at the low phospholipid concentration in the sample used (1 wt.%), $S(Q)\cong1$ [4-8]. Using the well-known equations for scattering on a hollow sphere [9], for monodisperse unilamellar liposomes with the heavy water inside and outside the bilayer, one can write

$$I(Q)=N(\Delta\rho)^2(4\pi/Q^3)^2(A_2-A_1)^2 \tag{3}$$

$$A_i=\sin(QR_i)-(QR_i)\cos(QR_i) \tag{4}$$

where N is the number of liposomes, and R_1 and R_2 correspond to the inner- and outer radius of the liposome, respectively. The bilayer thickness is then $d_L=R_2-R_1$. Komura et al. [10] observe that the oscillating scattering function $I(Q)$ is smeared by convolution with the liposome radius distribution

function and the spectrometer resolution function. Using computer simulated smeared scattering curves, we found, in our recent paper [11], that they approach the scattering function for planar two-dimensional sheets in the range of scattering vectors 0.001 $Å^{-2} \leq Q^2 \leq 0.006$ $Å^{-2}$ and liposome outer radii 500 $Å \geq R_2 \geq 200$ Å. To obtain the value of d_L, the Kratky-Porod plot

$$ln\{I(Q)Q^2\}=lnI(0)-R_t^2Q^2 \quad (5)$$

can be used, where

$$d_L^2=12R_t^2+aR_t^3+bR_t^4 \quad (6)$$

R_t is the radius of gyration and a=0.0223±0.0023 and b=0.0062±0.0001 are the constants obtained from simulated curves. Figure 2 shows typical Kratky-Porod plots of the experimental data and the table below lists the values of d_L obtained from these data by using the least squares fits.

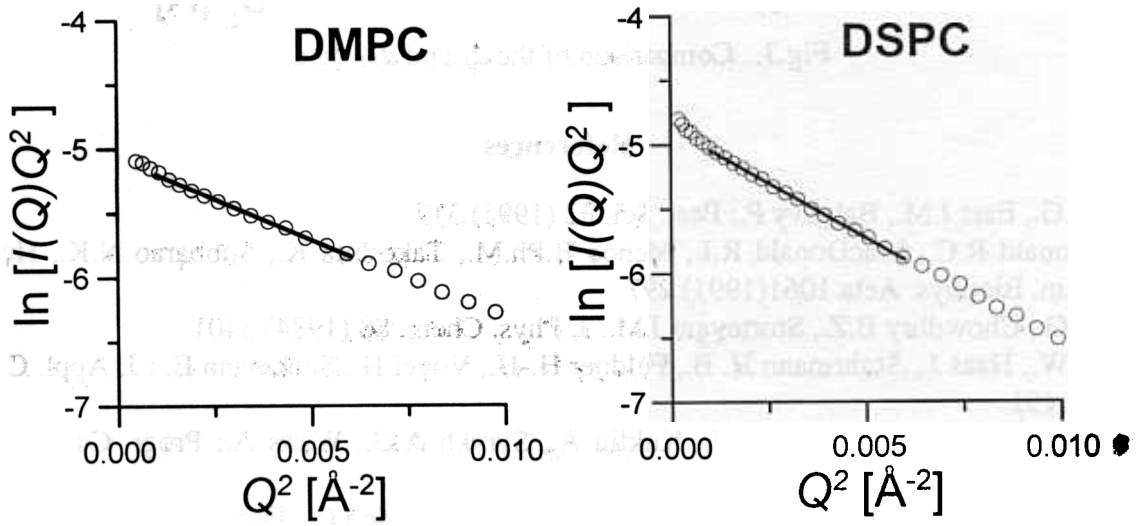

Fig.2. Kratky-Porod plots of the experimental neutron scattering curves. Full lines are obtained by fitting the data by eq. 5.

The table also shows the thickness d_L for extruded egg yolk phospatidylcholine (EYPC) liposomes obtained in our recent paper [11] as well as the distances d_{PP} between phosphatidylcholine phosphate groups across the lipid bilayer of unilamellar liposomes prepared by the ultrasonication method and measured by small-angle X-ray scattering (SAXS) [12, 13]. The data from the table are depicted in Fig.3. The values of d_L and d_{PP} display linear dependence on the number n of carbon

n	10 (20°C)	12 (20°C)	14 (36°C)	16 (44°C)	18 (60°C)	EYPC (20°C)
d_L		39.4±0.5 Å	40.8±0.4 Å	45.0±0.6 Å	47.8±0.3 Å	41.7±0.3 Å
d_{PP}	26.5±1.0 Å	30.5±1.0 Å	34.0±1.0 Å	37.0±1.0 Å	40.5±1.0 Å	36.0±1.0 Å

atoms in the phosphatidylcholine acyl chain for n=14-18 and n=10-18, respectively. The increment of the bilayer thickness per one acyl chain CH_2 group obtained from the d_L vs. n (d_{PP} vs. n) dependence is 1.75±0.20 Å (1.72±0.04 Å), which is (within the experimental error) analogous to 1.75 Å suggested in [14]. The cause of d_L deviation from linear dependence for DLPC is not known. We have also observed nonlinear correlation between d_L and d_{PP}. This is most probably caused by differences in the molecular packing of lipids in extruded and sonicated liposomes.

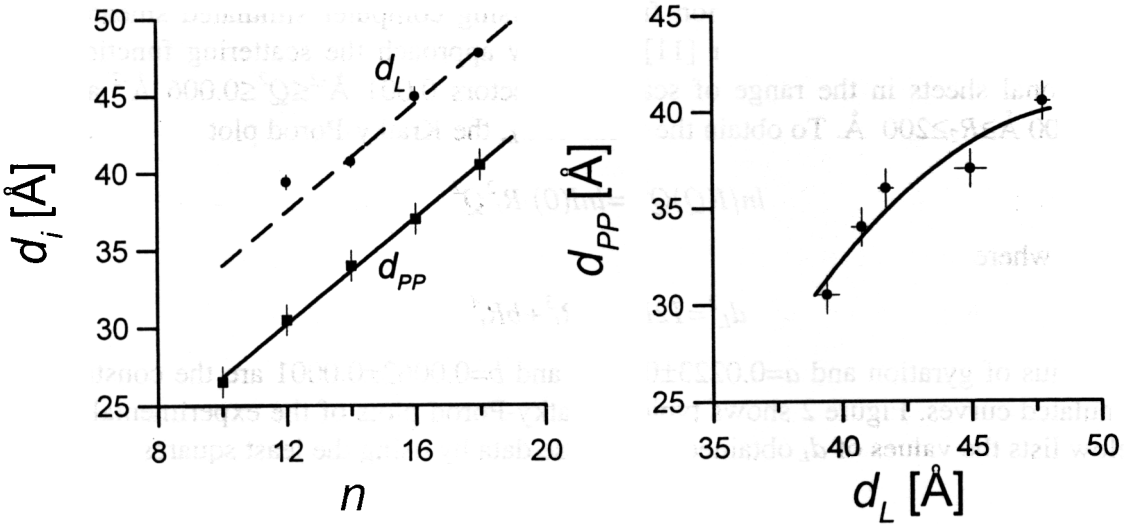

Fig.3 Comparison of the d_L and d_{PP} data.

References

1. Lee A.G., East J.M., Balgavy P.: Pest. Sci. 32 (1991) 317
2. MacDonald R.C., MacDonald R.I., Menco B.Ph.M., Takeshita K., Subbarao N.K., Hu L.-R.: Biochim. Biophys. Acta 1061(1991) 297
3. Lipka G., Chowdhry B.Z., Sturtevant J.M.: J. Phys. Chem. 88 (1984) 5401
4. Knoll W., Haas J., Stuhrmann H. B., Füldner H.-H., Vogel H., Sackmann E. : J. Appl. Cryst. 14 (1981) 191
5. Gordeliy V.I., Golubchikova L.V., Kuklin A., Syrykh A.G., Watts A.: Progr. Colloid Polym. Sci. 93 (1993) 252
6. Muddle A.G., Higgins J.S., Cummins P.G., Staples E.J., Lyle I.G.: Faraday Discuss. Chem. Soc. 76 (1983) 77
7. Nawroth T., Conrad, H., Dose, K.: Physica B 156&157 (1989) 477
8. Hjelm R.P.Jr., Thiyagarajan P., Alkan H.: J. Appl. Cryst. 21 (1988) 858
9. Feigin L.A., Svergun D.I.: Structure Analysis by Small Angle X-ray Scattering, Plenum, New York, 1987
10. Komura S., Toyoshima Y., Takeda T.: Jpn. J. Appl. Phys. 21 (1982) 1370
11. Balgavy P., Dubnickova M., Uhrikova D., Yaradaikin S., Kiselev M., Gordeliy V.: Acta Phys. Slov. 48 (1998) 509
12. Lewis B.A., Engelman D.M., J. Mol. Biol. 166, 211-217, 1983
13. Wilkins M.H.F., Blaurock A.E., Engelman D.M.: Nature New Biol. 239 (1971) 72
14. Sperotto M.M, Mouritsen O.G.: Europ. Biophys. J. 16 (1988) 1

STRUCTURE OF MIXED POPC /$C_{12}E_n$ AGGREGATES, SANS STUDY

T. Gutberlet*, M. Kiselev#, H. Heerklotz%, G. Klose*

* *Institute for Experimental Physics I, University of Leipzig, Linne-Str. 5, D- 04103 Leipzig, Germany*

\# *FLNP, Joint Institute for Nuclear Research, Dubna 141980, Russia*

% *Department of Biochemistry, McMaster University Health Sciences Center, Hamilton, ON L8N 3Z5, Ontario, Canada.*

Introduction

Mixtures of zwitterionic lipids, like POPC, and non-ionic detergents of the ethylene oxide type $C_{12}E_n$ are appropriate model systems for studying fundamental questions. The structure of bilayers formed of POPC and $C_{12}E_n$ at reduced hydration is characterized detail by different methods in /1-3/. At excess water, a vesicle micelle transition occurs for $n > 4$ /4/.

The results of structural changes obtained using SANS are presented for POPC/ $C_{12}E_8$ and POPC/ $C_{12}E_6$–d_{24} mixtures across a vesicle micelle transition.

1. POPC/ $C_{12}E_8$ mixed system

The solubilisation of POPC membranes by nonionic $C_{12}E_8$ detergent was studied by SANS at the YuMO spectrometer at T = 25°C. The measurements of mixed POPC/ $C_{12}E_8$ aggregates were carried out for the detergent pseudo molar fractions $\mathbf{X_D = N_D /(N_D + N_L)}$ ($\mathbf{N_D}$ and $\mathbf{N_L}$ are the mol of the detergent and lipid, respectively) of 0.1, 0.36, 0.6, and 0.85 with a mass concentration of amphiphiles (lipid + surfactant) of 10mg/ml in D_2O. In addition, pure $C_{12}E_8$ micelles ($\mathbf{X_D = 1}$) were measured to compare mixed lipid/detergent aggregates and pure detergent systems.

Figure 1 presents the scattering curves from systems with $\mathbf{X_D} = 0.1$, 0.6, and 0.85. The SANS spectra were measured at two sample to detector distances 7.463m and 13.173m. The scattering was recorded in the range of the scattering vector length **q** from 0.007Å^{-1} to 0.2Å^{-1}. For fitting the macroscopic cross-section $\mathbf{d\Sigma/d\Omega}$, the equation

$$\frac{d\Sigma}{d\Omega} = \frac{d\Sigma}{d\Omega}(0) \cdot q^{\alpha} \exp\left[-q^2 \cdot \beta\right] , \qquad (1)$$

was used. It allows one to distinguish between different morphologies of particles and determine the geometrical parameters α and β /5/. For spherical or ellipsoidal micelles, theoretically $\alpha = 0$, for rod-like micelles, $\alpha = -1$ and for vesicles, $\alpha = -2$. The gyration radius is calculated as $R_g = \sqrt{3 \cdot \beta}$ for spherical or ellipsoidal micelles, $R_c = \sqrt{2 \cdot \beta}$ for rod-like micelles, and $R_t = \sqrt{\beta}$ for vesicles. The radius of gyration is related, in a simple way, to the dimensions of particles. For spherical particles with the radius R, $R = R_g\sqrt{5/3}$, while for ellipsoidal particles with the semi-axes a, b, and c, $R_g^2 = \frac{1}{5}(a^2 + b^2 + c^2)$. For cylindrical particles, the radius is $R = R_C\sqrt{2}$, while for the ellipsoidal cross-section of rod-like micelles, $R_c^2 = \frac{1}{4}(a^2 + b^2)$. The thickness d_l of bilayers for vesicles is given by a simple formula, $d_l = R_t\sqrt{12}$.

The parameters α and β determined using equation (1) are summarized in Table 1. Mixed POPC/$C_{12}E_8$ systems with $\mathbf{X_D} = 0.1$ ($\alpha = -2.09$) and $\mathbf{X_D} = 0.36$ ($\alpha = -1.97$) are the lamellar systems according to the parameter α which theoretically, should be 2.0. The experimental spectra

fitted by the theoretical value of $\alpha = -2.0$ give equal $\beta = 125.0 \pm 2Å^2$ for the too concentrations corresponding to the membrane thickness $d_l = 38.7 \pm 0.8Å$. This fact shows that the membrane thickness is not affected by the detergent concentration in such concentration range.

The aggregates formed at $\mathbf{X_D} = 0.6$ are the rod-like micelles according to $\alpha = -1.09$. From the scattering curve the gyration radius of the micelle cross-section $\mathbf{R_c} = 19.46 \pm 0.4Å$ was estimated. If we assume that the cross-section is circular, we obtain the micelle radius $27.52 \pm 0.6Å$. But the micelle cross-section can also be ellipsoidal if the detergent is nonhomogeneously distributed across the micelle surface. In this case, the semi-axes will be $\mathbf{a} = d_l/2 = 19.4 \pm 0.4Å$ and $\mathbf{b} = 33.8 \pm 0.7Å$.

Because $\alpha = 0.0$, a mixed POPC/$C_{12}E_8$ system with $\mathbf{X_D} = 0.85$ creates ellipsoidal micelles with $R_g = 26.65 \pm 0.3Å$ corresponding to the semi-axes $\mathbf{a} = d_l/2 = 19.4 \pm 0.4Å$ and $\mathbf{b} = \mathbf{c} = 39.9 \pm 0.5Å$. Pure $C_{12}E_8$ dispersion $\mathbf{X_D} = 1.0$ creates spherical micelles according to $\alpha = 0.0$ with $R_g = 22.72 \pm 0.4Å$. Pure detergent micelles are spherical and their radius is $29.3 \pm 0.5Å$.

Table 1. *SANS parameters of mixed lipid/detergent aggregates of a POPC/$C_{12}E_8$ system.*

$\mathbf{X_D}$	χ^2	$d\Sigma/d\Omega(0)$	α	β, Å^2	morphology
0.1	0.16	$(4.6\pm0.2)\cdot10^{-3}$, cm^{-3}	-2.09 ± 0.01	136.8 ± 11	vesicle
0.36	1.37	$(7.7\pm0.2)\cdot10^{-3}$, cm^{-3}	-1.97 ± 0.006	129.2 ± 7	vesicle
0.6	0.05	$(8.3\pm0.2)\cdot10^{-2}$, cm^{-2}	-1.09 ± 0.005	189.4 ± 4	rod-like micelle
0.85	0.06	(3.22 ± 0.02), cm^{-1}	0.00 ± 0.0006	236.7 ± 3	ellipsoidal micelle
1	0.10	(2.58 ± 0.09), cm^{-1}	0.00 ± 0.008	172.1 ± 3.0	spherical micelle

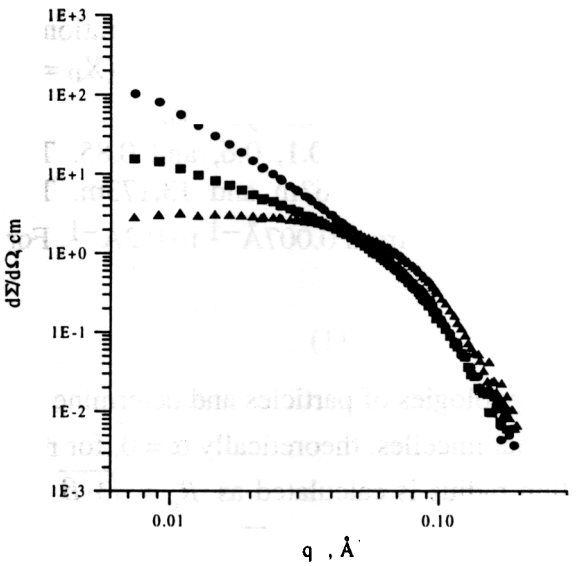

Figure 1. *SANS spectra of mixed POPC/$C_{12}E_8$ systems with $X_D = 0.1$ (circles), $X_D = 0.6$ (squares), and $X_D = 0.85$ (triangles) at $T = 25^oC$. Mixed lipid/detergent aggregates transform from vesicles at $X_D = 0.1$ ($\alpha = -2.09$) into rod-like micelles at $X_D = 0.6$ ($\alpha = -1.09$) and finally, in ellipsoidal and spherical micelles at $X_D = 0.85$ and 1.0, respectively1($\alpha = 0.0$).*

2. POPC/ $C_{12}E_6$–d_{24} mixed system

Similarly to POPC/$C_{12}E_8$ mixtures, mixed POPC/ $C_{12}E_6$–d_{24} aggregates transform from mixed unilamellar vesicles into mixed rod-like micelles increasing the detergent concentration. Figure 2 and Table 2 present the results obtained by SANS for a POPC/ $C_{12}E_6$–d_{24} system under the experimental conditions analogous to described in paragraph 1.

At $\mathbf{X_D} = 0.1$, 0.35, and 0.6 vesicular aggregates exist ($\alpha \approx -2$, see Table 2). Analysis of the scattering curves in the vesicular region gives decreasing values for the thickness parameter

calculated by equation (1). A decrease of the contrast between the solvent and the region of polar headgroups as the $C_{12}E_6$–d_{24} concentration increases must be taken into account in the data interpretation. In the limit, only the thickness of the hydrophobic bilayer core is measured. The thickness parameter of the hydrophobic core is 30.4 ± 0.6 Å at $\mathbf{X_D} = 0.6$.

The thickness parameters of lamellae for POPC/ $C_{12}E_8$ (see Table 1) and POPC/ $C_{12}E_6$–d_{24} (see Table 2) calculated by equation (1) with the theoretical value $\alpha = -2$ for the same $\mathbf{X_D} = 0.1$ are 38.7 ± 0.8 Å and 39.1 ± 0.7 Å, respectively. The thickness parameters are almost equal to one another. Consequently, the conclusion can be made that all ethylene oxide units of the detergent are totally included into the hydrophilic membrane region.

The scattering curve of pure $C_{12}E_6$–d_{24} micelles at small q gives $\alpha = -0.68 \pm 0.01$, which cannot be reasonably interpreted. But in the region of porod approximation $0.14 Å^{-1} \le q \le 0.17 Å^{-1}$, it can be fitted quite well ($\chi^2 = 3.0 \cdot 10^{-4}$) by the function $(3.31 \pm 1.65) \cdot q^{-(3.9 \pm 0.3)}$, cm^{-1}. This fact indicates that neutrons are scattered from a smooth solid surface including the hydrocarbon chains (micellar core). It is interesting to note that the SANS curve of non-deuterated $C_{12}E_8$ micelles deviates from the porod law within an analogous q range and is proportional to q^{-5}. It is reasonable to suppose that pure $C_{12}E_6$–$d_{24}$and $C_{12}E_8$ micelles have spherical shapes, and consist of a homogeneous hydrocarbon core and a limb of randomly oriented ethylene oxide chains around. A discontinuous surface of the limb might be the reason of deviation from the porod law q^{-4}.

Table 2. *SANS parameters of mixed lipid/detergent aggregates of a POPC/ $C_{12}E_6$–d_{24} system.*

$\mathbf{X_D}$	χ^2	$d\Sigma/d\Omega(0)$	α	β, $Å^2$	morphology
0.1	2.8	0.00643, cm^{-3}	−1.99±0.01	123.8±8	vesicle
0.36	3.0	0.00314, cm^{-3}	−2.14±0.01	82.4±8	vesicle
0.6	1.5	0.0027, cm^{-3}	−2.10±0.02	66.32±13	vesicle
0.85	0.08	0.029, cm^{-1}	−1.16±0.01	62.04±5	rod-like micelle
1	0.02	0.078, cm^{-1}	−0.68±0.01	74.04±3.0	?

Rod-like micelles exist at $\mathbf{X_D} = 0.85$ as an analysis of the SANS curve evidences. The Guinier approximation (see Fig. 3) yields $R_c = 14.10 \pm 0.07$Å and further estimation (see above) gives the radius of the cross-section $R = 19.94 \pm 0.10$Å. It is reasonable to conclude that this value characterizes the radius of the hydrophobic core only.

The size of the hydrophobic core for pure $C_{12}E_6$–d_{24} and $C_{12}E_8$ micelles must be approximately equal. The radius of $C_{12}E_8$ micelles is 29.3 ± 0.5Å (see paragraph 1) and the radius of the hydrocarbon core of $C_{12}E_6$–d_{24} is 19.94 ±0.10Å. Consequently, the thickness of the ethylene oxide region of $C_{12}E_8$ micelles is 9.46 ±0.60Å. It is a reasonable value for high disordered ethylene oxide chains.

Conclusions

The main stages in the morphology alteration at membrane solubilization by detergent are the lamellar structure, rod-like, ellipsoidal and finally spherical micelles.

Pure $\mathbf{C_{12}E_6}$ micelles do not have a continuous surface, the ethylene-oxide chains create tails around the hydrocarbon core. The core radius is $\mathbf{R} = 19.94 \pm 0.10$Å, the thickness of the ethylene-oxide region is 9.46 ±0.60Å.

In the lamellar phase, all ethylene-oxide chains are located in the region of POPC head groups

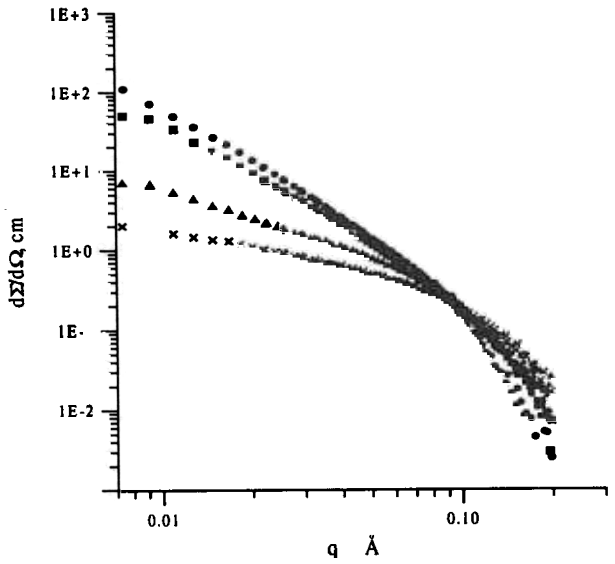

Figure 2. *SANS spectra of mixed POPC/ $C_{12}E_6$–d_{24} systems with* $\mathbf{X_D} = 0.1$ *(circles),* $\mathbf{X_D} = 0.6$ *(squares),* $\mathbf{X_D} = 085$ *(triangles),* $\mathbf{X_D} = 1$ *(crosses) at T = 25°C. Mixed lipid/detergent aggregates transform from lamellar structure at* $\mathbf{X_D} = 0.1$ *(*$\alpha = -1.99$*) and* $\mathbf{X_D} = 0.6$ *(*$\alpha = -2.1$*) into the rod-like micelles at* $\mathbf{X_D} = 0.85$ *(*$\alpha = -1.16$*).*

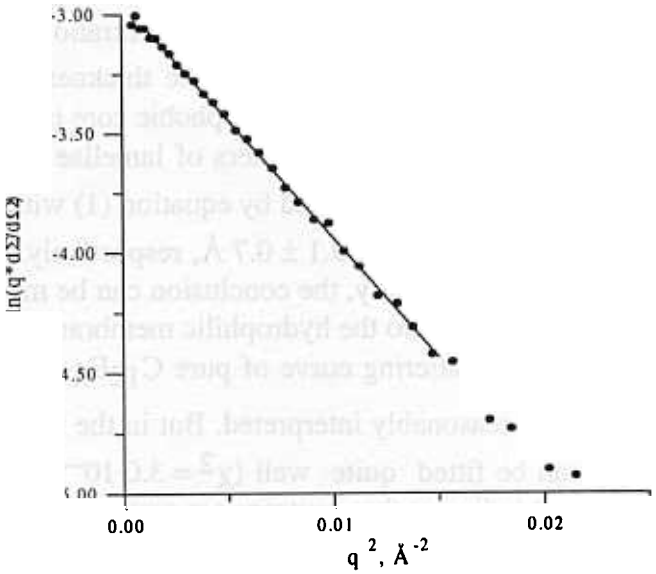

Figure 3. *Guinier approximation of a SANS curve of a mixed POPC/ $C_{12}E_6$–d_{24} system with* $\mathbf{X_D} = 0.85$ *at T = 25°C. Fitting by (1) with a fixed parameter* $\alpha = -1$ *yields rod-like micelles with the gyration radius* $R_c = 14.10 \pm 0.07$Å *and the radius of the cross- section* $R = 19.94 \pm 0.10$Å.

References

/1/ G. Klose, A. Islamov, B. Koenig, V. Cherezov, Langmuir 1996, 12, 409
/2/ B. Koenig, U. Dietrich, G.Klose, Langmuir 1997, 13, 525
/3/ G. Klose, B. Maedler, H. Schaefer, K.-P. Schneider, J. Phys. Chem. B. 1998 (in press)
/4/ H. Heerklotz, H. Binder, G. Lantzsch, G. Klose, J. Phys. Chem. B. 1997, 111, 639
/5/ M. A. Kiselev, P. Lesieur, A. M. Kisselev, S. A. Kutusov, L. I. Barsukov, T. N. Simonova, T. Gutberlet, G. Klose, Proc. German-Russian User Meeting, LNFP, April 2 - 4, 1998, Dubna

SANS study of onion-type micelles formed by an ABC block copolymer with a pH-sensitive middle block

J.Pleštil,[a] H.Pospíšil,[a] B.Masař,[a] and M.A.Kiselev[b]
[a] Institute of Macromolecular Chemistry, Academy of Sciences of the Czech Republic, Heyrovsky Sq.2, 162 06 Prague 6, Czech Republic
[b] FLNP, Joint Institute for Nuclear Research, 141980 Dubna, Russia

Introduction

Block copolymer micelles are polymolecular nanoparticles with a dense core formed by insoluble blocks and a protective corona formed by swollen soluble blocks. Most prospective applications of micelles are based on loading sparingly soluble compounds into micellar cores (solubilization). It is desirable to have a possibility of controlling this process by variation of the micelle parameters. Promising candidates for such purpose are onion-type micelles. Unlike commonly studied two-component core/corona micelles, the onion-type micelles have a three-layered structure.

Procházka et al.[1] developed a procedure for the preparation of the multilayered micelles using two diblock copolymers. Interpretation of SANS data for such system is not straightforward because beside the onion-type particles, a significant amount of the micelles formed by a stabilising copolymer is present[2]. The first attempt at SANS characterising onion-type micelles made of an ABC block copolymer is reported in Ref 3. For various reasons, the possibility of controlling the structure of the middle layer of these multilayered micelles was rather limited.

In this contribution, onion-type micelles prepared from an ABC triblock copolymer with a pH-sensitive middle block are studied. These micelles rank among promising systems for controlled uptake/release processes.

Block Copolymer and Micellar Solutions

An ABC triblock copolymer polystyrene-*block*-poly(2-vinylpyridine)-*block*-poly(ethylene oxide) (PSPVP-*b*-PEO) was used throughout this study. The molar mass of the blocks is respectively 14 100, 12 300 and 35 000 g mol^{-1}. First the copolymer is molecularly dissolved in a mixture of dioxan, methyl alcohol and water and then transferred by dialysis to aqueous media of various pH (0.1 M HCl (A), water (W), 0.2 M KOH (B)). The middle PVP block is expected to be swollen at low pH (A) and collapsed at high pH (W, B). Good solubility of PVP at low pH (below 4.8)[1,2] is associated with its protonation. The dialysis was performed in several successive steps to various media. Freeze-drying of micellar solutions provided the samples W, AW and ABW. The sample code describes the dialysis media used successively in the preparation of the samples. The micellar solutions were prepared by direct dissolution in D_2O or 0.1 M DCl. The copolymer concentrations ranged from 2 to 4 mg/mL.

Interpretation of SANS Data

Two different approaches were employed. The first approach is based on fitting the theoretical scattering function of spherical particles with the Schulz-Zimm distribution of radii to experimental SANS data within a properly chosen q-range. The fit provides parameters of the micelle core: mean radius, R_{core}, polydispersity characteristics, σ/R_{core} and M_w/M_n, mean volume, V_{core}. This approach is referred to as *bare-core approximation*[2] (BCA). In our second approach, we fitted the whole SANS curve to the Pedersen-Gerstenberg (P&G) model[4] modified to describe a polydisperse system[2]. In this model it is assumed that the micelle consists of a spherical core to which corona chains are attached. In addition to the core parameters, some characteristics related to the corona can be found from the fit (e.g., radius of gyration of the corona-forming chains, $R_{G,chain}$).

Results and Discussion

To examine the influence of the preparation procedures on the micelle formation, three samples of various histories (W, AW, ABW) were dissolved in D_2O. The sample codes suggest the states of the PVP block during individual preparation steps. While the PS blocks collapse and the PEO blocks swell in aqueous media, the PVP block can swell at low pH (A) or collapsed at high pH (B, W). This means that the structure of the freeze-dried samples with different histories may differ and these structures may be preserved after dissolving in water.

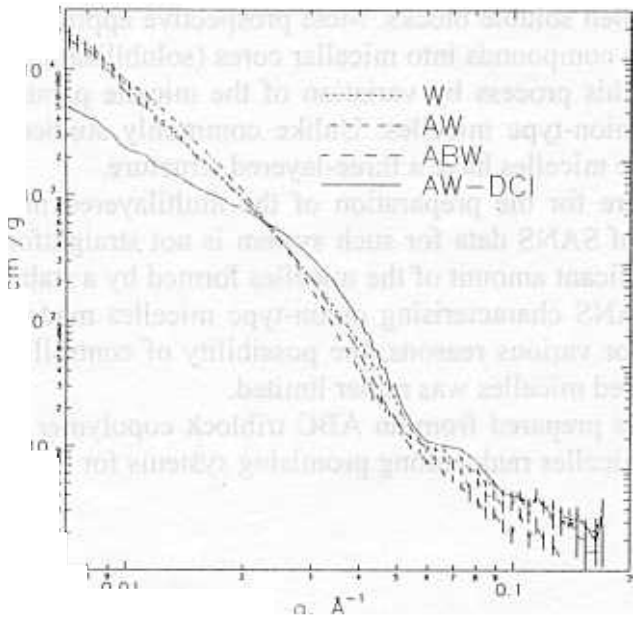

Fig. 1 SANS curves of the PS-*b*-PVP-*b*-PEO in D_2O (samples W, AW, ABW) and in 0.1 M DCl (AW-DCl). For explanation of the codes, see the text.

Figure 1 shows the SANS curves of micellar systems prepared in D_2O from copolymer samples of various histories. The SANS curves do not differ dramatically after normalisation to the unit concentration. This shows that the resulting particles are very similar in D_2O, regardless of their history. However, both approaches to the data (bare-core approximation, P&G model) failed to provide a unique and consistent set of the micelle parameters. This indicates that the particles formed in D_2O are possibly not regular micelles but more complex aggregates.

One (AW) of the samples was dissolved in 0.1 M DCl where, unlike in D_2O, the formation of micelles with expanded PVP block is expected. The shape of the SANS curve (Fig.1) is typical of micellar solutions. The observed scattering maximum may be ascribed to scattering from the micelle core, which gives a predominating contribution at high q's. The enhanced intensity in the innermost part of the SANS curve indicates where the scattering contribution of the micelle corona becomes significant.

An example of pH-induced variation of the micelle structure is given in Fig.2. We measured the SANS curves of the sample AW dissolved in 0.1 M DCl and then repeated the measurement after raising pH by adding of an appropriate amount of NaOH. We can see a pronounced change in the scattering behaviour upon a pH change. The side maximum is shifted to smaller angles indicating larger size of the micelle core. This is the result of a collapse of PVP blocks caused by their deprotonation at high pH.

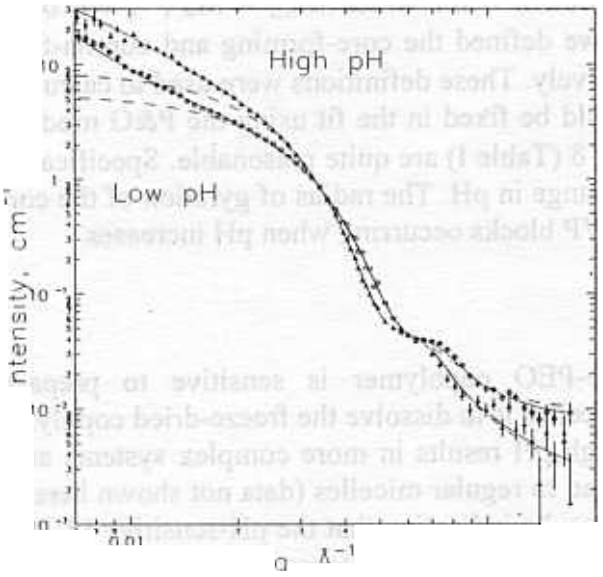

Fig.2 Experimental SANS curves for the PS-*b*-PVP-*b*-PEO copolymer in D_2O media at low pH (O) and at high pH (Δ) along with the theoretical fits using bare-core approximation (dashed lines) and P&G model (solid lines)

The PS-*b*-PVP-*b*-PEO is expected to form micelles with PS blocks in the core and the PEO blocks in the corona. The PVP part may contribute to the core or corona depending on pH. We introduce the parameter δ as a fraction of the PVP block in the collapsed state (and therefore belongs to the core). First we assumed the ideal behaviour be the one characterised by δ=0 at low pH and δ=1 at high pH. The structure parameters are collected in Table I. We can see that the parameters obtained using the BCA approach are in good agreement with the results based on the P&G model. This means that the bare-core approximation works properly for the micelles studied.

A closer inspection of the results, however, reveals some discrepancies. The micellar molar mass calculated in two ways, namely from the core volume ($M_{w,V}$) and from the extrapolated scattering intensity ($M_{w,I}$) are different. Furthermore, the micellar molar mass at low pH is significantly higher than that at high pH. This can hardly be accepted because the PS core is in the glassy state and, therefore, a decrease in the micelle mass upon collapse of PVP blocks is unlikely to occur. Of possible explanations of these discrepancies, the most plausible consists in a nonideal

Table Structure parameters of PS-*b*-PVP-*b*-PEO micelles in aqueous (D_2O) media

	Low pH			High pH		
	BCA[a] (δ=0)[c]	P&G[b] (δ=0)	P&G (δ=0.182)	BCA (δ=1)	P&G (δ=1)	P&G (δ=0.538)
R_{core}, Å	72	74	74	82	81	81
σ/R_{core}	0.19	0.18	0.18	0.17	0.18	0.18
M_w/M_n	1.36	1.29	1.29	1.28	1.30	1.30
$V_{core} \times 10^{-6}$, Å^3	2.4	2.4	2.4	3.2	3.1	3.2
$M_{w,I} \times 10^{-6}$, g/mol	7.5	-	-	3.8	-	-
$M_{w,V} \times 10^{-6}$, g/mol	6.6	6.6	5.7	4.7	4.6	6.0
$R_{G,chain}$, Å	-	253	231	-	129	164

[a] Bare-Core Approximation[2]
[b] Pedersen - Gerstenberg model[4]
[c] δ=fraction of collapsed PVP chain

behaviour of PVP chains. We calculated the values of δ for which $M_{w,I} = M_{w,V}$. We obtained δ=0.18 for low pH and 0.54 for high pH. Then we defined the core-forming and corona-forming block as PS+ δ PVP and (1-δ)PVP + PEO, respectively. These definitions were used to calculate the scattering characteristics of the block, which should be fixed in the fit using the P&G model. The relations between the results for the new values of δ (Table I) are quite reasonable. Specifically, the molar mass did not change significantly upon a change in pH. The radius of gyration of the corona-forming blocks, $R_{G,chain}$, reflects the collapse of PVP blocks occurring when pH increases.

Conclusions

The association behaviour of the PS-*b*-PVP-*b*-PEO copolymer is sensitive to preparation procedures. The most promising way to regular micelles is to dissolve the freeze-dried copolymer in an aqueous medium at low pH. Dissolution at high pH results in more complex systems and the subsequent lowering of pH does not necessarily lead to regular micelles (data not shown here). The two approaches to the SANS data lead to similar results indicating that the pH-sensitive PVP block is probably not completely swollen at low pH and not completely collapsed at high pH. It would be possible to confirm or reject this hypothesis if the SANS data at smaller scattering vectors were available.

This work was supported by the Grant Agency of the Czech Republic (Grant 203/96/1387).

References

1. K.Procházka, T.J.Martin, S.E.Webber, P.Munk *Macromolecules* **29**, 6526 (1996).
2. J.Pleštil, J.Kříž, Z.Tuzar, K.Procházka, Yu.B.Melnichenko, G.D.Wignall, R.Talingting, P.Munk, S..E.Webber " Small-Angle Neutron Scattering Study of Onion-Type Micelles " *Macromolecules*, submitted.
3. J.Kříž, B.Masař, J.Pleštil, Z.Tuzar, H.Pospíšil, D.Doskočilová *Macromolecules* **31**, 41 (1998).
4. J.S.Pedersen, M.C.Gerstenberg *Macromolecules* **29**, 1363 (1996).

NEUTRON DIFFRACTION STUDY OF THERMAL EXPANSION AND COMPRESSIBILITY OF PYRIDINIUM NITRATE AND TETRAFLUOROBORATE

L. Bobrowicz-Sarga [1,2], P. Czarnecki[1], S. Lewicki[1], I. Natkaniec[2,3], J. W1sicki [1]

1) Institute of Physics, A. Mickiewicz University, 61-614 Poznañ, Poland
2) Frank Laboratory of Neutron Physics, JINR, 141980 Dubna, Russia
3) H. Niewodniczañski Institute of Nuclear Physics, 31-342 Krak ó w, Poland

Structural phase transitions of the order-disorder type occur in many simple salts of pyridine (Py=C_5H_5N). In the high temperature phase the pyridinium cation (PyH^+) perform fast in-plane reorientations around its pseudohexagonal C_6 axis between six equivalent potential wells (symmetric potential). However, in low temperature phases the reorientation of the cation takes place around an analogous axis between nonequivalent potential wells (asymmetric potential). Pyridinium tetrafluoroborate ($PyHBF_4$), perrhenate ($PyHReO_4$) and perchlorate ($PyHClO_4$) were found to show ferroelectric properties [1,2,3]. Phase transitions in both ferro- and non-ferroelectric pyridinium salts are related to ordering of pyridinium cations and anions in the crystal. The difference is that ferroelectric salts undergo two phase transitions, while non-ferroelectric salts undergo only one solid-solid transition.

The $PyHBF_4$ undergoes two structural phase transitions at 238.7 and 204 K. At 238.7 K the ferroelectric crystal transforms from $R\bar{3}m$ into C2 symmetry, and at 204 K into the space group P2 [1]. This compound is a unique example of continues ferroelectric phase transitions in multidirectional ferroelectrics [4]. In the disordered ferroelectric phase of $PyHBF_4$ the pyridinium cation reorients by jumping in a symmetric potential and the planes of pyridinium cations are arranged in parallel, which implies a considerable anisotropy of physical properties. In the low-temperature phases the potential wells for reorientation of the piridinium cation become nonequivalent. Significant differences in the structure of $PyHBF_4$ and $PyHNO_3$ were established.

Pyridinium nitrate ($PyHNO_3$) crystallise in the monoclinic system $P2_1/c$ [5]. The $PyHNO_3$ does not undergo the solid-solid phase transition most probably because of the presence of a strong hydrogen bonds in this compound. The planes of the pyridinium cations are not parallel in the monoclinic system, so the anisotropy of physical properties should be smaller. In the $PyHNO_3$, the cation performs jumps between nonequivalent potential wells.

We applied the time -of-flight neutron powder diffraction method to complement the information on the crystal lattice dimensions of the $PyHBF_4$ and $PyHNO_3$ as a function of temperature and pressure. The results permit determination of the thermal expansion coefficients α and compressibility β, as well as relations between these coefficients and the structures of $PyHBF_4$ and $PyHNO_3$. The values of α and β are also necessary to determine the thermodynamic state of these compounds.

Neutron scattering experiments were performed by the time of flight method on the NERA-PR spectrometer [6] installed at the IBR-2 high flux pulsed reactor of the JINR in Dubna. This spectrometer operates in the inverted geometry and permits simultaneous recording of neutron diffraction (ND) spectra for sixteen scattering angles in the angular sectors of (20° - 80°) and (100° - 160°) as well as incoherent inelastic neutron scattering (IINS) spectra for sixteen scattering angles in the range 20° - 160°. The flight path of 109 m from the reactor core to the spectrometer allows a good resolution of ND spectra, $\Delta d/d$ = (0.2 - 1)% for the lattice spacing in the range of (1 - 7) A.

The studied polycrystalline samples at ambient pressure and different temperatures ware placed in the cryostat cooled by closed-cycle helium refrigerator permitting temperature changes from 10 K to 300 K within an accuracy of 0.5 K. Measurements of ND spectra as a function of

hydrostatic pressure were performed on the same spectrometer with the aid of the high pressure set-up [7]. The high pressure gaseous helium arrangement consists of a U11-GC gas compressor, GNC-400 high-pressure cell and a top loaded type cryostat. The U11-GC (UNIPRESS, Warsaw) gas compressor is a laboratory high-pressure arrangement generating pressure up to 1500 MPa in gases. This compressor is designed for the use with helium; however, any inert gas can be used as the pressure transmitting medium. The cylindrical high pressure gas neutron cell GNC-400, (Φ=6cm, h=22cm), made from aluminium alloy was developed for investigations of the structure and dynamics of molecular crystals by the neutron scattering method under a high pressure up to 400 MPa. It is connected to a gas compressor by a beryllium-cooper capillary and arranged inside a top-loaded cryostat cooled by liquid nitrogen with adjustable temperature in the range of 78 - 350 K. The working volume ca. 22 cm^3, (Φ=1.6 cm, h=10 cm), of the high pressure cell is fully used for deuterated samples. A polycrystalline sample of hydrogeneous substance to be studied is cylindrically shaped by an additional aluminium container inserted into the high-pressure cell. The use of helium gas as a pressure transmitting medium enables the achievement of purely hydrostatic conditions inside the cell in a wide temperature range down to ca. 20 K.

The examples of the ND spectra of $PyHBF_4$ and $PyHNO_3$ measured in different experimental conditions are presented in Fig. 1 and Fig. 2. Despite a significant background due to incoherent neutron scattering on hydrogen atoms (especially seen for large scattering angles), the ND spectra exhibit characteristic diffraction peaks, which permits conclusions about the occurrence of phase transitions in the studied samples.

Figure 1. presents neutron diffraction spectra of a polycrystalline $PyHBF_4$ sample at 260 K (phase I), 220 K (phase II) and 180 K (phase III). The I $\Leftrightarrow$ II phase transition is marked by a splitting and shifting of the diffraction peaks. The II $\Leftrightarrow$ III phase transition is connected with a change in the space group in the monoclinic symmetry of these phases. The inserted figure presents the evolution of the position and shape of the (-110) reflection (in the phase I) at phase transitions. The splitting of this reflection is caused by a change in the symmetry from trigonal system to monoclinic system at structural ferroelectric phase transition.

The influence of the high pressure set-up on the powder neutron diffraction spectra for $PyHNO_3$ is illustrate in Fig. 2. A noticeable shift of strong diffraction peaks is caused by a decrease of lattice constants under high pressure. However, low intensity reflections are lost in the increased background from the high pressure cell which, by absorption in the walls, decreases the intensity of the neutrons scattered on the sample, as well. At high pressure conditions, deuterated samples of the investigated compounds have been also measured, in order to increase the ratio of the ND intensity to the background of the high pressure-set-up.

The neutron diffraction spectra recorded between 12 and 290 K for ambient pressure and in the temperature range of 78 - 290 K at higher pressures were used for determining the unit cell thermal expansion and isothermal compressibility of $PyHBF_4$ and $PyHNO_3$ crystals. The values of the unit cell parameters: a, b, c, β and volume (V), were refined by the least squares method from the positions of about twenty five independent reflections. The values of the elementary unit cell volumes for both compounds calculated in monoclinic system notation of lattice parameters, are presented in Fig.3, Fig.4, Fig.5, and Fig.6, as functions of pressure and temperature.

The influence of high pressure on the elementary unit cell volume of $PyHNO_3$ is practically the same for whole temperature range of 78 -290 K. The absolute value of the slope of the $V_T(p)$ curves, presented in Fig.4 decreases with increasing pressure. A similar behaviour of the pressure dependence of $V_T(p)$ can be noticed for the phase I and II of $PyHBF_4$. However, for the low temperature phase III, the absolute value of the slope of the corresponding $V_T(p)$ curve increases with increasing pressure, as one can see in Fig.3.

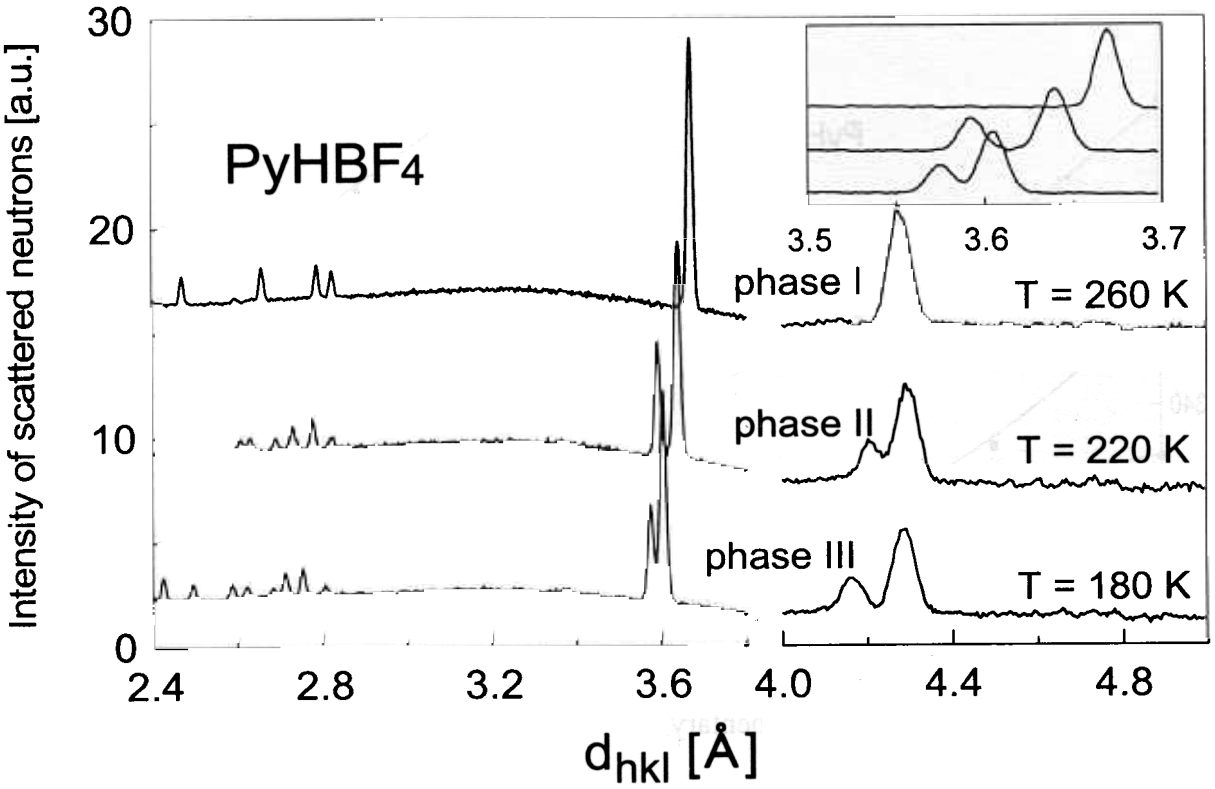

Fig. 1.Neutron powder diffraction spectra of three solid phases of piridinium tetrafluoroborate measured at the scattering angles $2\Theta=135^{o}$ (left side spectra) and $2\Theta=68.6^{o}$ (right-side spectra).

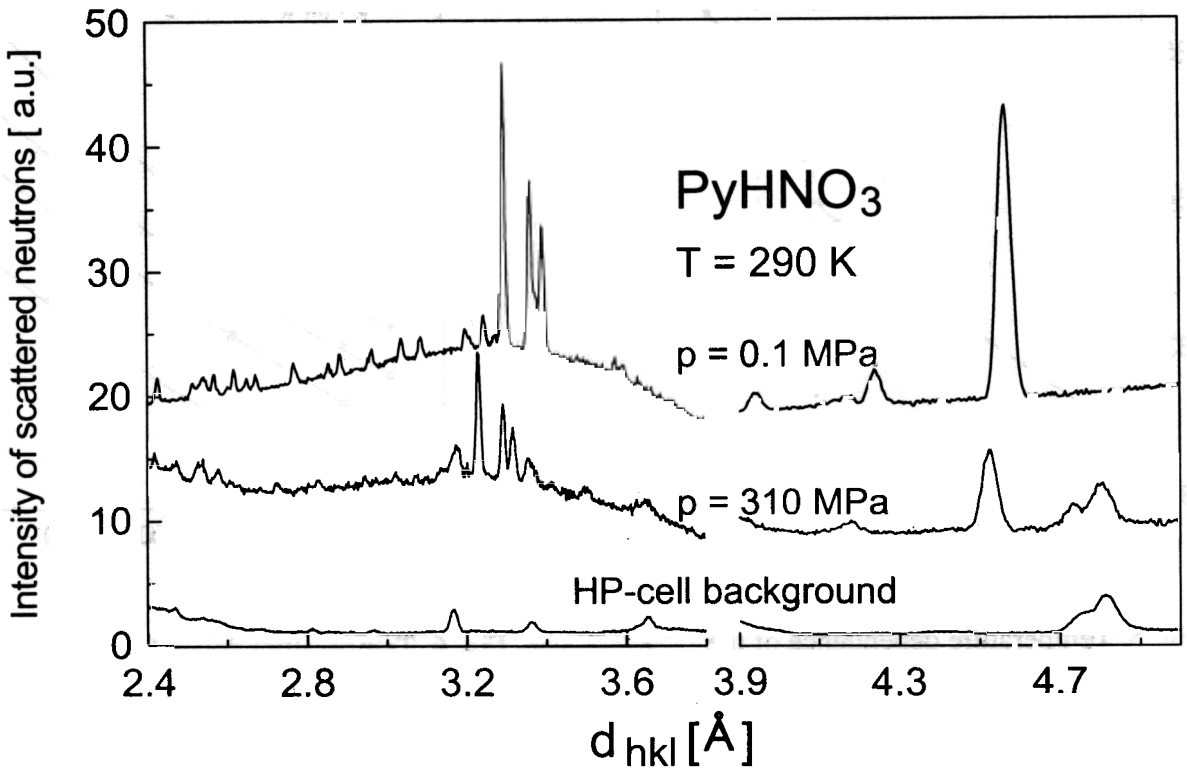

Fig. 2. Neutron powder diffraction spectra of piridinium nitrate measured within a close-cycle helium refrigerator cooling set-up at ambient pressure (upper spectra at p = 0.1MPa) and within the high pressures set-up (middle spectra at p = 310 Mpa).

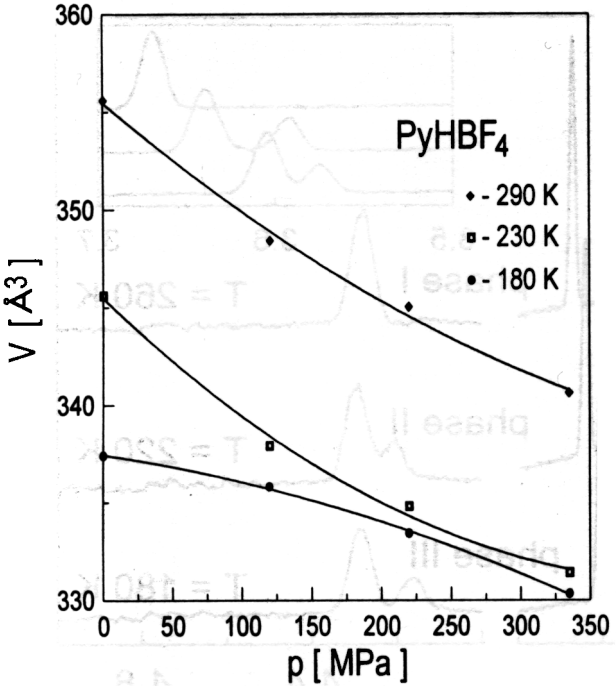

Fig. 3. Pressure dependence of the elementary unit-cell volume of $PyHBF_4$.

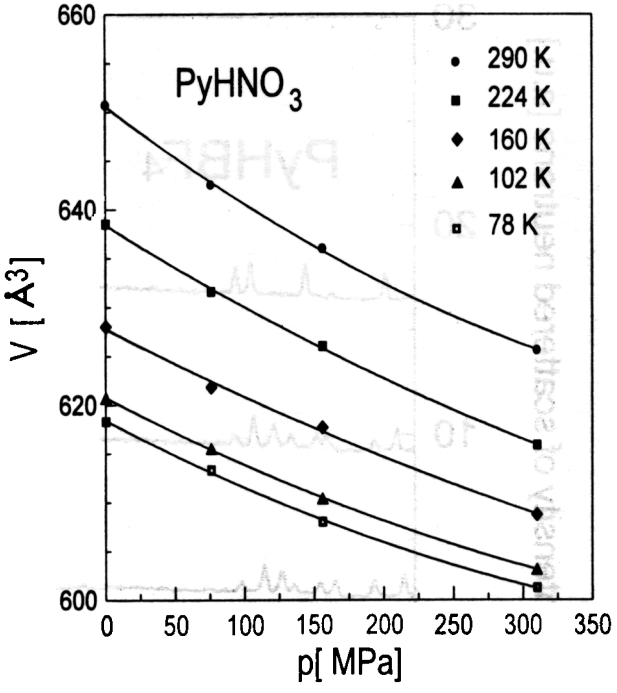

Fig. 4. Pressure dependence of the elementary unit cell volume of $PyHNO_3$.

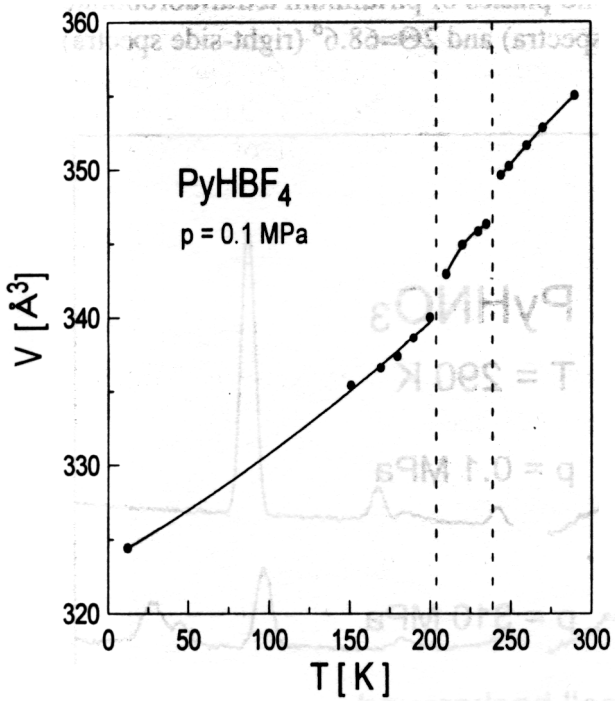

Fig. 5. Temperature dependence of the elementary unit cell volume of $PyHBF_4$.

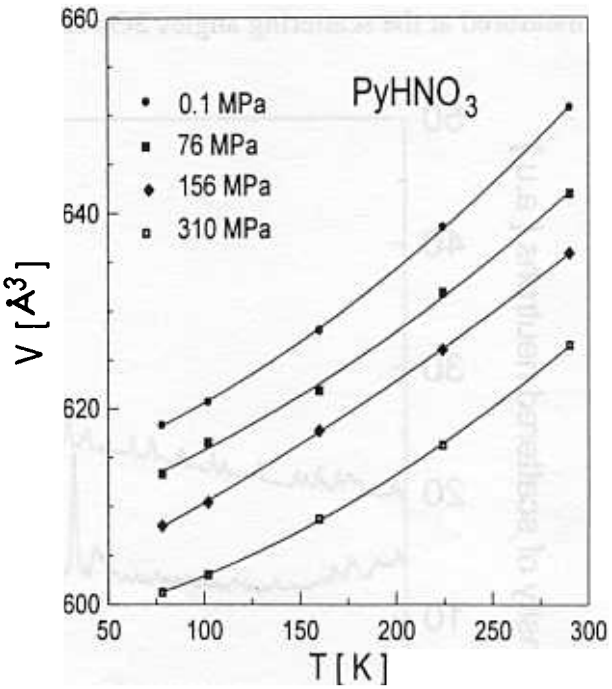

Fig. 6. Temperature dependence of the elementary unit cell volume of $PyHNO_3$.

The temperature dependence of the elementary unit cell volume of $PyHBF_4$ at ambient pressure is presented in Fig.5. The phase transitions in this crystal correspond to small jumps of the elementary unit cell volume. The slope of the $V_p(T)$ curve of phase I and II is larger than for phase III. In the case of $PyHNO_3$, the slope of the corresponding $V_p(T)$ curves continuously decreases with decreasing temperature, as one can see in Fig. 6. The values of the isobar thermal expansion coefficient α and the isothermal compressibility coefficient β determined for $PyHNO_3$ and $PyHBF_4$, by the relative slope of the corresponding $V_T(p)$ and $V_p(T)$ curves, are summarised in the Table 1.

Table The isobar thermal expansion and isothermal compressibility coefficients for three phases of $PyHBF_4$ and $PyHNO_3$.

		$\alpha=1/V(dV/dT)_p$ [1/K] x10^{-3}	$\beta=-1/V(dV/dp)_T$ [1/MPa] x10^{-3}
$PyHBF_4$	phase I	0.469 (p=0.1 MPa)	0.143 (p→0.1 MPa, T=290 K)
	phase II	0.662 (p=0.1 MPa)	0.150 (p→0.1 MPa, T=230 K)
	phase III	0.460 (p=0.1 MPa)	0.054 (p→0.1 MPa, T=180 K)
$PyHNO_3$		0.281 (p=0.1 MPa)	0.129 (p→0.1 MPa, T=230 K)

The value of the thermal expansion coefficient of piridinium nitrate is smaller than the corresponding values of piridinium tetrafluoroborate crystals. It might be due to the presence of hydrogen bonds in $PyHNO_3$, which should be less important in $PyHBF_4$ crystals. One can also note a relatively small value of the compressibility coefficient of the phase III of $PyHBF_4$. The thermodynamic equations of state of $PyHBF_4$ and $PyHNO_3$ crystals under investigations will be discuss in more details in a following publications.

Acknowledgements

The authors express their sincere thanks to Mr. T.Sarga and Mr. S.I. Bragin for their assistance in neutron scattering measurements.

References

[1] P. Czarnecki, W. Nawrocik, Z. Pajak and J. Wasicki, Phys. Rev. **B 49**, 1511 (1994)
[2] P. Czarnecki, W. Nawrocik, Z. Pajak and J.Wasicki, J. Phys. C **6,** 4955 (1994)
[3] J. Wasicki, P. Czarnecki, Z. Pajak, W. Nawrocik and W. Szczepanski, J. Chem. Phys. **107**, 576 (1997)
[4] P. Czarnecki, A. Katrusiak, I. Szafraniak and J. Wasicki, Phys. Rev. **B 55**, 3326 (1998)
[5] A.J. Serewicz, B.K. Robertson, E.A. Mayers, J. Phys. Chem., **69** 1915 (1965)
[6] I. Natkaniec, S.I. Bragin, J. Brankowski, J. Mayer, Proc. ICANS XII, Abingdon, 1993, RAL Report 94-025, Vol. I, p. 89-96.
[7] S. Habrylo, S.I. Bragin, J. Brankowski, W. Iwanski, J. Mayer, I. Natkaniec, W. Nawrocik, K. Zawalski, High Pressure Research, **4** 457 (1990)

NEUTRON SCATTERING STUDY OF THE LIQUID HELIUM EXCITATION SPECTRUM

V.Bogoyavlenskii[1], A.V.Puchkov[2], A.N.Skomorokhov[3]

[1]*Kharkov Institute of Physics and Technology, Kharkov, Ukraine;*
[2]*Institute of Physics and Power Engineering, Obninsk, Kaluga Region, Russia;*
[3]*Joint Institute for Nuclear Research, Dubna, Moscow Region, Russia.*

A neutron scattering experiment on the spectrometer DIN-2PI was oriented towards the study of a phonon-maxon region of the liquid helium excitation spectrum. One of the aims of the experiment was to verify the existence of a zero-sound mode in the maxon region. To solve this problem, the measurement was focused on temperatures quite close to the superfluid transition temperature, as expected by Glyde and Griffin [1,2] and from experimental results [3,4].

$S(Q,\omega)$ of liquid ^{4}He was measured at T=1.53; 1.81; 1.96; 2.1; 2.22K covering the wavevector range from 0.2 to .2Å^{-1}. To obtain the resolution function, measurements at a low temperature were also carried out. A low initial neutron energy (2.37meV) and reduced angular uncertainties provide an instrumental resolution between 0.105 and 0.07meV (FWHM) as a function of the scattering angle.

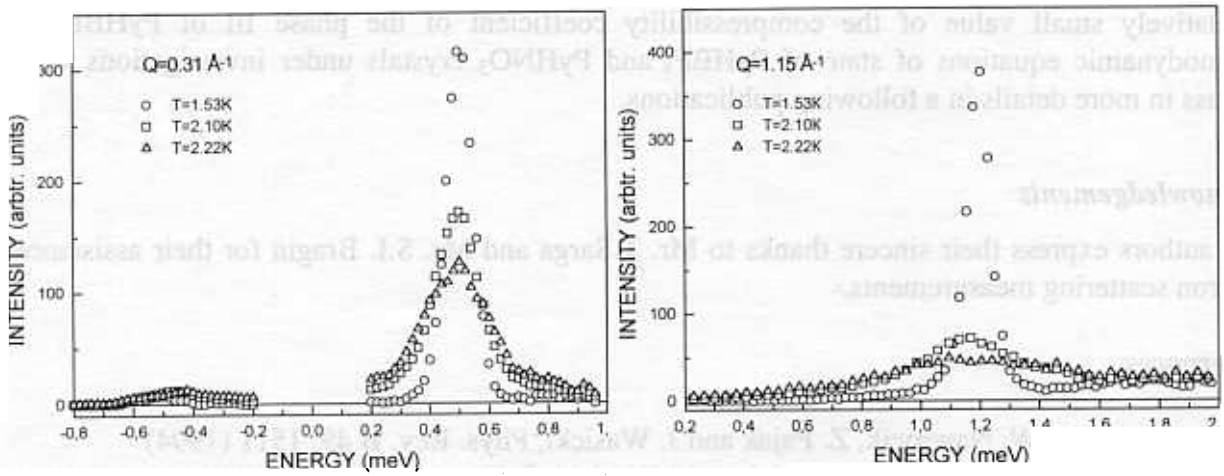

Fig.1 Temperature dependence of S(Q,ω) at Q=0.31 and 1.15 Å^{-1}

It is found that the temperature dependence of $S(Q,\omega)$ depends notably on Q. At $Q<0.5$Å^{-1}, the phonon broadens as the temperature increases though retains a well-defined excitation above T_λ. The peak position varies slightly with temperature. In the maxon region (Q about 1.0Å^{-1}) the temperature dependence is quite different. Maxon change abruptly at T_λ, leaving no sharp peak at temperature above. In the Q region from 0.5 to 0.8Å^{-1}, $S(Q,\omega)$ exhibits additional intensities at $\omega>\omega_0$, that increase with temperature. This peculiarity can be explained as the temperature dependence of the interference terms of $S(Q,\omega)$ or the remnant zero sound mode.

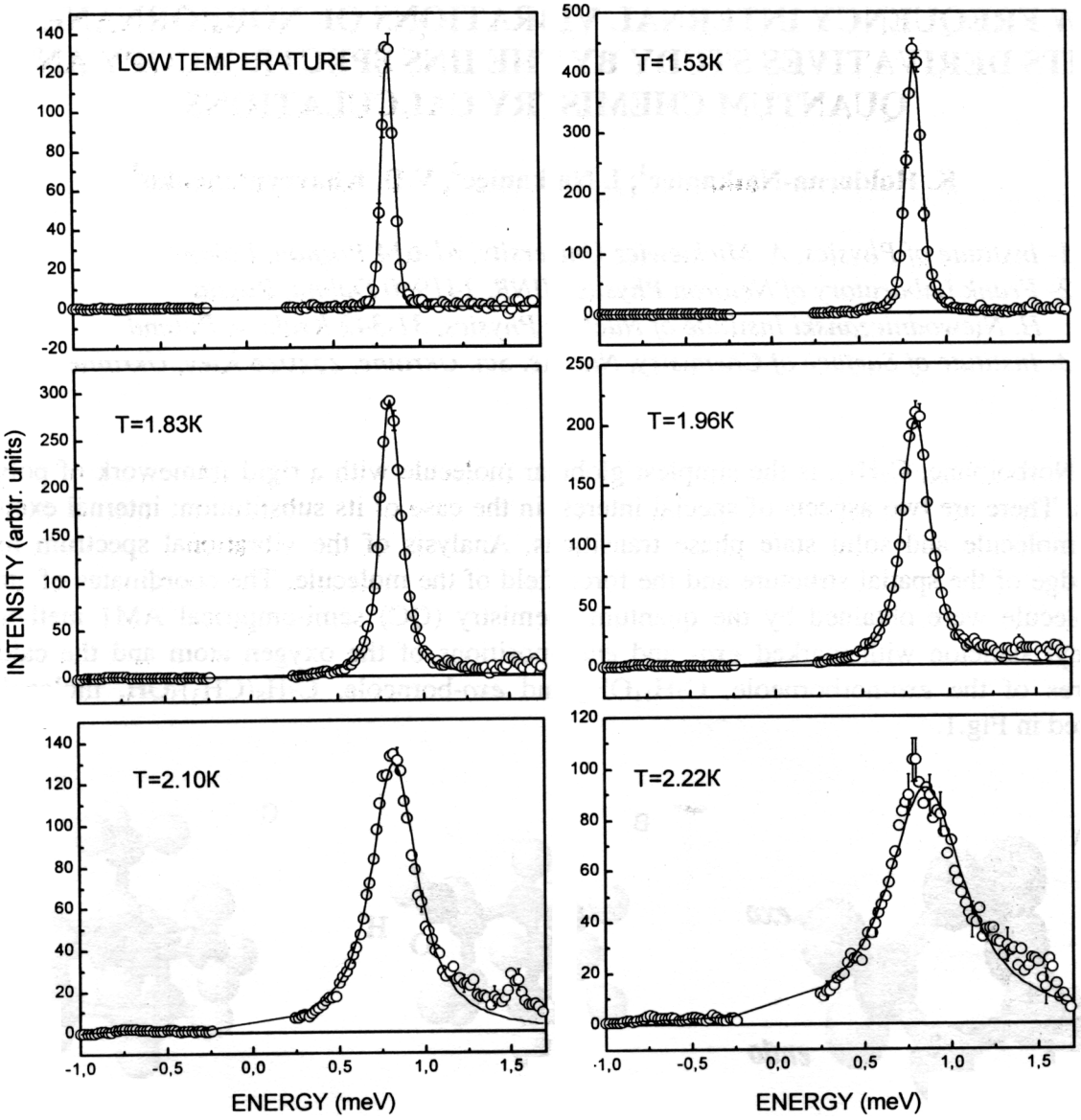

Fig.2. Temperaure dependence of S(Q,ω) at Q=0.51 $Å^{-1}$. Solid lines represent best fits to the data obtained by convolution of the resolution function and the function a damped harmonic-oscillator.

REFERENCES

[1] H.Glyde, Exitations in liquid and solid helium, Clarendon Press.,Oxford,(1994)

[2] H.R.Glyde and A.Griffin, Phys.Rev.Lett.**65**(1990),1454

[3] R.M.Crevcoeur, H.M.Smorenburg, I.M. de Schepper, W.Montfrooij and E.C.Svensson, Czech. J. of Phys.**46**(1996)257

[4] I.V.Bogoyavlenskii, A.V.Puchkov, A.N.Skomorokhov and S.V.Poupko, Physica B **234-236**(1997)324.

LOW FREQUENCY INTERNAL VIBRATIONS OF NORBORNANE AND ITS DERIVATIVES STUDY BY THE IINS SPECTROSCOPY AND QUANTUM CHEMISTRY CALCULATIONS

K. Holderna-Natkaniec[1], I. Natkaniec[2], V.D. Khavryutchenko[3]

1- Institute of Physics, A. Mickiewicz University, 61-614 Poznan, Poland
2- Frank Laboratory of Neutron Physics, JINR, 141980 Dubna, Russia
H. Niewodniczanski Institute of Nuclear Physics, 31-342 Krakow, Poland
3- Institute of Surface of Chemistry, Nat. Ac. Sci. Ukraine, 252028 Kiev, Ukraine

Norbornane, C_7H_{12}, is the simplest globular molecule with a rigid framework of polycyclic alkanes. There are two aspects of special interest in the case of its substitution: internal excitations of the molecule and solid state phase transitions. Analysis of the vibrational spectrum requires knowledge of the spatial structure and the force field of the molecule. The coordinates of atoms in the molecule were obtained by the quantum chemistry (QC) semi-empirical AM1 method. The norbornyl skeleton with marked *exo*- and *endo*-positions of the oxygen atom and the calculated structures of the *exo*-norborneole, $C_7H_{11}OH$, and *exo*-borneole, $C_7H_8(CH_3)_3OH$, molecules are presented in Fig.1.

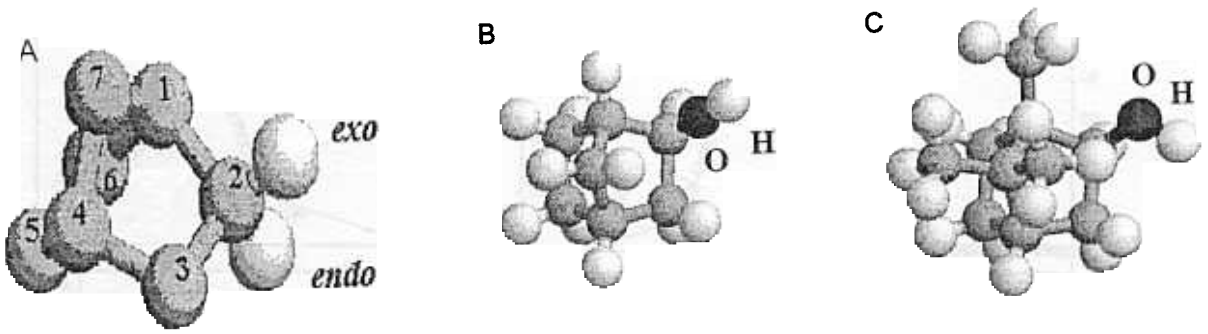

FIG. 1. The norbornyl skeleton and used notation for carbon atoms - (A), the calculated structures of *exo*-norborneole - (B) and *exo*-borneole - (C) molecules.

The calculated lengths of intramolecular C-C bonds of norbornane are in the range from 1.49 to 1.57 A and the C-O, O-H and C-H bonds are equal to 1.47, 0.95 and 1.11 A, respectively. The bond lengths obtained experimentally by the x-ray and electron diffraction methods [1] are close to the above values. The C1-C7-C4 bridge angle of norbornane calculated by the AM1 method gives the value of 93° and is close to the diffraction data - 96° [1].

The force field was determined in the Cartesian system of coordinates as a matrix of the second derivatives of the total energy of the molecule with respect to atom displacements [2,3]. On the basis of the atom coordinates and the force field the frequencies of particular modes and their intensities in the INS spectrum were obtained. The frequencies calculated for an isolated molecule of norbornane, its qualitative assignment with a potential energy distribution (PED) and the experimentally obtained frequencies are summarised in Table 1. These frequencies differ by about 10%. The calculated frequencies were fitted to their experimental values by solving the full matrix inverted vibration problem [4]. The fitted neutron intensities are shown by bars in Fig. 2. The calculated IINS spectra were obtained by the convolution of these δ-functions with the resolution function of the NERA spectrometer [5] in the approximation of one-phonon neutron scattering cross-section. Finally, the transformation of the calculated and experimental IINS spectra to the

G(ω) amplitude weighed phonon density of states was performed. The G(ω) functions are compared in Fig.2.

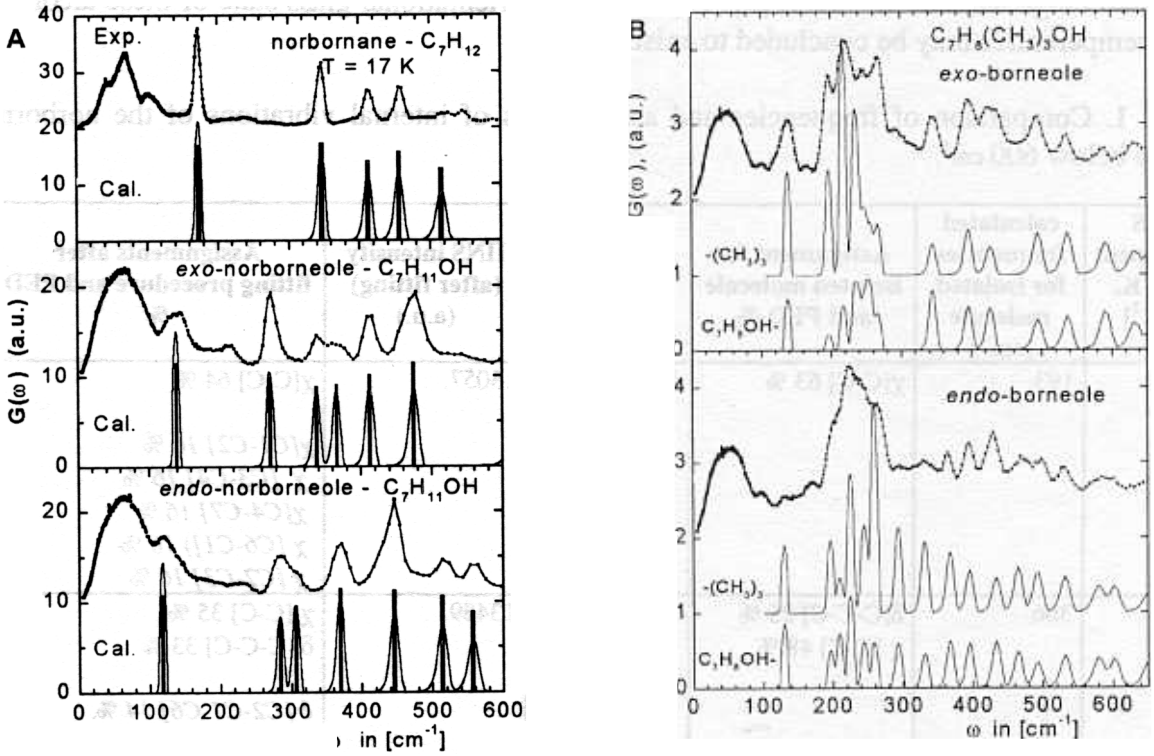

FIG. 2. **A** - The experimental G(ω) at 17 K (Exp.) and calculated (Cal.) spectra of low- frequency internal vibrations for norbornane, *exo-* and *endo*-norborneole molecules. **B** - comparison of the experimental G(ω) at 17 K of *exo-* and *endo*-borneole with the partial $G_H(\omega)$ density of states calculated for three methyl groups and the C_7H_8OH skeleton of borneole molecules.

The fitted low-frequency vibrations of the norbornane molecule and qualitative assignment of subsequent modes are presented in Table 1. Particular modes with the PED greater than 10% are marked by *italics*. Each of these low frequency internal vibrations is a combination of several torsions: stretching (ν), bending in-plane (δ) and bending out-of-plane (χ). The bands appearing in the low-frequency spectrum of norbornane can be interpreted as corresponding to the breath vibrations of the skeleton at 173 cm^{-1}, and subsequently the out-of-plane and in-plane bendings as in Table 1. The skeleton deformation modes of *exo-* and *endo*-norborneole were mainly shifted towards lower frequencies in comparison to those observed for norbornane. For both norborneole molecules the out-of-plane bending χ[CO] at 338 cm^{-1} and 369 cm^{-1}, and in-plane bendingss δ [CCO] at 272, 366 cm^{-1} and 284, 369 cm^{-1}, for *exo-* and *endo*-forms, respectively, were observed.

The G(ω) spectra of norborneole substituted at 1.7.7 by methyl groups i.e. *exo-* and *endo*-borneole are compared in Fig. 2 B with the results of the calculations. The calculated results are presented as partial spectra of a C_7H_8OH skeleton and three methyl groups. The out-of-plane vibrations of methyl groups were observed in the range 190 - 400 cm^{-1}. These vibrations are mixed with the skeleton ones. It was found that the lines corresponding to the torsional vibration involving any atoms from the hydroxyl group were close to 260 cm^{-1}, and those attributed to the deformational modes δ[CCC-O] are close to 350 - 480 cm^{-1}.

The half-width of the peaks in the experimental spectrum of norbornane, in the region up to 600 cm^{-1}, is practically similar to the resolution function of the spectrometer. Broadening of subsequent bands much over the resolving power of the spectrometer as well as overlapping of the low-frequency internal modes and the lattice ones, especially for *endo*-borneole is shown in Fig. 2. The wide bands of low frequency internal vibrations and the structureless lattice vibration density of

states below ca. 100 cm^{-1} lead to the conclusion about that the orientational disorder of molecules in the low-temperature phase of the studied norborneole alcohols is frozen. The neutron diffraction pattern for *endo*-norborneole and *endo*-borneole does not indicate the phase transition in the temperature range from 17 to 300 K [6]. Therefore, the orientational glass state of these alcohols in the low-temperatures may be concluded to exist.

TABLE 1. Comparison of frequencies and assignments of internal vibrations of the norbornane molecule below 600 cm^{1}.

IINS experiment at 17 K. [cm^{-1}]	calculated frequencies for isolated molecule [cm^{-1}]	Assignment for isolated molecule and PED %	Fitted frequencies [cm^{-1}]	IINS intensity (after fitting) (a.u.)	Assignments after fitting procedure and PED %
173	193.	χ[C-C] 63 %	173.	13057.	χ[C-C] 64 % *χ[C1-C2] 16 %* *χ [C3-C4] 16 %* *χ[C4-C7] 16 %* *χ [C6-C1]) 16 %* *χ [C2-C3] 16 %*
347	366.	δ[C-C-C] 25 % χ [C-C] 48 %	346.	13489.	χ [C-C] 35 % δ [C-C-C] 33 % *δ [C2-C1-C6] 14 %.* *δ [C3-C4-C7] 14 %* *χ [C1-C2] 8 %* *χ [C3-C4] 8 %* *χ [C4-C7] 8 %*
411	439	δ[C-C-C6] 75 %	406.	11034.	δ [C-C-H] 38 % *δ [C1-C6-H16]* *δ [C1-C6-H17]* *δ [C4-C7-H8]* *δ [C4-C7-H9]*
456	481.	δ[C-C-C7] 42 %	455.	11163.	δ[C-C-C7] 50 % χ [C-C7] 26 % *χ[C1-C3] 13 %* *χ [C13-C4] 13 %* *δ [C2-C1-C3] 12 %* *δ [C6-C1-C3] 12 %* *δ [C3-C4-C3] 12 %*
516	611	δ[C-C-C] 66 %	516.	12894.	δ $[C\text{-}C\text{-}C]_{skeleton}$ 62 % *δ[C2-C1-C6] 25 %* *δ [C3-C4-C7] 25 %*

References:

1. de Carneiro J.W., Seidl P.R., J.Mol.Struct, **152** (1987) 281.
2. Smith J.C., Karplus K., J.Amer.Chem.Soc, **114**(3) (1992) 201.
3. Dewar M.S.J., J.Molec.Struct, **43** (1978) 135.
4. Khavryutchenko V.D., The COSPECO complex of programs to computed vibrational spectroscopy Institute of Surface Chemistry, Nat. Ac. of Science Ukraine, Kiev, 1990.
5. Natkaniec I, Bragin S.I., Brankowski J., Mayer J., Proc. ICANS XII, Abingdon 1993, RAL Report 94-025, Vol. I., p. 89-96.
6. Holderna-Natkaniec K., Natkaniec I., Proc. XI Polish Conf. Molec. Cryst, Gdansk 1998.

NEUTRON STUDY OF DYNAMIC ATOMIC CORRELATIONS IN AMORPHOUS ISOTOPIC Ni-B ALLOYS

S.N. Ishmaev*, Y.V. Lisichkin **, A.V.Puchkov**,
V.A. Semenov**, E. Svab ***, G.F. Syrykh*

* *RRC Kurchatov Institute, 123182 Moscow, Russia*
** *Institute of Physics and Power Engineering, 249020 Obninsk, Russia*
*** *Research Institute for Solid State Physics, Budapest, Hungary*

The dynamics of metallic glasses $^{i}Ni_{65}{}^{11}B_{35}$ is investigated by the inelastic slow neutron scattering method on isotopic substituted (i= natural, 60 and <b>=0) samples using the time-of-flight spectrometer DIN-2PI at the pulsed reactor IBR-2 in Dubna, and earlier at reactor IR-8 in Moscow [1]. The density of vibration states splits into two distinct regions: 0-40 and 40-90 meV, corresponding to predominant vibrations of heavy (Ni) and light (B) atoms (Fig.1). The first results obtained on the spectrometer DIN-2PI on the Q-dependence of the dynamic structure factor $S(Q,\varepsilon)$ at fixed energies (Fig.2) show small deviations from the Q^2 behaviour possibly due to short range structure and dynamic atomic correlations.

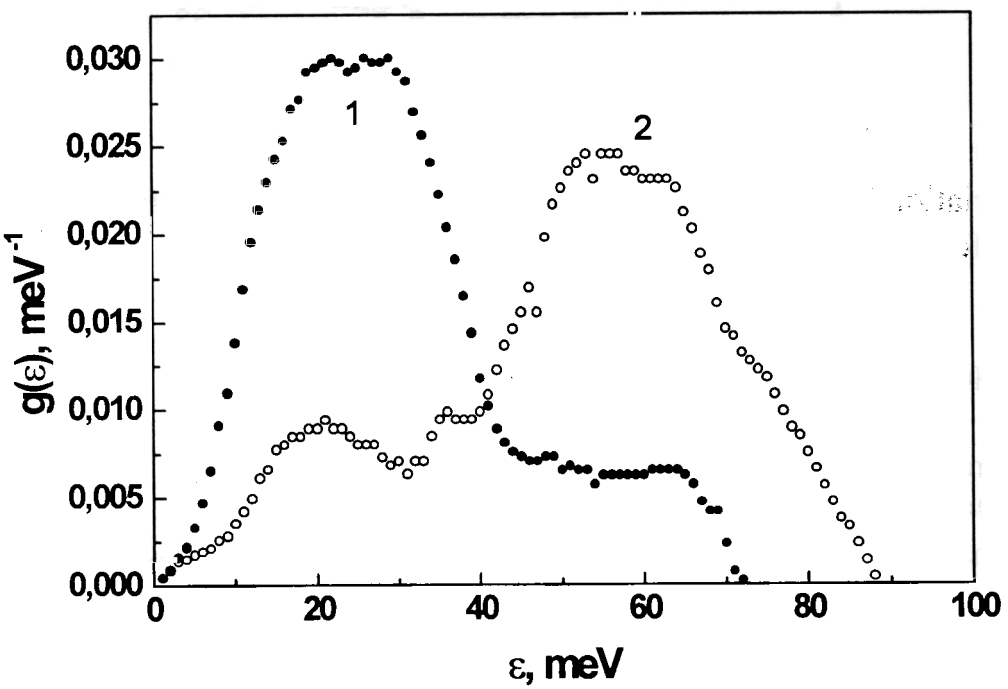

Fig.1 Partial densities of vibration states of Ni (curve 1) and B (curve 2) atoms in the amorphous alloy $Ni_{65}B_{35}$.

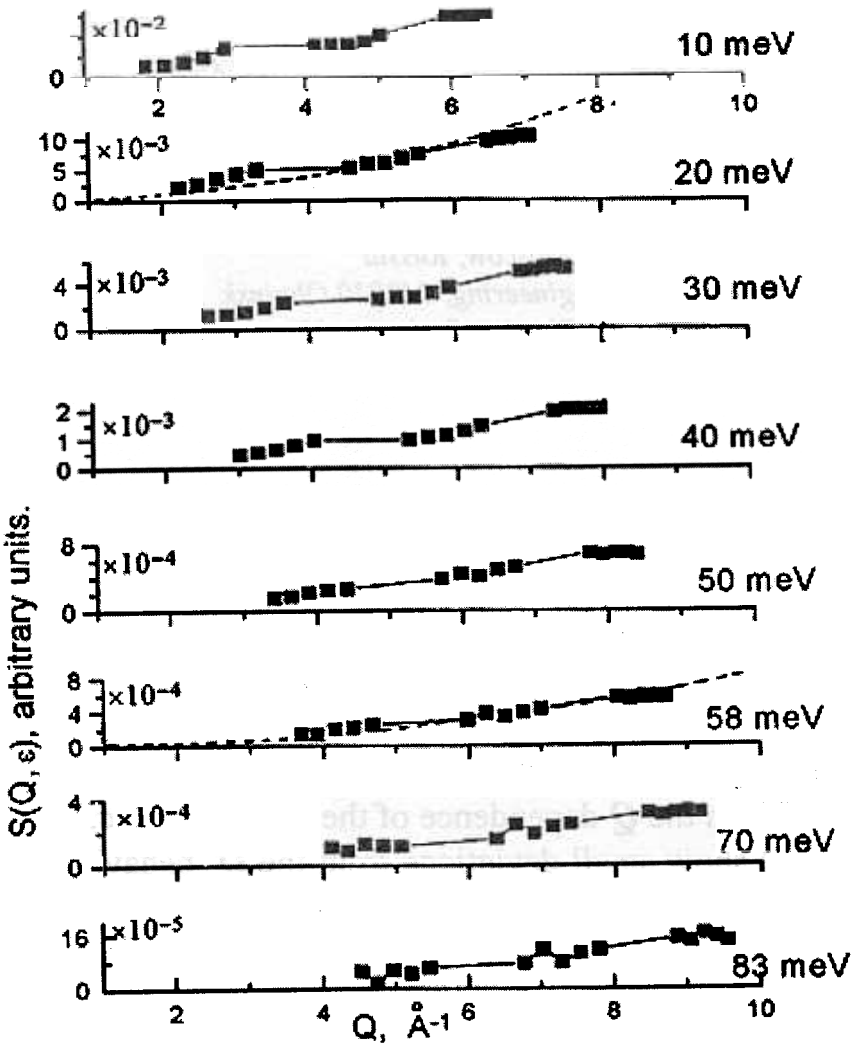

Fig.2 Q variations, $S(Q)$, for the amorphous alloy $Ni_{65}B_{35}$ at different energy transfers ε [2].

REFERENCES

1. M.G.Zemlyanov, G.F.Syrykh, N.A.Chernoplekov and E.Svab, ZhETP,94(1998)365 (in Russian).
2. S.N.Ishmaev, Yu.V.Lisichkin, A.V.Puchkov, V.A.Semenov, E.Svab and G.F.Syrykh, Proc.of 6-th European Powder Diffraction Conference EPDIC-6, Aug.22-25, Budapest, Hungry,1998.

ON HYDROGEN LOCALIZATION IN THE β' PHASE OF $VO_{0.2}$

S. I. Morozov
Physics and Power Engineering Institute, State Science Center of the Russian Federation, Obninsk, Russia

The objective of the present work was to trace by the INS method the effect of oxygen at high concentrations on the dynamics and position of hydrogen localization in the host lattice. To this end, samples of the alloys $VO_{0.2}$ and $VO_{0.2}H_{0.05}$ were prepared and measurements of the INS spectra were performed on a DIN2-PI spectrometer [1]. The result is displayed in Fig. 1.

Since interstitial atoms interact mainly with the nearest-neighbor metal atoms, the structure of the local vibrations (LVs) should be directly related with the symmetry of the interstitial position occupied by the interstitial atom. As one can see from Fig.1, the spectrum consists of a principal feature at ε=86 meV and a small feature at ε_1= 28 meV. The latter feature is due to the band modes of the hydrogen atoms in the $VO_{0.2}$ lattice. The fine lines in Fig.1 show the peaks identified in the spectrum by a best fit of Gaussian curves to the experimental data.

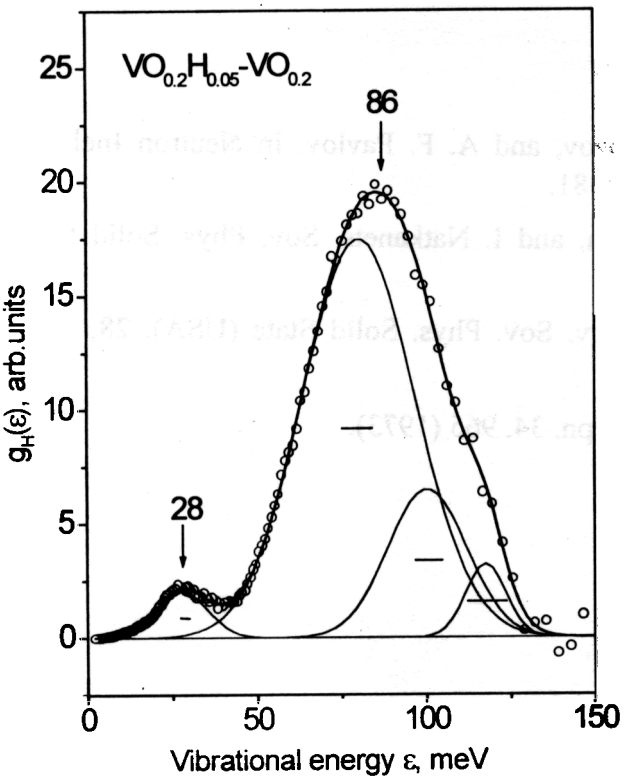

FIG. 1. Vibrational spectrum of hydrogen atoms in the interstitial β' phase of $VO_{0.2}H_{0.05}$. The peaks shown by the fine lines were extracted from the spectrum by fitting Gaussian curves to the experimental data. The thick solid line shows the total result of the description. The positions of the features marked by arrows are given in meV. The horizontal bars show the half-width of the resolution function of the spectrometer.

Such a structure is a typical of the vibration spectrum of light interstitial impurities in the fcc or ideal hcp lattice of the host atoms, where the *T* and *0* positions have T_d and O_h, point symmetry, respectively, while such a low vibrational energy of the H atoms is usually interpreted as evidence of octahedral coordination of hydrogen [2,3]

The character of the regular displacements of the vanadium atoms in the 16(*m*) positions in the $4V_{16}O_3$ superstructure [4], caused by the ordered arrangement of the oxygen atoms, is such that octahedral interstices with O_h symmetry (or weak tetragonal distortion) which are available to hydrogen do not form in it. At the same time, because the vanadium atoms are displaced along the *z* axis by δ=0.54Å some tetrahedral voids in this lattice, are appreciably larger in size than the TPs in pure vanadium and they possess the

symmetry of an almost ideal tetrahedron. If they are occupied by light interstitial atoms, the spectrum of local vibrations should be either degenerate or weakly split. Therefore we arrive at the conclusion that the character of the local displacements of the vanadium atoms changes at a transition from the α to the β phase of V-O. Ordering of oxygen in the β'-phase results in regular displacements of a definite fraction of vanadium atoms. In the process, interstices with T_d local symmetry, which are most favorable for hydrogen atoms, are formed near the oxygen atoms. This result could also be important for interpreting the results of investigations of the vibrational spectrum of hydrogen in other ternary systems, for example, Ta-N-H and V-N-H, where the energy of the triply degenerate localized vibrations of the hydrogen atoms is ε=110 meV [5].

This work was supported by the Russian Fund for Fundamental Research, Project 95-02-04675-a, and the Russian State Program "Topical Problems in Condensed Matter Physics" in the subfield "Neutron Investigations of Matter."

1. Parfenov, P. S. Klemyshev. I. G. Morozov, and A. F. Pavlov. in Neutron Inelastic Scattering, Vol. 1, IAEA. Vienna, 1978, p. 81.
2. Morozov, V. V. Sumin. A. V. Belushkin. and I. Natkanets. Sov. Phys. Solid State (USA), 27. 1652 (1985).
3. Danilkin, V. V. Sumin. and V. P. Minaev. Sov. Phys. Solid State (USA), 28, 1592 (1986).
4. Hiraga and M. Hirabayashi, J. Phys. Soc. Jpn. 34. 965 (1973).
5. Morozov. Physica B 234-236. 32 (1997).

Ammonium dynamics study in the $Rb_{1-x}(NH_4)_xI$ mixed crystals

I.Natkaniec[1], M.L.Martinez Sarrion[2], L.Mestres[2], L.S.Smirnov[3]

1-Frank Laboratory of Neutron Physics JINR, Dubna, Russia,
2-Department of Inorganic Chemistry, University of Barcelona, Barcelona, Spain,
3-SSC RF Institute of Theoretical and Experimental Physics, Moscow, Russia

The influence of the inner strains on the ammonium dynamics in mixed crystals was studied by us earlier in the $Me_{1-x}(NH_4)_xSCN$ (Me=K, Rb) mixed crystal system [1-3]. As the ionic radius of rubidium is close to that of ammonium, a greater influence on ammonium dynamics from the inner strains could be expected in $K_{1-x}(NH_4)_xSCN$ mixed crystals. This is because the ionic radius of potassium is smaller than the ionic radius of ammonium. It has been shown that the low energy resonance mode E_r, observed in the $K_{1-x}(NH_4)_xSCN$ mixed crystals in the dynamic disordered orthorhombic phase at 10 K, was absent in the spectra of the generalized phonon density of (G(E)) states of the $Rb_{1-x}(NH_4)_xSCN$ mixed crystals in the appropriate concentration region of its dynamic disordered orthorhombic phase at 10 K. Therefore, certain scientific interest has arisen in the study of the possible influence of inner strains on ammonium dynamics in the $Me_{1-x}(NH_4)_xI$ (Me=K, Rb) mixed crystal systems. One could expect their presence in these mixed crystals, to a variable degree, in accordance with the above-mentioned reasons.

Ammonium dynamics in the $K_{1-x}(NH_4)_xI$ mixed crystals were studied by us earlier in the entire concentration region and over a wide temperature interval from 10 to 300 K [4,5]. We showed that this system has two low-energy resonant modes: E_r^1 (2-3 meV) and E_r^2 (7-10 meV), and local excitations owing to the translational, ν_5, and librational, ν_6, modes. It is interesting to point out that the two resonance modes are observed only in the α-phase at low temperature (dynamic orientational disordered region and static orientational disordered region of the orientational glass state) and are absent in the ordered γ-phase.

Crystalline samples of $Rb_{1-x}(NH_4)_xI$ mixed crystals were prepared from aqueous solutions with concentrations of x=0.06, 0.16, 0.40, and 0.66 by slow evaporation. The spectra of the inelastic incoherent neutron scattering were measured on the NERA-PR spectrometer set up on the pulsed neutron source IBR-2 (FLNP, JINR, Dubna) over a wide temperature interval from 20 to 300 K. With the help of neutron powder diffraction, it was shown that crystals from the concentration region $0<x<0.40$ at 20 K are found in the α-phase. Diffraction spectra from $Rb_{1-x}(NH_4)_xI$ measured samples are shown in Fig. 1. One can see that the diffraction patterns from the samples with x=0.40 and 0.66 at 20 K have radically changed. This can be explained as a result of the structural phase transition.

The inelastic incoherent neutron scattering (IINS) spectra of the $Rb_{1-x}(NH_4)_xI$ mixed crystals measured at 20 K are given in Fig. 2. Due to the presence of the contribution of the quasielastic incoherent neutron scattering (QINS), the obtained IINS spectra for these samples permitted us to conclude that the $Rb_{1-x}(NH_4)_xI$ mixed crystals for the concentrations $0<x<0.16$ are found in the dynamic orientational disordered state and with x=0.40 - in the static disordered state of the orientational glass.

The generalized phonon density of the G(E) spectra states of the $Rb_{1-x}(NH_4)_xI$ mixed crystals, calculated in the one-phonon approximation and using the measured IINS spectra, are shown in Fig. 3. The G(E) spectra for the concentration $0<x<0.40$ describe the ammonium dynamics in the α-phase region of $Rb_{1-x}(NH_4)_xI$. The vibrational spectrum of ammonium ions in this concentration region is characterized by two low energy resonance modes and two local modes

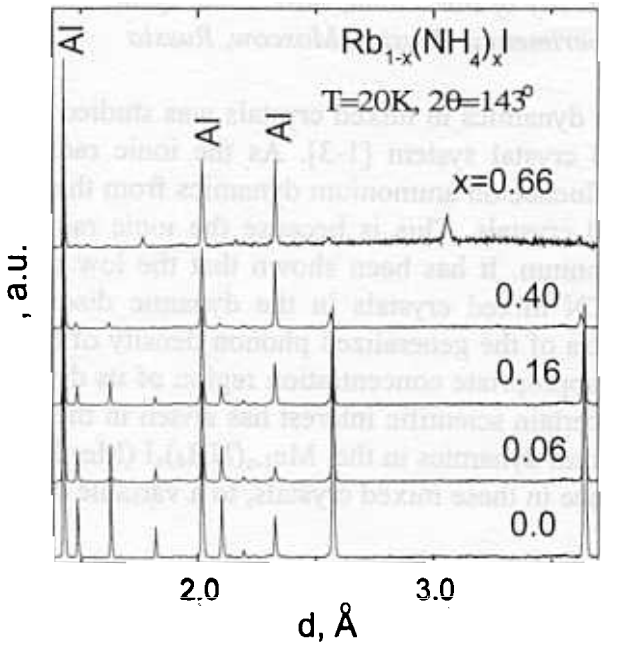

Fig. 1. Diffraction patterns from powder samples of $Rb_{1-x}(NH_4)_xI$ mixed crystals measured at 20 K and the scattering angle $2\Theta=143^{\circ}$.

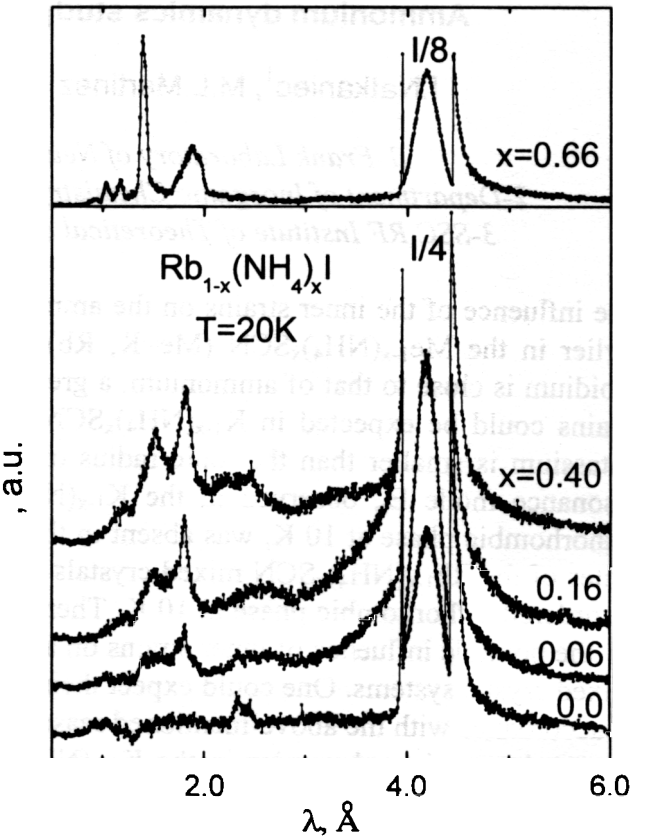

Fig. 2. The inelastic incoherent neutron scattering (IINS) spectra of $Rb_{1-x}(NH_4)_xI$ mixed crystals measured at 20 K.

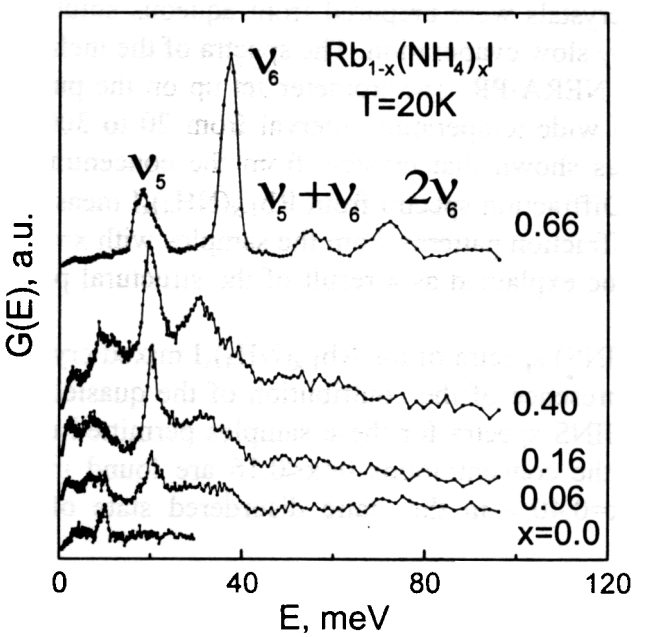

Fig. 3. The generalized phonon density of the states G(E) of $Rb_{1-x}(NH_4)_xI$ mixed crystals.

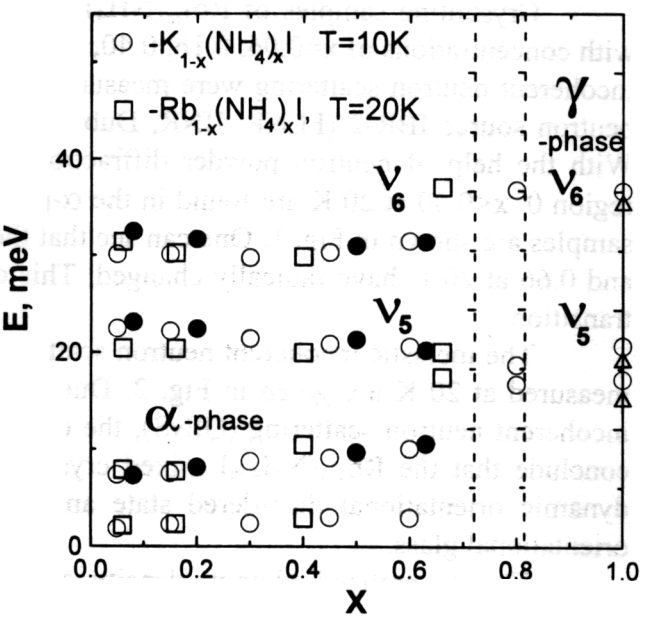

Fig. 4. A comparison of the excitation energies of ammonium ions in $Me_{1-x}(NH_4)_xI$ (Me=K, Rb) mixed crystals at low temperature. ●- E_r^2 resonance and local modes in $K_{1-x}(NH_4)_xI$ determined at 20 K in [6].

which can be assigned to the translational, ν_5, (near 20 meV) and librational, ν_6, (near 30 meV) modes.

The G(E) spectrum for $Rb_{0.34}(NH_4)_{0.66}I$ has peculiarities which are suited to the local translational, ν_5, and librational, ν_6, modes, Raman scattering $\nu_5 + \nu_6$, and scattering from second harmonic of the librational mode $2\nu_6$. A comparison of the ammonium dynamics in the systems of $K_{1-x}(NH_4)_xI$ and $Rb_{1-x}(NH_4)_xI$ mixed crystals is given in Fig. 4. One can see that the energies of the resonance (E_r^1 and E_r^2) and local (ν_5 and ν_6) modes in the $K_{1-x}(NH_4)_xI$ and $Rb_{1-x}(NH_4)_xI$ mixed crystals are similar in the concentration region $0<x<0.40$, at low temperature, and are different near the concentration region $x=0.60$. If the $K_{1-x}(NH_4)_xI$ mixed crystals near $x=0.60$ are in the α-phase, then the $Rb_{1-x}(NH_4)_xI$ mixed crystals are not in the α-phase. However, the energies of the local modes of $Rb_{1-x}(NH_4)_xI$ are close to the energies of the local modes of $K_{1-x}(NH_4)_xI$ in the ordered γ-phase. Thus, the influence of the inner strains can manifest itself in a change in the boundary between the disordered α-phase and β- or γ-phases.

References:

1. I.Natkaniec, L.S.Smirnov, A.I.Solov'ev, Physica **B 213&214**, 667 (1995).
2. L.S.Smirnov, I.Natkaniec, S.I.Bragin, L.A.Shuvalov, S.N.Sulyanov, Physica **B 234&236**, 66 (1997).
3. C.Guy, L.S.Smirnov, I.Natkaniec, BENSC Experimental Reports 1996, edit. by Y.Kirschbaum et al, BENSC HMI, Berlin, 1997, pp.180-181.
4. I.Natkaniec, L.S.Smirnov, Physica B **234&236**, 409 (1997).
5. И.Натканец, Л.С.Смирнов, С.И.Брагин, А.И.Соловьев, Кристаллография, **43**, 246 (1998).
6. J.Tomkinson, B.A.Dasannacharya, P.S.Goyal,and R.Chakravarthy, J.Chem.Soc.Faraday Trans. **87**, 3431 (1991).

NEUTRON SPECTROMETRY AND NUMERICAL SIMULATIONS OF LOW-FREQUENCY INTERNAL VIBRATIONS IN SOLID XYLENES

I. Natkaniec[1], K. Holderna-Natkaniec[2], J. Kalus[3], V. D. Khavryutchenko[4]

1 - Frank Laboratory of Neutron Physics, JINR, 141980 Dubna, Russia, and H. Niewodniczanski Institute of Nuclear Physics, 31-342 Krakow, Poland.
2 - Institute of Physics, A. Mickiewicz University, 61-614 Poznan, Poland.
3 - Institute of Physics, University of Bayreuth, 95440 Bayreuth, Germany.
4 - Institute of Surface Chemistry, Ukrainian Academy of Science, 252028 Kiev, Ukraine.

A molecule of xylene, $C_6H_4(CH_3)_2$, contains a phenyl ring and two methyl groups in the *para-*, *metha-* and *ortho-* positions, as shown in Fig. 1. Determination of a vibrational spectrum requires knowledge of the spatial structure and force-field of the molecule. The calculations were performed for an isolated molecule of the compounds studied. The atom coordinates in the molecule are obtained by the AM1 semi-empirical quantum chemistry (QC) method [1] and the Hartree-Fock method with a 6-31G basis set of the GAUSSIAN 94 program [2].

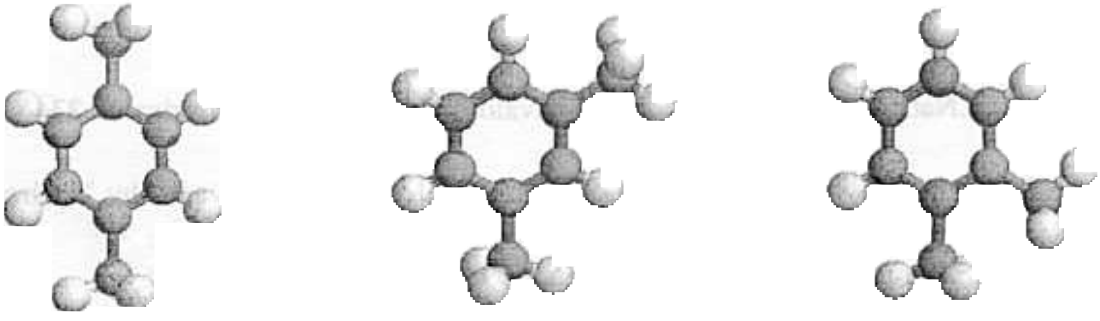

FIG. The calculated structures of the *para-*, *metha-* and *ortho-*xylene molecules.

The structures of molecules as well as the frequencies of normal modes calculated by these two methods do not differ significantly. Using the molecular structure and the force-field matrix calculated by the AM1 method, the inverse spectroscopic problem is solved to fit the calculated frequencies of isolated molecules to the ones experimentally observed in crystals [3].

The force-field is determined in the Cartesian system of coordinates as a matrix of the second derivatives of the total energy of the molecule with respect to atom displacements. From the atom coordinates and the force-field matrix, the frequencies of particular modes - ω_j, and their intensities in the amplitude weighed vibrational density of states - $G(\omega)$, are obtained. The contribution of the *n-th* atom involved in the *j-th* vibrational mode is calculated as a function proportional to the scattering cross-section - σ_n, and the displacement - $a_n(\omega_j)$,

$$G(\omega) = \Sigma_n ([\sigma_n]^2/M_n) \Sigma_j [a_n(\omega_j)]^2 \delta(\omega-\omega_j) \qquad (1)$$

The IINS spectra are obtained in the approximation of one-phonon scattering process by convolution of neutron intensities calculated according to formula (1), with the resolution function of the NERA spectrometer [4]. Inverse transformation of calculated and experimental IINS spectra into $G(\omega)$ spectra presented in Fig. 2 is made without solving the deconvolution problem.

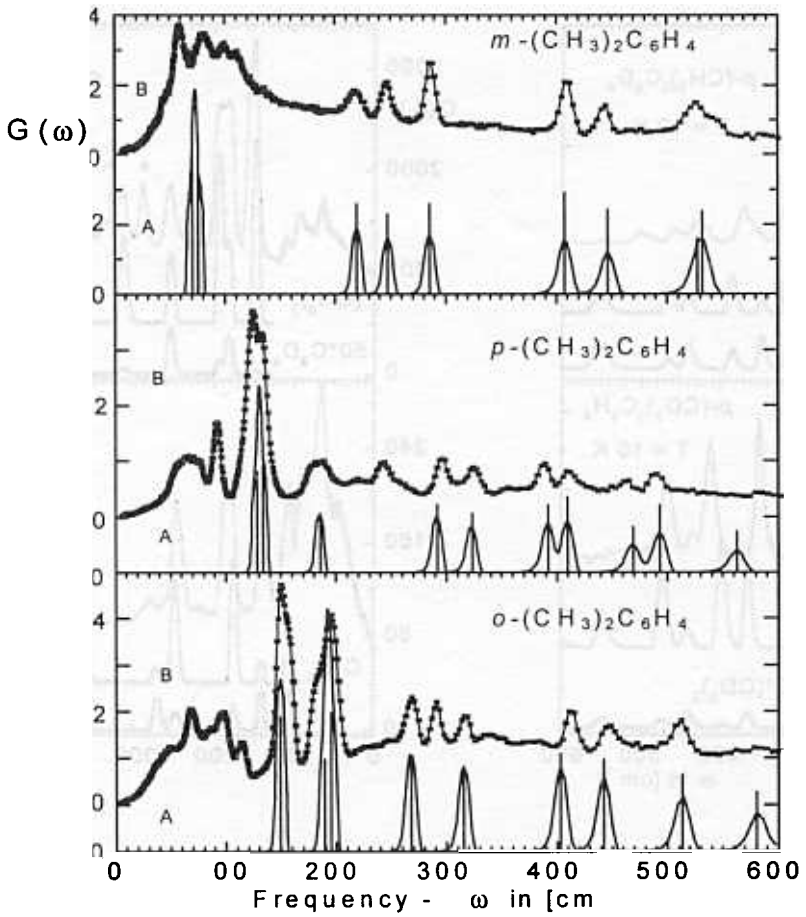

FIG. 2. A comparison of the neutron scattering intensities (A - bars) calculated according to formula (1) and the simulated spectra (A - solid lines) of internal vibrations up to 600 cm^{-1} with the G(ω) experimental spectra (B) of solid xylenes at 10 K.

The frequencies of the torsional modes of methyl groups for isolated molecules of *m*-, *p*- and *o*-xylenes, are calculated by the AM1 method as ca. 60 cm^{-1} for the first two and about 200 cm^{-1} for the third. These modes are experimentally observed at about 60-80 cm^{-1} for solid *m*-xylene, and their frequencies are located in the ranges: 120-140 cm^{-1} and 150-200 cm^{-1} for solid *p*- and *o*-xylenes, respectively. It means that inter-molecular forces in solid xylenes play a significant role in the rotational dynamics of the methyl groups. The calculated frequencies of other internal modes below 600 cm^{-1} differ by about 10% from the experimental ones. Those low frequency deformations of the phenyl ring are mixed with methyl groups rotations. The neutron intensities and simulated G(ω) spectra in Fig. 2,are computed by fitting the calculated frequencies to the experimental ones. Due to mixed character of the low frequency modes the fitting procedure is accomplished by solving the inverted vibration problem using a full force matrix.

IINS spectra of deuterated xylene molecules were also measured in order to test the correctness of fitted force constants matrices and assignments of the low- frequency modes shown in Fig. 2. The spectra of xylene molecules with deuterated C_6D_4- and -$(CD_3)_2$ sub-units are calculated using the force constants matrices fitted to the experimental frequencies of $C_6H_4(CH_3)_2$ molecules. The experimental and calculated spectra of *p*- and *o*-xylenes are presented in Fig. 3. In the case of each partially deuterated sample, deuterated sub-units almost do not contribute to the IINS spectra of protonated sub-units. The experimental G(ω), in this case, corresponds to the partial weighed density of states of protonated sub-units.

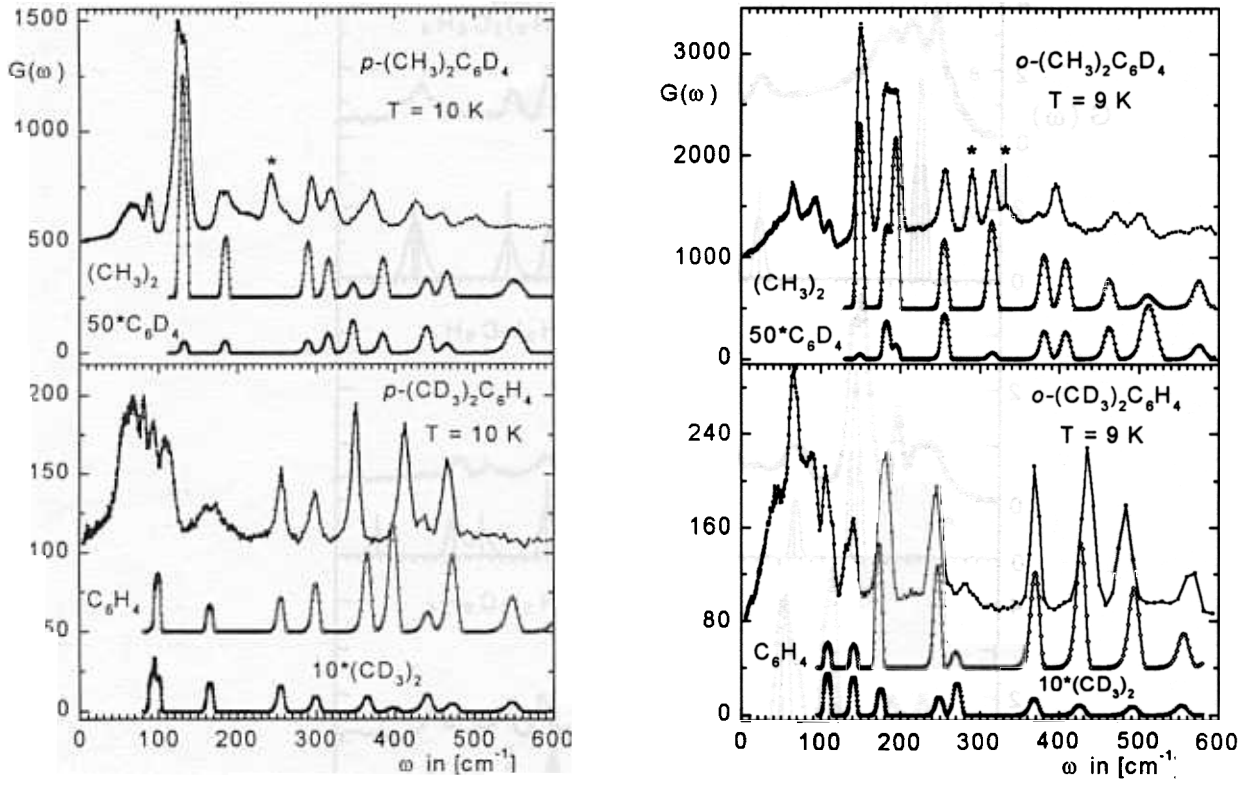

FIG. 3. A comparison of the G(ω) spectra of partially deuterated *p*- and *o*-xylene molecules with the calculated partial G(ω) spectra of the two methyl groups -$(CH_3)_2$ and the phenyl ring C_6H_4- of the corresponding molecules. The partial spectra of deuterated sub-units -$(CD_3)_2$ and C_6D_4- should be multiplied by factors of 10 and 50, respectively, to see them in the scale of protonated sub-units. The second harmonics of the methyl group torsions are marked by asterisk.

The most intense bands in the G(ω) spectra of xylenes correspond to torsions of CH_3 groups. These modes are quite weak in the partial spectra of the phenyl ring, as one can see in Fig. 3. The low frequency deformations of the phenyl ring in xylene molecules are quite intense in the partial spectra of CH_3 groups. The torsional frequencies of deuterated methyl groups are not shifted by the factor $1/\sqrt{2}$, because they are mixed with lattice vibrations. Such modes should be taken into account in lattice dynamics calculations of xylene crystals. Such calculations based on the experimental crystalline structure, which is known for *p*-xylene, are presented in [5] and [6].

Good agreement between the calculated and experimental frequencies as well as neutron intensities for partially deuterated molecules of xylenes confirm the assignments of the low-frequency internal vibrations suggested by the computation of the simulated spectra as presented in Fig. 2. Our recent results illustrate the usefulness of neutron spectroscopy and relatively fast semi-empirical QC calculations for the investigation of low-frequency methyl group vibrations which are very poorly seen by optical spectroscopy methods.

References:

1. Philipenko A.T., Zayetz A.V., Khavryutchenko V.D., Falndysh E.P., Zh. Struk. Khimii, **28** (1987) 155-157.
2. Frisch M.J., Trucks G.W., Schlegel H.B. et all., GAUSSIAN 94, Gaussian Inc., Pittsburgh PA, 1995.
3. Khavryutchenko V.D., The COSPECO complex of programs to computed vibrational spectroscopy, Institute of Surface Chemistry, Nat. Ac. of Science Ukraine, Kiev, 1990.
4. Natkaniec I., Bragin S.I., Brankowski J., Mayer J., Proc. ICANS XII, Abingdon 1993, RAL Report 94-025, Vol. I., p. 89-96.
5. Kalus J, Monkenbusch M., Natkaniec I, Prager M., Wolfrum J., Worlen F., Mol. Cryst. Liq. Cryst., **268** (1995) 20.
6. Natkaniec I, Kalus J., Griessl W., Holderna-Natkaniec K., Physica B, **234-236** (1997) 104-105.

COMPARATIVE ANALYSIS OF IONIC AND HYDROPHOBIC HYDRATION BY INELASTIC NEUTRON SCATTERING

A.G.Novikov[a], M.N.Rodnikova[b] and O.V.Sobolev[i]

[a]*State Scientific Centre – Institute of Physics and Power Engineering, 249020, Obninsk, Kaluga Region, Russia*

[b]*Kurnakov Institute of General and Inorganic Chemistry, Russian Academy of Sciences, 117907, Moscow, Russia*

Neutron scattering experiments of LiCl, CsCl, $[CH_3]_4NCl$ (2M) and $[C_4H_9]_4NCl$ (1M) aqueous solutions carried out by our group in the last years and analysis of these experiments allow us to perform the a comparison of the effects of ionic and hydrophobic hydration on the molecular level. Experiments and data processing methods are described in our previous papers [1-4].

The GFD of pure water molecules and GFDs of water molecules comprising the hydration shells of Cs^+, Li^+ and Bu_4N^+ ions are shown in Fig.1. Although Li^+ and Cs^+ ions belong to different types of ionic hydration (positive or negative), as it follows from the presented data both of these ions lead to H-B network disruption in the hydration shell. The evidence of this is decreasing of the weight of the fist translation mode (lowest-frequency one) corresponding to deformation of tetrahedral angle O-O-O, which is usually regarded as the evidence of the H-B network existence [5]. Primary water structure distortion in the vicinity of dissolved ions is also witnessed by libration bands shift to a lower frequency, which is more obvious in the case of the Cs^+ ion and is weaker in the case of Li^+.

The Bu_4N^+ ion affects the molecules GFD of their hydration shell differently from the ions mentioned above. It follows from Fig.1c that there is no significant changes in the low-frequency part of the spectra. This fact is indicative of the persistence of the H-B network existing in pure water in the vicinity of a large hydrophobic particle. In our opinion, this result directly correlates with the results of neutron diffraction investigations of the water structure in hydration spheres of thetraalkilammonium ions [6-9]. There is clearly shown the absence of significant influence of such ions (at least, up to and including Bu_4N^+) on the hydration water molecular structure which appears as practically indistinguishable from pure water. As it was repeatedly noted earlier, the cause of such a result is the structural features of the ions, that allow them to enter the inherent tetrahedral water structure without distortion. The geometrical model of such structural organization for Me_4N^+ is formulated [8].

It should be noted that the study of hydrophobic effects by Raman scattering and infrared adsorption also did not show a remarkable growth of intermolecular interactions and space coordination of the H-B network in hydration water surrounding the hydrophobic particles [10].

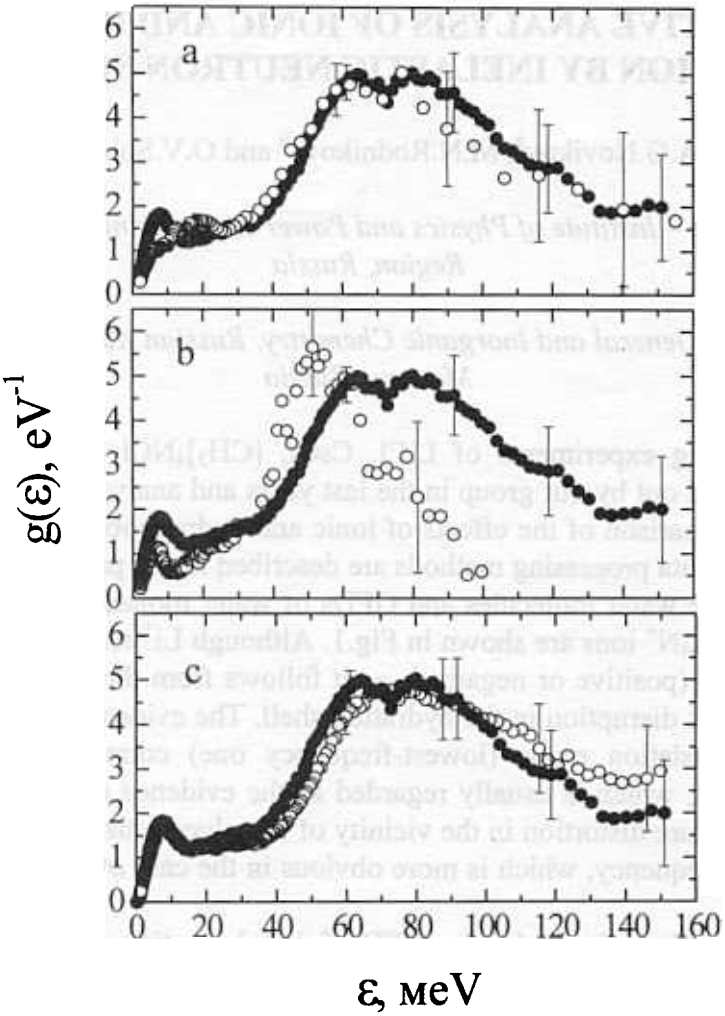

Fig.1. Generalized frequency distributions of water molecules. Solid circles – pure water, open circles – hydration water: (a) - Li^+ ion; (b) - Cs^+ ion; (c) – TBA^+ ion.

REFERENCES

1. A.G.Novikov, M.N.Rodnikova, V.V.Savostin, O.V.Sobolev. Rus. J. Phys. Chem. **70**, 1011, (1996).
2. A.G.Novikov, M.N.Rodnikova, V.V.Savostin, O.V.Sobolev. Chem. Phys. Letters. **259**, 391, (1996)
3. A.G.Novikov, M.N.Rodnikova, V.V.Savostin, O.V.Sobolev. Physica B. **234-236**, 340, (1997).
4. A.G.Novikov, M.N.Rodnikova, V.V.Savostin, O.V.Sobolev. Rus. J. Inorg. Chem. **42**, 1428, (1997).
5. M.Seats, S.Rice. J. Chem. Phys. **72**, 3236, (1980).
6. J.Turner, A.Soper, J.Finney. Mol. Phys. **70**, 679, (1990).
7. J.Turner, A.Soper, J.Finney. Mol. Phys. **77**, 411, (1992).
8. J.Turner, A.Soper. J.Chem. Phys. **101**, 6116, (1994).
9. J.Turner, A.Soper, J.Finney. J. Chem. Phys. **102**, 5438, (1995).
10.Z.Kecki, P.Dryjnski. J. Mol.Structure. **275**, 135, (1992)

SOME STRUCTURAL and DYNAMICAL PROPERTIES of LIQUID $POCl_3$

A.G. Novikov, D.I. Seliverstov, O.V. Sobolev.
Institute for Physics and Power Engineering, 249020, Obninsk, Kaluga Reg.

Liquid $POCl_3$ (chlorine oxide of phosphor) is known as the main component of the mixture constituting a liquid-based laser system (typical composition: $POCl_3$ + $SnCl_4$, activated by Nd^{3+} ions) [1]. Although the chemical properties and the electron excitation spectrum of the liquid are widely studied, the information, about its molecular structure and microdynamics is scarce. At the same time, it is well established that the elementary excitation spectrum of the phonon subsystem and its correlation with electron excitations are directly related to the nature of the electron excitation transfer, its relaxation and quenching [2]. This is why we have undertaken a set of neutron scattering experiments of liquid $POCl_3$ with the spectrometer DIN-2PI, using its diffraction and inelastic scattering modes. The present report contains short information about our first results.

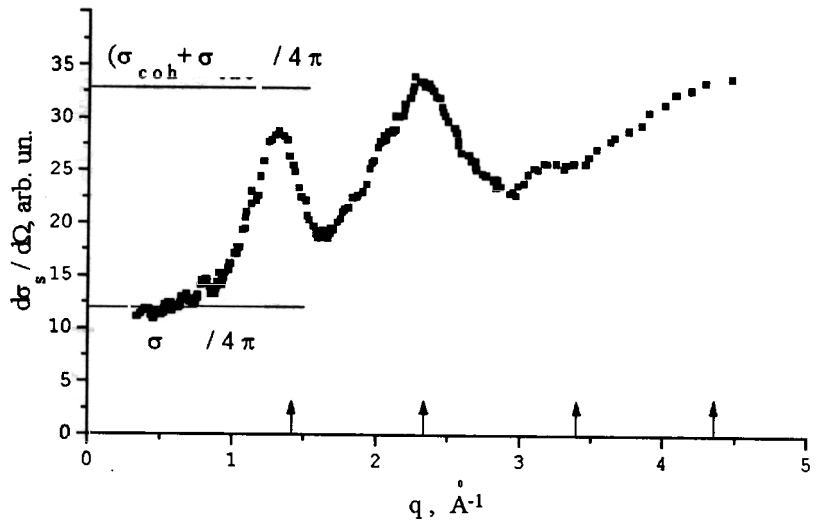

Fig. 1. Angular differential scattering cross section for liquid $POCL_3$

Figure 1 shows the angular differential scattering cross section. The arrows point to the positions of coherent peaks found by X-ray diffraction [3]. The double differential scattering cross sections measured at small scattering angles, where coherent effects can be neglected (see initial part of $d\sigma/d\Omega$ on fig.1), are used to extract the generalized frequency distribution (GFD) of chlorine atoms (87% of scattering events on the $POCl_3$ molecule are connected with chlorine) by the method elaborated for incoherent scatterers [4] (fig. 2). The arrows show the location of the intramolecular modes discovered in optical experiments by IR- absorption and the Raman scattering of light [5]. From figure 2 it can be concluded that the region of intramolecular modes is restricted by energy transfers $\varepsilon \geq 20$meV. Thus, the part of GFD on the left of such energies can be related to intermolecular modes. It should be assumed that a wide peculiarity with the maximum about ε~(4-5) meV contains effects of molecular vibration motions (hindered translations) as well as effects of molecular librations in the force field of neighbors. There is no information about intermolecular interactions in the liquid under study. However, in [6] the method is suggested to estimate the frequency of intermolecular vibrations for liquids on the

basis of their evaporation heat. For $POCl_3$ taking $H_{ev} \cong$ 8 kCal/mole, we get ε_{tr} ~ (7-8) meV. If it is assumed that the intermolecular part of GFD can be described by the superposition of two Gaussians, we get one centered near ε~ (7-8) meV (assumed translational), and the second peak (librational) near ε~(4-5) meV (see inset of fig. 2).

Analysis of the quisielastic component of scattering in the region of small q allows to estimate the selfdiffusion coefficient for $POCl_3$ the liquid as D ~(1.6±0.2) cm^2/c.

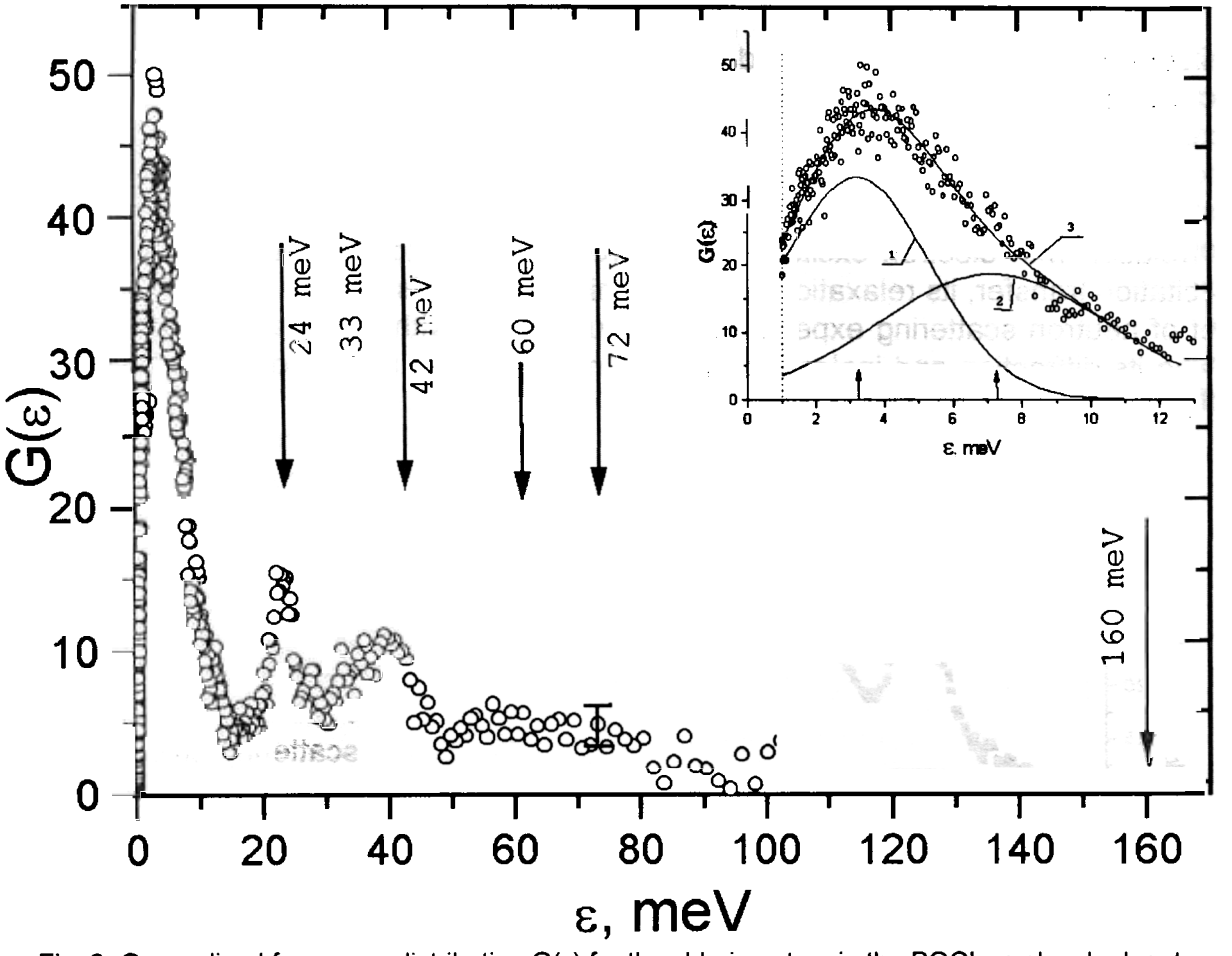

Fig. 2. Generalized frequency distribution G(ε) for the chlorine atom in the $POCL_3$ molecule. Inset: intermolecular part of G(ε). 1 -libration mode; 2 -translation mode; 3 - common approximating curve.

REFERENCES.

1. Yu.G. Anikeev, M.E. Zhabotinski, V.B. Kravchenko. Lasers on Inorganic Liquids. M., "Nauka", 1986, 248 p.
2. V.L. Ermolaev, E.N. Bodunov, E.B. Sveshnikova, T.A. Shahverdov. Emissiveless Transfer of Electron Energy Excitation. L., "Nauka", 1977, 311p.
3. A.K. Dorosh. Structure of Condensed Substances. Lviv, "Vissha Shkola", 1981, 176p.
4. A.G. Novikov, Yu.V. Lisichkin, N.K. Fomichev. Russ. J. Phys. Chem. 1986, v.60, p.1337.
5. K. Nakamoto. Infrared Spectra of Inorganic and Coordination Compounds. J. Wiley & Sons Inc., New York, London, 1984.
6. N.G. Bahshiev, V.S. Libov. Dokladi RAN, Phys.Chem., 1990, v.312, p. 1384.

THE IINS SPECTROSCOPY OF AMINO ACIDS: L-ISOLEUCINE

A. Pawlukojc [a], I. Natkaniec [a], J. Leciejewicz[b]

[a] *Frank Laboratory of Neutron Physics, Joint Institute for Nuclear Research, 141980 Dubna, Russia*
[b] *Institute of Nuclear Chemistry and Technology, Warsaw, Poland*

As a continuation of our studies of the dynamical properties of hydrogen bonds in aliphatic amino acids we report the results of IINS investigations of L-leucine and L-isoleucine. In previous studies of L- and DL-valine [1] and L-leucine [2] the out-of-plane γ(N-H...O) hydrogen bond vibrations were uniquely identified by the IINS method.

L-isoleucine (L-2-amino-3-methylopentanoic acid), a simple aliphatic acid, exists in the form of a dipolar ion (zwitterion). The X-ray diffraction study [3] shows that the asymmetric unit cell contains two crystallographically independent molecules with *trans* and *gauche* I conformations. The molecules of L-isoleucine and their numbering are shown in Fig. 1. The nitrogen atom of the amino group in the *gauche* I conformation forms three hydrogen bonds aligned in nearly tetrahedral directions while in the *trans* molecule one hydrogen atom is shared by two hydrogen bonds forming a bifurcated system. The hydrogen bond distances for L-isoleucine are listed in Table 1.

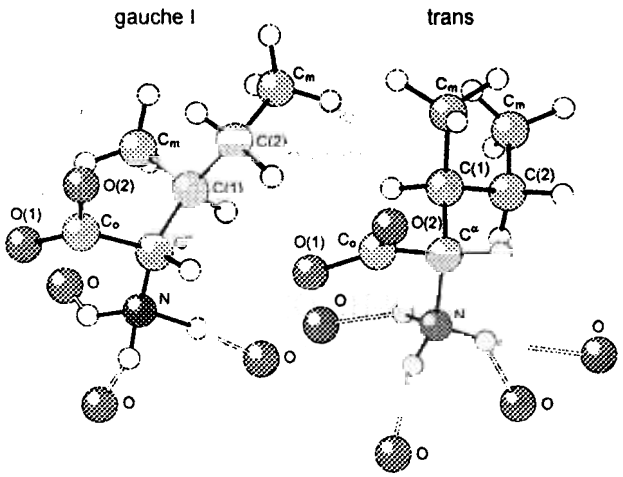

Fig. 1. The conformation of L-isoleucine molecules (by the program MOVIEMOL)

The IINS method provides some adventages in studies of molecular vibrations in solids as compared to optical spectroscopic methods: (i) no selection rule has to be applied to the incident neutron during its interection with molecular vibrations; (ii) low-wave number vibrations give more intense bands than high-wave number ones; and (iii) proton incoherent cross-section is much larger than that of other nuclei; consequently, vibrational modes in which the hydrogen atom participates give rise to IINS bands with much higher intensities than the bands appearing due to other atoms. The substitution of hydrogen by deuterium whose incoherent scattering cross-section for thermal neutrons is almost 40 times smaller and the oscillator mass is twice as large makes it possible to identify uniquely the modes due to hydrogen vibrations in molecules. Therefore, an amino group deuterated sample of L-isoleucine was used in our experiment.

Table Hydrogen bond distances for L-isoleucine [3]

Gauche	N(1)...O(11) [II(010)]	2.844 Å
	N(1)...O(2) [I(010)]	2.867 Å
	N(1)...O(11) [I(010)]	2.812 Å
Trans	N(11)...O(1) [II(000)]	2.794 Å
	N(11)...O(12) [I(010)]	2.845 Å
	N(11)...O(1) [I(100)]	2.993 Å
	N(11)...O(2) [I(100)]	3.028 Å

Numbers I and II denote the operations: I, x,y,z; II, 1-x,0.5+y,1-z.

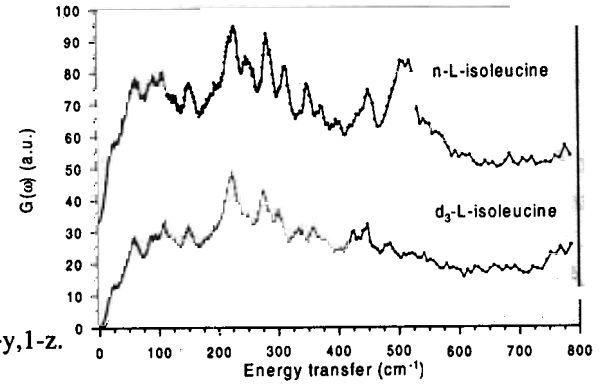

Fig.2. The IINS spectrum of normal and d_3-L-isoleucine.

Neutron scattering measurements were performed using a commercial grade polycrystalline sample of L-isoleucine (Fluka Chemie AG). The deuterated sample was supplied by the Prikladnaya Khimija Company in St. Petersburg. Only hydrogen atoms of the amino group were substituted up to 95% by deuterium. Neutron scattering data were collected at the pulsed reactor IBR-2 in Dubna using the inverted geometry time-of-flight spectrometer NERA-PR. The phonon density of states function $G(\omega)$ of normal and d_3-L-isoleucine at the temperature 90 K is shown in Fig. 2.

Out-of-plane γ(N-H...O) hydrogen bond vibrations.

It is known, that the NH_3 group exhibits triple-degenerate torsional vibration observed at energies of approximately 250-300 cm^{-1}. This degeneracy is lifted when hydrogen atoms become involved in a hydrogen bonding scheme operating in the crystal. Three frequency modes can be separated in the IINS spectrum of normal L-isoleucine: two intense bands at 505 and 518 cm^{-1} and a weak band at 250 cm^{-1}. These modes were found to be absent in the spectrum of the deuterated sample. This indicating their relation to out-of-plane γ(N-H...O) hydrogen bond vibrations.

Methyl groups deformations.

The IINS intensities of hydrogenous compounds are completely determined by the mean-square displacement of protons. In fact, intensity modes assignment to methyl group deformations were found in the energy range 200-300 cm^{-1} of the IINS spectrum. The mode at 250 cm^{-1} can be ascribed to out-of-plane γ(N-H...O) hydrogen bond and $C(1)H_{tors.}$ vibrations. The high intensity peaks at 219, 228 and 281 cm^{-1} suggest the occurrence of a large proton displacement in $C^{\alpha}H$, $C(2)H_2$ and C_mH_3 groups, respectively.

References

[1]. A. Pawlukojc, L. Bobrowicz, I. Natkaniec and J. Leciejewicz, Spectrochim. Acta, **51A** (1995) 303,
[2]. A. Pawlukojc, J. Leciejewicz, I. Natkaniec, Spectrochim. Acta, **52A** (1996) 29,
[3]. K. Torii, Y. Iitaka, Acta Cryst., **B27** (1971) 2237.

INCOHERENT INELASTIC NEUTRON SCATTERING STUDIES OF 1,8-BIS(DIMETHYLAMINO)NAPHTALENE AND ITS PROTONATED FORMS

A. Pawlukojc[a], I. Natkaniec[a], E. Grech[b], J. Baran[c], Z. Malarski[d], L. Sobczyk[d]

[a] *Frank Laboratory of Neutron Physics, Joint Institute for Nuclear Research, 141980 Dubna, Russia*
[b] *Institute of Fundamental Chemistry, Technical University, 71-065 Szczecin, Poland*
[c] *Institute of Low Temperature and Structure Research of Polish Academy of Sciences, 50-950 Wroclaw, Poland*
[d] *Faculty of Chemistry, University of Wroclaw, 50-383 Wroclaw, Poland*

1,8-bis(dimethylamino)naphthalene (DMAN-proton sponge) (Fig.1.) has been a subject of particular interest for a long time. First of all it is a model example of a group of compounds containing two nitrogen basic centres in close neighbourhood so that attachment of a proton leads to a particularly short and strong N-H-N^+ hydrogen bond. In the case of DMAN, double protonation is not possible. N-H-N hydrogen bonds in protonated DMAN appear to be the shortest of those reported so far. Numerous structural studies show that the N-H-N^+ bridge length can change within the range 2.522(1)-2.621(1) Å. In the case of shortest bridges 2.554(4)-2.579(2) Å, they are usually symmetric and their geometry is governed by the environment in the lattice.

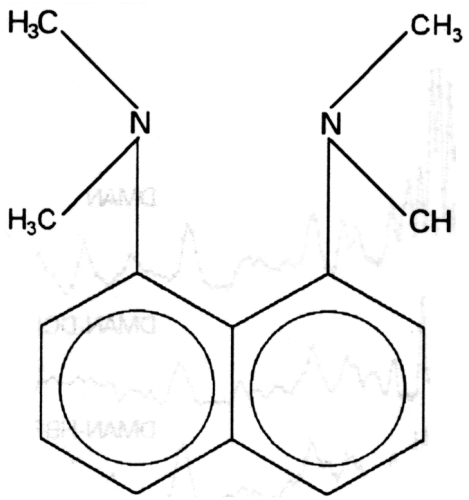

Fig. 1. Schematic view of the DMAN molecule.

There are substantial structural differences between a free DMAN molecule and its protonated cation. In a free DMAN molecule there are two dimethylamino groups turned in opposite directions by 30° with respect to the naphthalene skeleton. One can suspect that they experience a large angle torsional motion. After protonation the system becomes highly rigid and flattened and the torsional motion is hindered.

It seems justified to approach the problem of the dynamics of CH_3 groups in the free DMAN molecule and its protonated cation. The most promising technique seems to be the inelastic neutron scattering. The hydrogen atom nuclei are characterised by a particularly large incoherent scattering cross-section. Therefore, all internal modes with participation of methyl groups should be

characterised by high intensity in low frequency IINS spectra and their sensitivity to the environment should be considerable.

The studied objects were polycrystalline samples of DMAN and two DMAN salts with HBF_4 and 4,5-dicyanoimidazole (DCI). Both salts are characterised by symmetric N-H-N^+ hydrogen bonds 2.562(3) and 2.579(2) Å in length. In the first salt, BF_4^- anions show a dynamic spherical symmetry while in the second one, planar DCI anions are oriented perpendicularly to DMAN cations passing through their C_{2v} symmetry axes. In both cases, nearly planar cations are formed.

DMAN was purchased from Aldrich Chemical Company Ltd. and purified by crystallisation from ethanol. A DMAN complex with HBF_4 was obtained by equimolar neutralisation of DMAN by HBF_4 in ethanol solution and then recrystallized from acetonitrile. A DMAN complex with DCI was prepared by slow isothermal crystallisation from a solution of equimolar amounts of components in acetonitrile.

The functions of the phonon density of states G(w) of DMAN and salts with HBF_4 and DCI are presented in Fig.2. There are observed dramatic changes of bands related to a motion of methyl groups, both torsional and C-N-C bending, and particularly of the bonds connected with motion of as a dimethylamino groups. The behaviour demonstrates intense bands at 125 and 141 cm^{-1} which appear to be poorly resolved doublets. As follows from theoretical analysis, both bands should be ascribed to a motion of as a dimethylamino groups. Participation of large angle vibrations of entire $N(CH_3)_2$ groups seems to be a decisive factor that leads to high intensity of the bands for nonprotonated DMAN as well as a drastic reduction of the intensity on protonation.

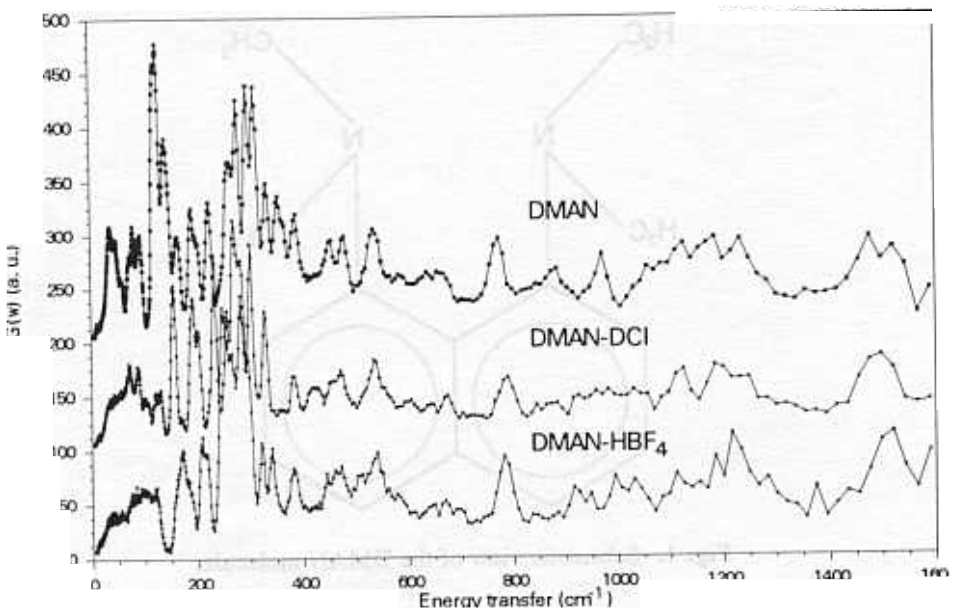

Fig. 2. Low frequency IINS spectra of DMAN and its protonated forms.

High intensity also shows a group of four bands at 262, 278, 298 and 311 cm^{-1}. The two first are related to almost pure torsional vibrations of methyl groups while the other two should be ascribed to CH_3-N-CH_3 bending vibrations mixed with the motion of ring atoms. Relatively intense bands at 163, 190 and 200 cm^{-1} are connected with CH_3 torsional vibrations.

References

[1]. K. Wozniak, T. M. Krygowski, B. Karinki, R. W. Jones and E. Grech, J. Mol. Struct., **240**, (1990) 111,

[2]. T. Glowiak, Z. Malarski, L. Sobczyk and E. Grech, J. Mol. Struct., **270**, (1992) 441,

[3]. E. Grech, Z. Malarski, and L. Sobczyk, Chem. Phys. Lett., **128**, (1986) 259.

NEUTRON STANDING WAVES AT TOTAL REFLECTION OF POLARIZED NEUTRONS OBSERVED THROUGH SPIN-FLIP AND BEAM-SPLITTING

V.L. Aksenov[1], Yu.V. Nikitenko[1], S.V. Kozhevnikov[1], F. Radu[1], R.Kruijs[2], Th. Rekveldt[2]

[1] *Frank Laboratory of Neutron Physics, Joint Institute for Nuclear Research, 141980 Dubna, Moscow Region, Russia*

[2] *Interfaculty Reactor Institute, Delft University of Technology, Mekelweg 15, 2629JB, Delft, The Netherlands*

Introduction

At present, X-ray standing waves are an everyday tool for the study of the structure of crystals and layered nanostructures[1]. At the same time, methods of generation and registration of neutron standing waves are being developed very actively [2-5]. To determine the position and composition of the layer, experimentalists have to register the characteristic radiation typical of the nuclei in the neutron absorbing layer.

In the case of polarized neutrons, it is possible to register standing waves without using nuclear reactions. In fact, if a multilayer structure has a noncolinear magnetic layer, the spin flip process takes place. As a result, in the transmitted (reflected) beam there appears a flux of neutrons J_{sf} that have experienced spin flip. Changes in the J_{sf} flux provide information about the existence and position of the magnetic layer.

Experimental technique

The measurements were conducted with the polarized neutron spectrometer SPN at the IBR-2 pulsed reactor in Dubna. The neutron beam from a polarizer is collimated using cadmium diaphragms over a 3 m flight path to the sample. The mean square deviation of the glancing angle of the incident neutron beam, θ=2.5ч4 mrad, in the direction perpendicular to the sample surface is ±0.1 mrad. The reflected from the sample neutron beam is registered with a ^{3}He gas position-sensitive detector at a 2.6ч8 m distance from the sample. The neutron beam spectrometry is accomplished by measuring the neutron time of flight from the moderator to the detector. The wavelength mean square deviation is 0.02Е. The reflected from sample neutron beam is transmitted through a polarization analyzer. In front of and behind the sample two spin-flippers are situated to change the polarization of the incident and reflected beams. Measurements in the neutron channel consist of the registration of the reflected from sample neutron counts J (on(off), on(off)) in turn in four spin measurement modes corresponding to four states «on(off),on(off)» of two spin-flippers. The investigated sample is a 100 mm x 60 mm x 5 mm multilayer structure on a glass substrate. To prepare it, layers of 1000Е copper, 2000Е titanium, 60Е cobalt and 300Е titanium are sequentially applied by sputtering. The upper titanium layer is to prevent cobalt oxidation. For the sample to be magnetically noncollinear, a magnetic field is applied at an angle γ to the sample surface. As a result, the external magnetic field vector is at some angle to the magnetic induction vector in the cobalt layer, which leads to neutron spin flip. The angle γ is varied within the limits 0ч90 degrees of arc.

Results of Measurements and Discussion

Let us discuss the qualitative picture of formation of the neutron density in the sample. In the general case, the optical potential consists of a wave transforming (transformer), wave phase shifting (shifter) and a wave reflecting (reflector) region. In the shifter, at the distance L from the reflector there is a magnetic layer (flipper) with the magnetization vector noncollinear with the

external magnetic field direction. Let the incident neutron beam travelling in vacuum be $\psi_0^{\leftarrow}$. Having travelled through the transformer, the $\psi_0^{\leftarrow}$ function transforms into $\psi^{\leftarrow}(x)$ (x is the distance from the reflector) being the sum of waves with different reflection multiplicities from shifter-reflector and shifter-vacuum interfaces. It is reflected with the amplitude r from the reflector. This results in the appearance of the opposite running wave $\psi^{\rightarrow}(x)$. The waves $\psi^{\rightarrow}(x)$ and $\psi^{\leftarrow}(x)$ interfere. As a result, in the shifter a standing wave is formed with the spatial period T_x:

$$T_x=(\lambda/2\sin(\theta))/(1-\beta U_{sh}(\lambda/\sin(\theta)^2))^{1/2} \qquad 1)$$

where $\beta=2m/h^2$, h is the Planck constant, m is the neutron mass, λ is the neutron wavelength in vacuum, θ is the glancing angle, U_{sh} is the coherent interaction potential of the neutron with the shifter.

For the reflected beam of neutrons with the spin state «-(+)» in vacuum we have:

$$J_{r,-(+)} \quad \alpha_{+,sf(nsf)}\psi^{+}(x_m) + \alpha_{-,nsf(sf)}\psi^{-}(x_m)|^2 =$$

$$\alpha_{+,sf(nsf)}(\psi^{+\rightarrow}(x_m)+\psi^{+\leftarrow}(x_m))+\alpha_{-,sf(nsf)}(\psi^{-\rightarrow}(x_m)+\psi^{-\leftarrow}(x_m))|^2 \qquad (2)$$

where the coefficients α are expressed through the transmission and reflection amplitudes of the transforming layer, x_m is the flipper to reflector distance, and «+(-)» on the wave function denote the neutron «+(-)» spin state in the shifter. From Eq.(2) it is seen that the reflected neutron beam J_r is determined not only by the interference of oppositely running waves with a particular spin state but also by the interference of waves with the states «+» and «-» in the shifter. The interference of oppositely running waves leads to that the neutron intensity becomes a periodic function of the neutron wavelength and the distance from the reflector surface to the flipper. The interference of waves with different spin states in the shifter blurs the peaks or even splits them in two. As this takes place, spin-flip is maximum when the reflector to antinode of the standing wave distance coincides with the reflector to flipper distance. To this end, the following condition must be satisfied:

$$L+\Delta(\lambda)=nT_x(\lambda)\,, \qquad (3)$$

where $\Delta(\lambda)$ is the spatial shift of the standing wave caused by a change in the wavelength dependence of the phase of the complex amplitude of neutron reflection from the reflector. Writing (3) we neglected the neutron wave change in the flipper.

Next, we go to the discussion of the experimental results. Figures 1a,b show the wavelength dependence curves of the neutron counts (with subtraction of the background counts J_{bac}) $\alpha(off,on)=\sum_{\Delta\theta 1}(J(off,on)-J_{bac})/\sum_{\Delta\theta 3}(J(off,off)-J_{bac})$ and $\alpha(off,on)=$ $=\sum_{\Delta\theta 2}(J(on,off)-J_{bac})/\sum_{\Delta\theta 3}(J(on,on)-J_{bac})$ for the case of the external magnetic field 6.75kOe directed at the angle $\gamma=80^0$ to the sample surface. The summation is over the interval of changes in the glancing angle of reflection $\Delta\theta_1$= 4.34÷8.33 mrad, $\Delta\theta_2$=0÷1.99 mrad, $\Delta\theta_3$= 2÷4.34 mrad. The illustrated curves show peaks at λ=3.7 and 5.6E (Fig. 1a) corresponding to the appearance of neutrons with the spin state «-» and a peak at λ=2.8E (Fig. 1b) corresponding to the appearance of neutrons with the spin state «+». The observed peaks correspond to the second and third absorption orders (n=2 and n=3) for the initial «+» state

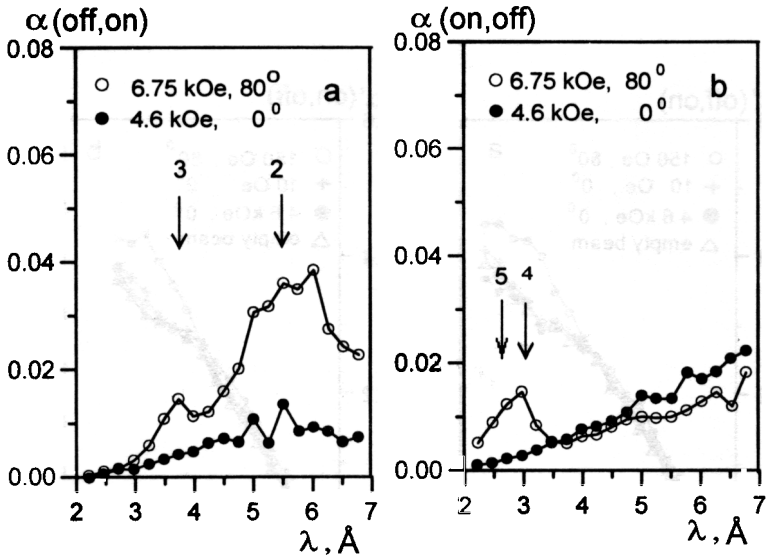

Fig. 1. The wavelength dependence of the ratios of counts α(off,on) to α(on,off) for the glancing angle of the incident beam 3.2 mrad, and the sample to detector distance 3m.

and the fourth plus fifth absorption orders ((n=4)+(n=5)) for the initial «-» state. Lower absorption orders for the initial «-» state are absent because they are forbidden due to insufficient energy of neutrons. Of interest is also the fact that for the initial «+» state, the second order peak is broader than the third order peak. This is due to the fact that in addition to the wave in the initial spin-state, in the phase shifting layer there travels a wave with an opposite spin-state. Calculations show that the magnetic layer magnetization is 2.9kOe. The magnetization 2.9kOe corresponds to the ratio 1:4 of Co atoms to CoO.

The actual layered structure is presented as
glass/1000Е(Cu)/1500Е(Ti)/ 500Е($7Ti_2O_3$+3Ti)/60Е(Co+4CoO)/115(Ti)/195Е($7Ti_2O_3$+ 3Ti).

Of interest is the observation of neutron interference through the angular dependence of the registered reflected neutron beam. This effect is connected with the fact that because of a change in energy at spin transition the reflected neutron beam with the state «-/+» is scattered in the nonspecular direction «nspec»(the specular direction we denote by «spec») according to the relation $\theta_{nspec}^2(mrad^2) = \theta_{spec}^2(mrad^2) \pm 0.147H\ (kOe) \times \lambda^2(Е^2)$[6]. This results in that the periodic wavelength dependence of the intensity of the beams (on,off) and (off,on) due to the formation of standing wave becomes a periodic function of the glancing angle. Figure 2 shows the angular dependence of the intensity of the beams «off,on» and "on,off". Against the background of a strong peak of specular reflected neutrons there are seen peaks of the third and second absorpsion orders of the initial "+" spin-state at the reflection angles 3.7 and 4.8mrad and a peak of the fouth and fifth absorption orders of the initial "-" spin-state at the reflection angle 1.5 mrad.

In Figs. 3a,b there is shown the dependence of the parameters α'(off,on) and α'(on,off) for H and γ equal to 150 Oe and 80°, 10 Oe and 0°, 4.6 kOe and 0°. For such H and γ the reflected beam is specular. In this connection, the parameters α' differ from the parameters α by that in the numerator of the expression for α' the summation is over the specular reflected beam interval $\Delta\theta_3$. It is seen that in contrast to the data in Fig. 1, both of the curves in Fig. 3 corresponding to $\gamma=80^0$ have a maximum for the wavelength 5.6Е. This is explained by the fact that the magnetic field 150 Oe is no longer sufficient to prevent the appearance of the peak on the dependence α(on,off) (Fig.3b). At the same time, it is obvious that the transition probability increases to 0.1 due to the increase of the angle between the magnetic field vector and the magnetization vector. Fitting the experimental data shown in Fig. 3 we obtain the parameters of layers equal to their values obtained by fitting the data shown in Figs. 1-2.

The conducted investigation shows that at total reflection in the near surface region of the neutron reflector a neutron standing wave with a particular spin state is generated. For the investigated wavelength interval 2ч7Е the standing wave period is 250÷500Е. To register the spin-

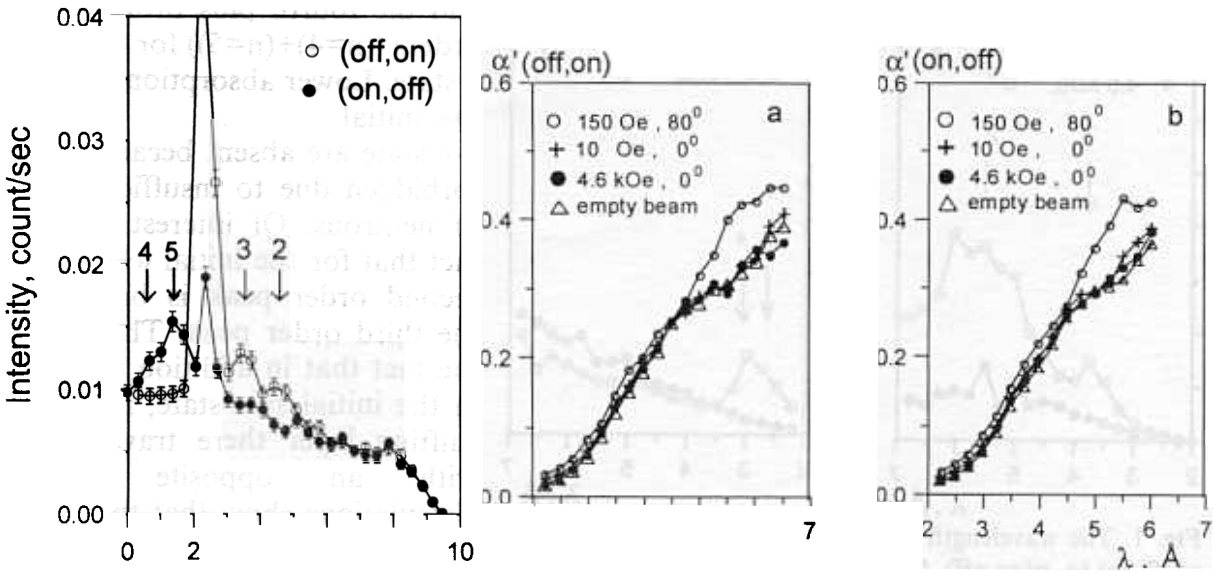

Fig. 3. The wavelength dependence of the parameters α'(off,on) and α'(on,off) for the glancing angle of the incident beam 3.2 mrad, and the sample to detector distance 3m.

flip neutron flux, in addition to the polarization analysis of the reflected beam, the method of splitting of the neutron beam with a particular spin state is used /6,7/. A combined use of two detecting methods makes it possible to decrease, to a large extent, their disadvantages, such as a restricted polarization efficiency of polarization analysis and a limited angle resolution of the beam-splitting. The obtained results allow one to make the conclusion that it is possible to use the method of the generation of the standing wave with a particular spin state for the determination of the position of the magnetic layer with the magnetization of the order of several kOe and the thickness of some fractions of a nanometer. At the same time the luminosity of measurements on the beam with the flux 10^5n/cm^2/sec is high enough to detect a change in the relector-flipper distance of a 50E magnetic noncollinear layer with the magnetization on the order of 20 kOe by the value 0.1E in several hours of measurements.

References:

1. M.V. Kovalchuk, A.Yu. Kazimirov. S.I. Zheludeva, Nucl. Instr. Meth. B 101 (1995) 435.
2. H. Zhang, P.D. Gallagher, S.K. Satija et.al, Phys. Rev. Lett. 72 (1994) 3044.
3. V.L.Aksenov, N.A.Gundorin, Yu.V.Nikitenko, Yu.P.Popov, L.Cser, Proceedings of the National Conference on the Application of X-Ray and Synchrotron Radiation, Neutrons and Electrons, Dubna, JINR, 1997, p.. 266 (in Russian).
4. V.L. Aksenov, N.A. Gundorin, Yu.V. Nikitenko, Yu.P. Popov, L. Cser, «Observation of neutron standing waves at total neutron reflection by the method of precision gamma-spectroscopy», P3-98-374, Dubna, 1998 (in Russian).
5. V.L. Aksenov, Yu.V. Nikitenko, S.V. Kozhevnikov, F. Radu, R. Kruijs, Th. Rekveldt, «Generation of neutron standing waves at total reflection of polarized neutrons», D3-98-369, Dubna, 1998.
6. V.K.Ignatovich, ZhETF Lett., 28 (1978) 311(in Russian).
7. V.L. Aksenov, E.B. Dokukin, S.V. Kozhevnikov, Yu.V. Nikitenko, A.V. Petrenko, J.Schreiber. Physica B 234-236 (1997) 513.

OBSERVATION OF RESONANCE ENHANCED NEUTRON STANDING WAVES USING CHARGED PARTICLE EMISSION AFTER NEUTRON CAPTURE

V.L. Aksenov, Yu.V. Nikitenko, F. Radu, Yu.M. Gledenov,
P.V. Sedyshev, A.V. Petrenko, S.V. Kozhevnikov

Frank Laboratory of Neutron Physics, JINR, Dubna

Introduction

Neutron standing waves were first detected in 1956 [1]. Authors [2-9] conducted a series of experiments to investigate the specific features of such neutron wave fields. Later, in [10] it was suggested to use X-ray standing waves to characterize the structure of crystals. At present, neutron standing waves are an every-day tool in investigations of crystals and layered structures. In the recent time, in connection with an increased demand for the characterization of magnetic and nuclear structures the development of methods of excitation of the neutron wave field mode in layered structures has become the subject of great interest [11-13].

The investigated layered structure Cu/Ti/^{6}LiF has an optical nuclear potential of interaction where the potentials of Cu and ^{6}LiF are the barriers which, together with the negative potential of titanium, form a potential well. Under stationary irradiation with neutrons a periodic spatial distribution of neutron density is created in the titanium layer of the structures due to coherent summation of neutron waves with different reflection multiplicities from potential barriers. The absolute value of the neutron density is determined by the parameters of the potential well and it may largely exceed the density of the incident beam. The neutron wave field whose neutron density exceeds four initial neutron densities is called enhanced neutron standing waves (the ratio of the maximum neutron density in some area of space to the incident neutron density is called the initial density enhancement factor M_i; the initial density enhancement factor divided by four is called the standing wave enhancement factor M_s). The standing wave enhancement mode is extremely sensitive to changes in the parameters of the layered structure, the extent of neutron beam monochromatization and collimation. The increase of the neutron density is limited due to different neutron absorption processes.

To characterize the constituent nuclei of a layered structure, different types of radiation following neutron capture in nuclei are used. Among the main of them are gamma-radiation, alpha-radiation, protons and nuclear fission fragments. In the reported investigation the ^{6}Li (n,α) ^{3}He reaction was used to observe neutron standing waves. Alpha-particles and tritons, the products of the reaction, were registered using an ionization chamber with a low background count level in the presence of gamma-radiation in the IBR-2 experimental hall.

Experimental equipment

The measurements were conducted on the spectrometer of polarized neutrons at the IBR-2 pulsed reactor. At the exit of the polarizer the neutron beam is formed by a diaphragm 0.2mm×40mm. The sample is at 3m from the diaphragm. The sample is a multilayer structure Cu(1000E)/Ti(2000E)/^{6}LiF(200E) thermally sputtered on a glass substrate of the size 5mm×90mm×150mm(along the beam). To register alpha-particles and tritons emitted after neutron capture in ^{6}Li nuclei, the sample is placed into an ionization chamber with a grid. The Cu layer of the sample plays the role of the cathode with the applied voltage –3kV. The working gas in the chamber is argon with a 4% admixture of carbon oxide under the pressure 1.1 atm. The

glancing angle of the incident neutron beam is 2.9 mrad. The reflected neutron beam is registered with a ^{3}He counter at a distance of 2.6 m from the sample. In front of the detector there is a 0.2mm cadmium diaphragm. Detection and data acquisition electronics in neutron and charged particle registration channels makes it possible to obtain spectra in relation to the time interval counted from the moment the neutron pulse arises in the moderator. The duration of the time channel is 64 mcsec.

Results and discussion

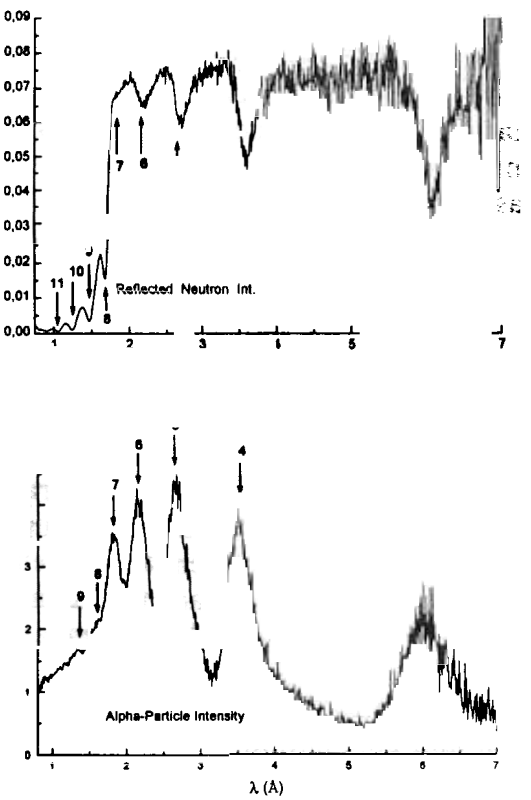

The Figure illustrates the wavelength dependence of the normalized neutron reflection intensities (the reflectometry curve is at the top) and the wavelength dependence of the emission intensity of charged particles (the emission curve is at the bottom) for the glancing angle 2.9 mrad. The reflectometry curve is obtained by the normalization of the reflected neutron flux to the incident neutron flux and the emission curve is obtained by the normalization of the charged-particle yield at the neutron glancing angle 2.9 mrad to the charged-particle yield at the glancing angle of the incident beam 30 mrad. For definite wavelengths, on the reflectometry curve there can be seen minimums (neutron absorption orders labelled with numbers 3÷11) and on the emission curve there are maximums (charged-particle emission orders labelled with numbers 3÷9). Charged particle emission orders correspond to neutron absorption orders. The absorption (emission) orders appear due to the fact that the standing wave antinode coincides with the ^{6}LiF layer. It can be seen that the width of peaks on the reflectometry curve is two times smaller than their width on the emission curve. This is because the measuring channels have different angular resolutions. The angular resolution in the reflectometry channel is $(\delta\theta/\theta)_R = 6\times10^{-3}$ and in the emission channel it is $(\delta\theta/\theta)_E = 1.6\times10^{-2}$. The maximum value of the enhancement factor in the titanium layer is larger than in the absorbing layer ^{6}LiF. For the angular resolution of the reflectometry channel the neutron density enhancement factor M_i in the ^{6}LiF layer is 4.9, 5.8, 5.6, 4.8, 4.8, 2.4, 1.8 for orders 3, 4, 5, 6, 7, 8, 9, respectively, and in the titanium layer it is 27.6, 18.5, 14.8, 11.2, 7.2, 2.5, 1.8, 1.6, 1.3 for orders 3, 4, 5, 6, 7, 8, 9, 10, 11, respectively. For the angular resolution of the emission channel the enhancement factor has smaller values.

In the estimation of the limiting capacity of the registration channel the important parameters are the effect count and the background count. In the charged-particle registration channel the effect count is determined by the yield of charged particles from the layer ^{6}LiF after the capture of neutrons from the neutron beam falling at the glancing angle. If the neutron beam has a mean square angular deviation of 40 mcrad, the glancing angle of the incident beam is 2.9 mrad and the sample size is 25mm(beam height on the sample)×150mm(along the beam) with the

^{6}LiF layer thickness 190E, the effect count in the maximum at the wavelength 1.8E is 0.8 (time channel)$^{-1}$sec^{-1}(incident neutron flux 1.3×10^3n/sec, beam cross section 0.11cm^2, initial neutron density enhancement factor 3).

The background count is determined by the particle yield from the ^{6}LiF layer induced by neutrons scattered on argon and it is 8.0×10^{-5} of the count caused by the effect. The minimum background count depends on the radiation situation (the beam is shut with a 2 mm cadmium sheet) and is 5×10^{-5} (time channel)$^{-1}$sec^{-1}. When the neutron flux through the chamber is less than 10^3 n/sec, the background count is determined by the radiation situation.

Conclusion

The conducted investigation has shown that neutron reflection experiments on the IBR-2 beams with an angular resolution of the order 5 mcrad (neutron flux on the sample is 100 n/sec) continue to provide sufficient measuring statistics. It is, therefore, possible to investigate the effect of standing waves in monocrystals as well as study layered structures with a neutron standing wave enhancement factor up to M_s=100. In this case, for a 1E neutron absorbing layer the cross section of its constituent nuclei must be higher than 1 barn.

The work is performed within the framework of the RFFI project No. 98-02-17037.

References

1. J.W. Knowles, Acta Crystallographica, **9**, 61 (1956).
2. D. Sippel, K. Kleinstuck, G.E.R. Schulse, Phys. Status. Solidi, **2**, 104 (1962).
3. D. Sippel, K. Kleinstuck, G.E.R. Schulse, Phys. Letters, **8**, 241 (1964).
4. F. Eichhorn, D. Sippel, K. Kleinstuck, Phys. status solidi, **23,** 237 (1967).
5. S.Sh.Shilstein, V.I.Marukhin, M. Kalanov, et al., Pisma ZhETF **12**, 80 (1970).
6. S.Sh.Shilstein, V.A. Somenkov, V.P. Dokashenko, Pisma ZhETF, **13**, 301 (1971).
7. D. Sippel, F. Eichhorn, Acta Crystallogr., **A24**, 237 (1968).
8. R. Michalec, P. Mikula, L. Sedlakova, Phys. Status solidi, **a26,** 317 (1974).
9. R. Michalec, P. Mikula, L. Sedlakova, Phys. Status solidi, **a23,** 667 (1974).
10. B.V. Batterman, Appl.Phys.Lett., **1**, 68 (1962).
11. H. Zhang, P.D. Galagher, S.K. Satija et. al, Phys. Rev. Lett. , **72** ,3044 (1994).
12. V.L. Aksenov, Yu.V. Nikitenko, S.V. Kozhevnikov, F. Radu, R. Kruijs, T. Rekveldt, D3-98-369, JINR, Dubna, 1998.
13. V.L. Aksenov, N.A. Gundorin, Yu.V. Nikitenko, Yu.P. Popov, L. Cser, P3-98-374, JINR, Dubna, 1998.

Reflectometry studies of the coherent properties of neutrons

D.A.Korneev[1], V.I.Bodnarchuk[1], S.P.Yaradaikin[1], V.F.Peresedov[1], V.K.Ignatovich[1],
A.Menelle[2], R.Gaehler [3]

[1]*Frank Laboratory of Neutron Physics, JINR*

[2]*Laboratoire Leon Brillouin, Saclay, France*

[3]*Technical University Munchen, Germany*

The question of the neutron coherent length ξ is important for understanding what the wave function of the elementary particle is: always a plane wave or it has the properties of a nonspreading wave packet with a spatial dimension ξ characteristic of the particle. For the investigation of the issue diffraction experiments were some time ago most promising. The first attempts to measure the coherent length were made as early as 1968 in [1]. However, the final result has not been obtained yet. The main difficulty is that the length ξ characterizing the behavior of every separate neutron is masked, like in most experiments, by the final angular and energy resolution of the neutron beam. This leads to that the obtained result is just the lower estimate of the sought value while for reliable identification of ξ, it is desirable to have the upper estimate.

We think that reflectometry measurements[4] make it possible to get into the region where a transition from wave to corpuscular properties takes place and thus, we can at least to lift the lower estimate of ξ essentially in comparison with diffraction method. For processing of reflectometry data it is not sufficient to know one parameter, the resolution of the instrument, but it is necessary to introduce another parameter, the coherent length or the characteristic dimension of the region where the neutron demonstrates wave properties, i.e interferes with itself. The first parameter is determined by the characteristics of the instrument and can be calculated. The second is the fundamental property of the neutron and is found from the experiment.

In our experiments the specular reflection of neutrons from thin films sputtered on a substrate is used. In the whole, the system is characterized by three parameters: the height of the film potential, u_0, the height of the substrate potential, u_s, and the film thickness, d. The film serves as a high resolution neutron interferometer [4] because in it, there occurs the interference of two neutron waves reflected from two interfaces. If

the neutron is characterized by the wave packet with the centre of gravity moving at velocity v, for the incidence on the film at some angle, due to the component of the momentum parallel to the entrance surface (direction $\mathbf{e}_l$) the exit point of the neutron on reflection from the back interface shifts along the vector $\mathbf{e}_l$ with respect to the entrance point by the value l equal to:

$$2d / \left(tg\varphi \sqrt{1 - k_g^2 / k^2} \right), \qquad (1)$$

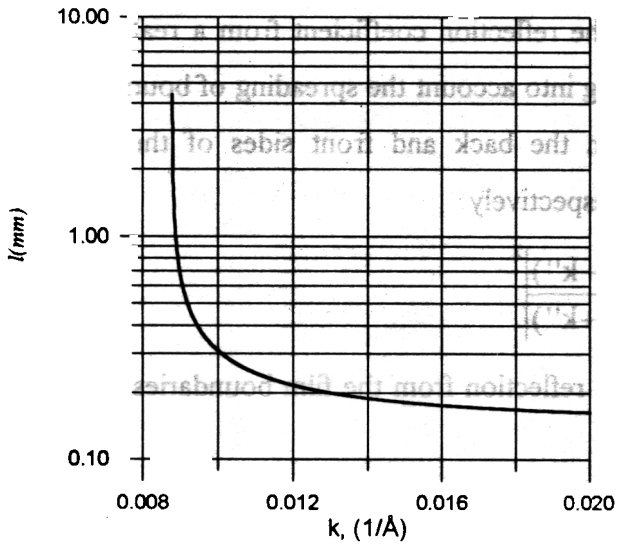

Fig. 1. The shifting parameter of coherent spots l as a function of the normal component of the wave vector calculated for the film thickness d = 1820Å and k_g=8.79 10^{-3}, φ=2.46 10^{-3}rad.

where d is the film thickness, φ is the glancing angle, k_g is the boundary value of the wave vector characterizing the height of the film potential, k is the component of the incident wave vector normal to the film surface.

The coherent length ξ characterizes the dimensions of the coherent neighborhoods (spots) of the neutron entrance and exit points on the entrance surface and formula (1) determines the shift of two neighborhoods. In the region of overlapping of two spots the incident and reflected neutrons interfere and create an interference pattern on the film surface.

Below, we do not use the exact formula for the dependence of the contrast on the shift l. For simplicity, we assume that lateral coherence decreases by the Gauss law as the spots move apart by the distance l along the direction of $k_{o\|}$

$$F(l / \xi) = 1 / (\sqrt{2\pi}\xi) \exp(-l^2 / (2\xi^2)),$$

The double value of the parameter ξ entering into the formula we call the lateral coherent length. Further we shall use the linear dependence of lateral cogernt lenght ξ on the neutron wavelength λ. It is obvious that the parameter characterizing the degree of coherence of the beams reflected from the front and back boundaries of the film is the ratio l/ξ and the condition of coherent beam overlapping is $l/\xi << 1$. The latter is simply the requirement of practically complete spatial overlapping of spots.

This is the scheme that lies in the basis of experiments performed by the authors on the neutron reflectometers REFLEX (IBR-2 reactor, Dubna) and EROS (ORPHEE reactor, Saclay). The sample is a 1814Å copper film sputtered on a glass substrate. The experimental method is the time-of-flight technique, i.e., the dependence of the reflection coefficient $R_{exp}(k)$ on the wave vector k and, at the same time, on the parameter l because l is the function of k (see Fig. 1), is measured. Let us introduce the coherent R_c and incoherent R_{ic} reflection coefficients for the discussed type of potentials. For a correct description of the reflection coefficient from a real film it is necessary to investigate the problem taking into account the spreading of boundaries. In this case, the reflection coefficient from the back and front sides of the film are described by the coefficients R_1 and R_2, respectively

$$R = \left|\frac{sh(\pi h_1(k-k'))}{sh(\pi h_1(k+k'))}\right|^2, \quad R_2 = \left|\frac{sh(\pi h_2(k'-k''))}{sh(\pi h_2(k'+k''))}\right|^2$$

Then, the problem of multiple incoherent reflection from the film boundaries gives the coefficient of incoherent reflection

$R_{ic} = (R_1 + R_2 - 2R_1R_2)/(1 - R_1R_2)$,

The coefficients R_1 and R_2 are the analytical solutions of a one-dimensional problem of reflection from the Eckart potential V(x)

$V(x)=V_0/[1+\exp(-x/h)]$.

In another hand, the coherent reflection coefficient R_c is obtained from the solution of the problem of two sewed Eckart potentials which is not included in this article because of a cumbersome analytical expression derived for this case [5]

In above formulas, k' and k" are the normal components of the wave vector in the film and substrate, respectively, h_1, h_2 are the parameters characterizing the graded potentials at the film/vacuum and film/substrate interfaces, respectively. The weights, with which R_c and R_{ic} enter into the formula for the total reflection coefficient R, are determined by the overlapping integral of coherent spots and depend on the parameter l/ξ

$$R(k, l/\xi) = \left(1 - \mathrm{erf}\left(\frac{l}{2\sqrt{2}\xi}\right)\right)R_c + \mathrm{erf}\left(\frac{l}{2\sqrt{2}\xi}\right)R_{ic} \qquad (2)$$

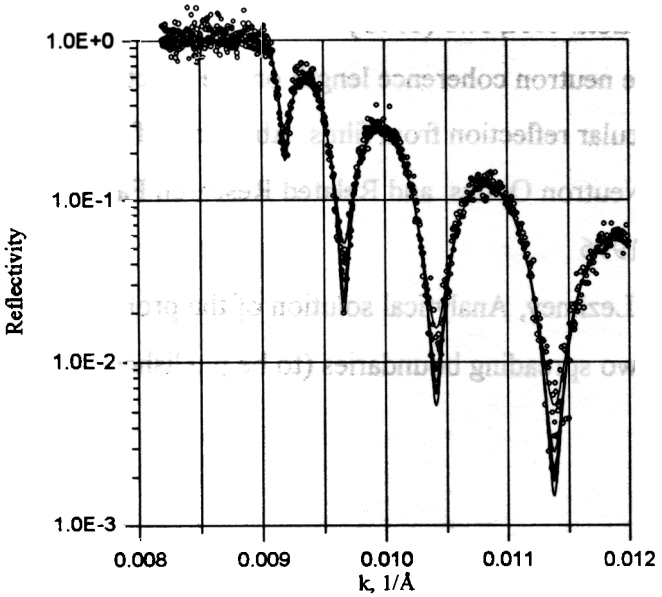

Fig. 2. Circles illustrate the experimental dependence R(k) for φ=10.2 10^{-3} rad, solid line is the set of theoretical curves for different 2ξ (λ=1.9Å) in the range from 1 to 11 mm. Beginning from 2ξ (λ=1.9Å) = 1.6 mm theoretical curves lie in the corridor of statistical errors.

For the purposes of fitting of the experimental reflection coefficient $R_{exp}(k)$ by dependence (2), a set of theoretical curves corresponding to different 2ξ was drawn taking into account instrument resolution $\Delta k/k$ (see Fig. 2). It appears that for $2\xi \geq 1.6$mm for λ=1.9Å all calculated curves lie in the corridor of statistical errors and describe well the experimental dependence $R_{exp}(k)$.

Thus, it follows from experimental data processing that $2\xi \sim 1.6$ mm for λ=1.9Å is the low estimate of the neutron lateral coherent length and it is about 7 times larger than the recent experimental estimates 0.25 mm for λ=1.9Å published in [3].

The fact that the lower estimation of 2ξ is of the order of few mm for thermal neutron is very important for interpretation of neutron reflectometry experiments in general. Weak dependence of the form of the reflection coefficient on ξ when the lower estimation for ξ has the order of few millimeters allows us, however, to make the conclusion that interpretation of reflectometry experiments using the assumption of infinite coherent length can be considered correct in most cases. The large length ξ found here can be also considered as a parameter characterizing the perfectness of our sample.

One of the authors (D.Korneev) thanks A.Frank for usefull discussions.
This work is supported by INTAS grant No 97-11329.

References

[1] C.G.Shull, Phys. Rev. Lett. 21(1968) 1585
[2] C.G.Shull, Phys. Rev. 179(1969) 752

[3] U.Bonse, W.Graeff, H.Rauch, Phys. Lett. 69A, N.6 (1979)

[4] D.A.Korneev, On the influence of the neutron coherence length on the spectral dependence of the coefficient of specular reflection from films. Abstracts of the International Symp. on Advance in Neutron Optics and Related Research Facilities (Neutron Optics in Kumatory '96), 1996

[5] V.K.Ignatovich, D.A.Korneev, D.V.Lezhnev, Analytical solution of the problem of neutron reflection from a film with two spreading boundaries (to be published).

STUDY OF OXIDATION OF THIN COBALT LAYERS BY ELASTIC SCATTERING OF HELIUM IONS

A.P. Kobzev, O.A. Nikonov, L.P. Chernenko
Frank Laboratory of Neutron Physics, JINR, Dubna

N.K. Pleshanov, S.V. Metelev, A.F. Schebetov, V.A. Ul'yanov
Neutron Optics Division, PNPI, Gatchina

The fact that the physical properties of thin-film structures can be essentially different from those of bulk materials is recognised now. Often the data obtained for bulk samples cannot be used to predict the behaviour of thin films. However thin films are widely used at present. Therefore, a systematic study of such processes as oxidation in thin films is required. Thin films of Co and Fe are used in neutron polarizers. Oxidation is one of the factors that affect the polarizing efficiency of such devices. The samples under consideration are among those used for neutron reflectometry studies of oxidation of magnetic films [1]. The RBS technique provides additional information on the depth dependence of the chemical composition of thin layers.

Thin (1000Å) films of cobalt were prepared by thermal evaporation on thoroughly prepared 5mm glass substrates. The evaporation was carried out in a vacuum chamber under pressure not exceeding 10^{-4} Pa. The samples were then placed into a furnace and annealed in air for 30 min at different temperatures.

The depth profiles of oxygen were studied by scattering of $^4He^+$ ions with energies ranging from 3.03 to 3.15 MeV. The well-known resonance in the nuclear reaction $^{16}O(^4He,^4He)^{16}O$ at the energy 3.045 MeV is used to determine the oxygen concentration. It allows one to increase essentially the yield of the elastic scattering on oxygen against the background of scattering on heavier elements. The depth profiles of the oxygen content was studied by gradual increases of the initial ion beam energy with a step of several keV. As result, the resonance shifts from the surface of the cobalt layer to the substrate. Model calculations lead to the depth profile of the oxygen content in cobalt that allows describing the whole set of experimental spectra for different energies of $^4He^+$ ions. A similar study of the depth profiles of oxygen in top layers of single-layer and multilayer structures were carried out erlier [2].

In this study the initial ion beam diameter is decreased to 400μm in order to diminish the influense of inhomogeneities and surface roughness on ion scattering spectra. Typical, experimental and calculated spectra of ions scattered at the angle 170° are shown in Fig. 1. One can see that the outputs of $^4He^+$ ions scattered on atoms of cobalt and oxygen in the oxidized layer are comparable.

So the oxygen content in the layer can be defined with a precision of 2-3%. The best fit of the experimental and calculated spectra is achieved for the detector resolution 30 keV, though the actual detector resolution found in a direct measurement of the spectrum of α-particles with the energy 5.5 MeV is 10 keV. The descripancy can be explained by the roughness of the surface of the studied samples.

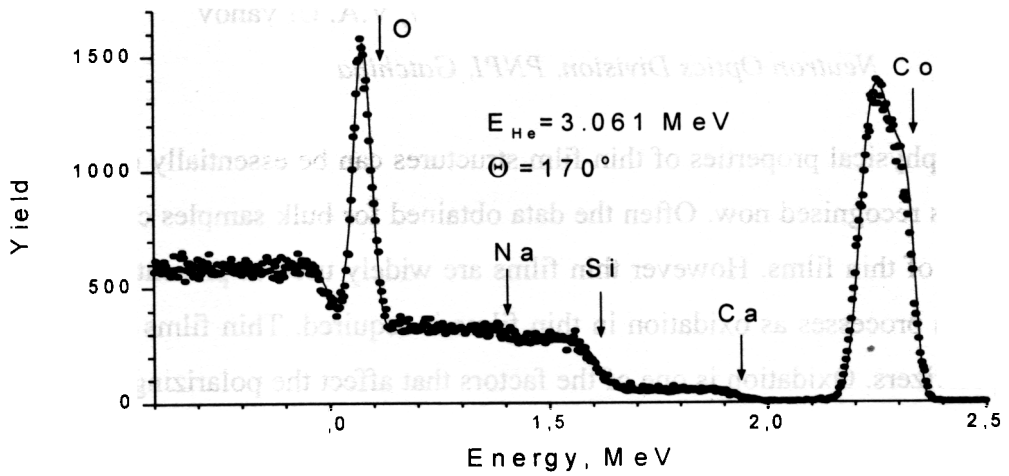

Fig. 1. Experimental (dots) and calculated (solid curve) spectra of helium ions scattered on the oxidized cobalt film. The kinematic borders of all elements are shown by arrows

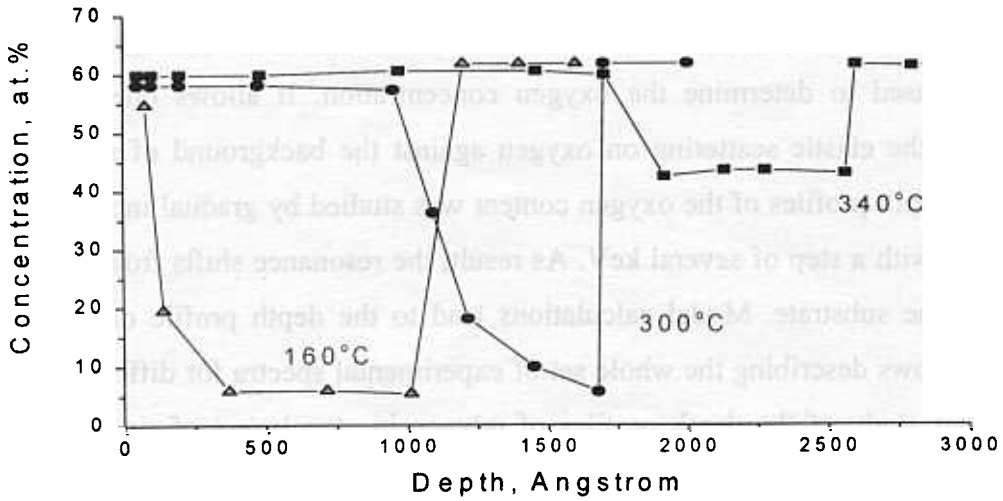

Fig. 2. The depth profiles of the oxygen content in films and glass substrates

In Fig. 2 there are shown the depth profiles of the oxygen content for three samples annealed at different temperatures. The oxygen content in the glass substrate is also shown and is found to be equal to 62±1% for three samples.

In the sample annealed at the temperature 160^{0}C, the oxygen content is found to be slightly below 60% and the oxide layer thickness is 80 Å. The oxide layer thickness increases up to 1000 Å for the sample annealed at the temperature 300^{0}C but the cobalt film is still not completely oxidized. The cobalt film annealed at 340^{0}C is oxidized completely but it cosists from two sublayers. One of them with the oxygen content about 60% starts at the surface and expands up to 1700 Å, and the other with the oxygen content about 43% reaches the substrate and is about 1000Å thick.

Also it should be noted that the experimental results point to the fact that oxide layers are less homogeneous than the initial cobalt layers, since in the majority of cases it is necessary to increase the struggling 3 times to have a satisfactory description of the experimental spectra.

Thus, the experiments carried out show that the non-distructive technique using scattering of charged particles yields detailed information on the oxidation of thin cobalt layers annealed in air.

Also, magnetic measurements were also carried out for the same samples. They demonstrate an essential change in the magnetic state of the samples under annealing at different temperatures (Fig. 3). Qualitatively, magnetic measurements agree with the results shown in Fig. 2. Particularly, they point to an abrupt change in the magnetization of the film as we come from annealing at 300^{0}C to annealing at 340^{0}C.

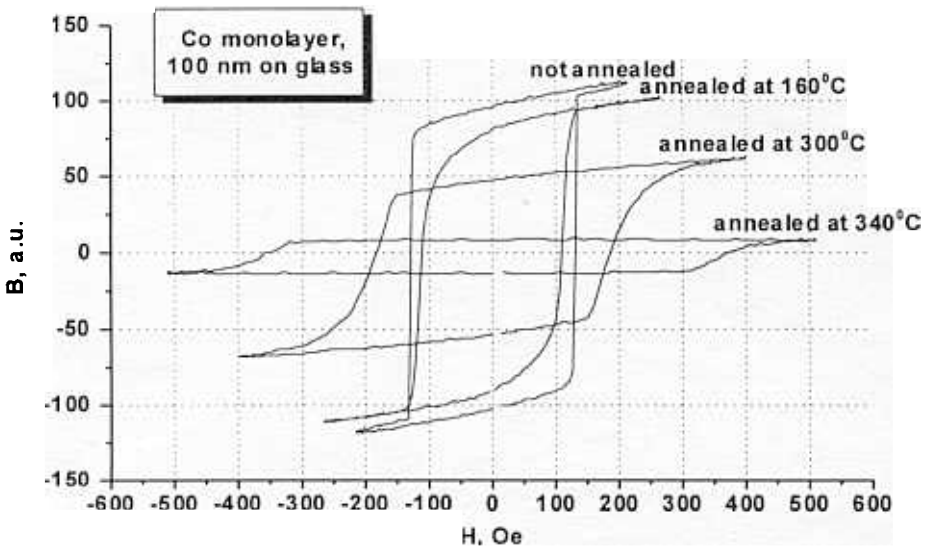

Fig. 3. Hysteresis loops B(H) for Co films annealed at different temperatures.

More detailed information about the magnetic state of the sample may be obtained from the neutron reflectometry data [1]. Combination of different techniques will promote more detailed studies of the effect of oxidation on the physical properties of thin cobalt films.

Similar experiment were carried out to study oxidation of thin iron layers.

The authors are grateful to Soroko Z.N. and Peskov B.G. for the preparation of the initial cobalt films.

REFERENCES

1. N.K.Pleshanov, A.Menelle, S.V.Metelev, Z.N.Soroko, et al., under preparation.

2. A.P. Kobzev, O.A. Nikonov, B.G. Peskov, V.A. Ul'yanov, A.F. Schebetov, Preprint JINR P14-98-110, Dubna, 1998.